

# DESIGN OF STILLING BASINS AND FLEXIBLE APRONS FOR BARRAGES UNDER VARIABLE HYDRAULIC CONDITIONS

Sponsored by:  
Ministry of Water Resources  
Government of India

Project Report prepared and submitted by:

Department of Civil Engineering  
Indian Institute of Technology, Kharagpur  
West Bengal – 721302

March, 2008

## CONTENTS

Chapter number	Title	Page
1	Barrages: origin, function and operation	1
2	Gate operation and its effects	22
3	Uniform gate operation	60
4	Non-uniform gate operation	105
5	Depressed flexible apron	114
6	Flow modelling software	130

## CHAPTER 1

# **BARRAGES: ORIGIN, FUNCTION AND OPERATION**

### **1.1 River diversion structures**

River diversion structures, such as weirs, have been used in the Indian subcontinent since long for diverting water into irrigation canals. The Grand Anicut across River Cauvery in the southern peninsula of India is believed to have been constructed during the second century A.D. and the structure is still in service with improvements being carried out subsequently. The Moghul rulers of the medieval period constructed a weir on river Yamuna in north India to divert water towards Delhi. However, these structures were perhaps constructed without any sound technical knowledge, as no evidence is recorded about any serious investigation into the design aspects. Appropriate scientific research was probably initiated by the British engineers during the latter half of the nineteenth century, who also helped establish hydraulic laboratories near important irrigation projects for carrying out experiments on models of various hydraulic structures. At about the same time, the simple weir section was also modified with addition of a horizontal masonry floor that provided a stable foundation and a finished surface for energy dissipation. Introduction of piers with gates in between helped to bring an overall improvement on control of flow and regulation of water level in the upstream pool and it is this feature that distinguishes a barrage from a weir. Undersluice bays, also called the scouring sluices and with lower crest levels than the regular mid-river or weir bays, are provided nearer the bank to guide the flow of the river particularly that during lean flow periods towards the bank with canal outlet. Divide walls separate the different bays. Other appurtenant structures such as river training works and deformable bed protection apron made of concrete blocks or boulders have been introduced to evolve a comprehensive system of river water diversion. Fig. 1.1 (a) reproduced from CBIP(1981) shows the layout of a typical barrage, the Okhla Barrage on river Yamuna at Delhi, India, constructed near the site of an older weir and meant for diverting water into an irrigation canal. Figs. 1.1(b) and (c) show the longitudinal sections through the weir and undersluice bays of the barrage respectively. The elevations shown are in metres above mean sea level. River diversion barrages have also been used for other purposes such as generation of hydropower and Ackers and Akhtar (2000) provide a very detailed description of one such project in Pakistan. The following section describes the components of a barrage in details.

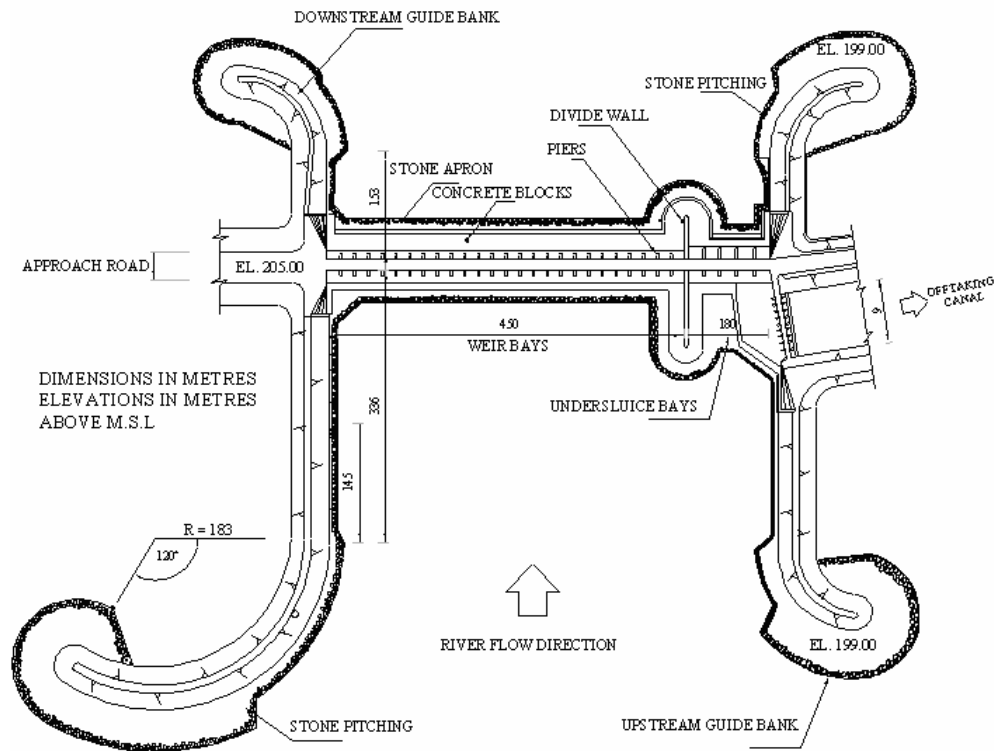


Figure 1.1(a) Layout plan of Okhla Barrage on River Yamuna, India

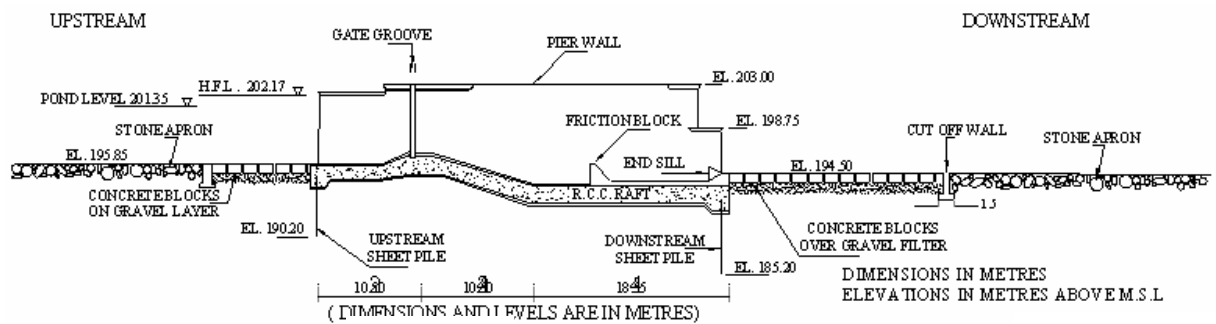


Figure 1.1(b) Section through weir bay of Okhla Barrage (plan shown in Figure 1.1(a) )

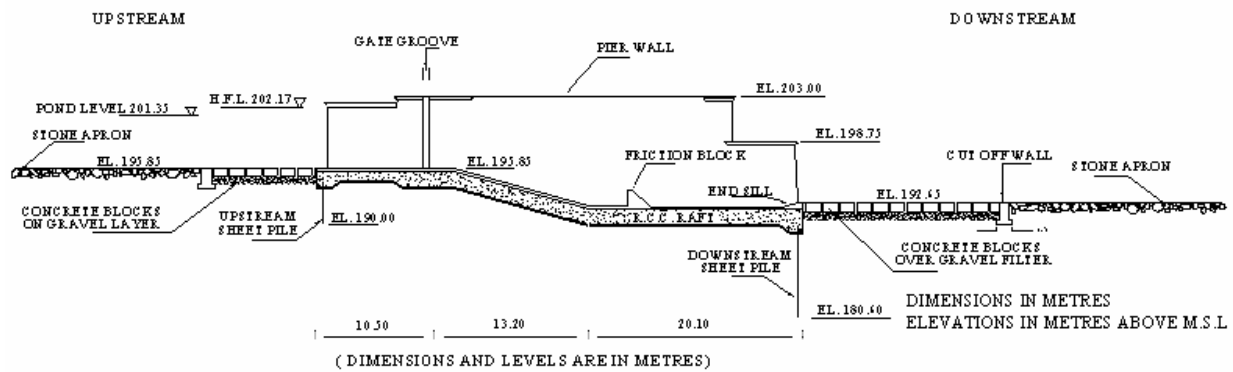


Figure 1.1(c) Section through undersluice bay of Okhla Barrage (plan shown in Figure 1.1(a) )

## 1.2 Components of a barrage

### (a) *Guide banks*

Guide banks direct the main river flow as centrally as possible to the diversion structure. They also safeguard the barrage from erosion and may be designed so that a desirable curvature is induced to the flow for silt exclusion from the canals. The side slopes of the guide banks must be protected by stone pitching, with a sufficient 'self –launching' stone apron at the lowest feasible level. The top level of the guide banks will depend on the increase in the maximum flood level upstream of barrage. The afflux (level difference between head water and tail water during maximum flood flow) results in a back water curve upstream of the barrage, and flood banks have to be provided along the upstream reach of the river to contain the flood flow.

### (b) *Wing walls*

Wing walls flanking the barrage and supporting the abutting earth bunds are designed as retaining walls. Cut-off walls(taken below the scour levels)below the wings and abutment walls at both sides, in addition to the upstream and downstream sheet pile cut-offs across the river, form an enclosed compartment providing good weir foundation conditions.

### (c) *Gates*

Gates used on barrages are of the same type as those used on spillway crests. Vertical lift and Tainter gates are most frequently used to control the flow rate over the crest (sill) of a barrage. The discharge capacity of a gated crest depends on the conditions of free or submerged flows below the gate.

### (d) *Regulators*

The structure controlling diversion into a supply canal is called regulators. The entry sill of a regulator must be such that it permits entry of the maximum flow at various pondage levels. Another important consideration in designing regulators is silt exclusion from canals. Silt-excluder tunnels are often provided in the barrage bays adjacent to the regulator, so that the heavier silt-laden bottom layers of water bypass through the tunnels.

### **(e) *Divide wall***

The divide wall is also like a pier and is provided between undersluice and river-sluice or undersluice and river-sluice and spillway or river-sluice and spillway as the case may be. The following are its main function:

- (i) It separates the turbulent flood waters from the pocket in front of the canal head. It also prevents heavy disturbance which would otherwise result on account of the water in the two portions being at different levels.
- (ii) It helps in checking parallel flow which would be caused by the formation of deep channels leading from the river to the pocket in front of the sluices. If parallel currents still form the floor of the diversion structure and upstream and upstream and downstream flexible protections.

The length of the divide wall on the upstream has to be such as to keep the heavy action on the nose of the wall away from the upstream protection of the sluices and also to provide deep still water pond in front of canal head regulator. The divide wall also plays an important part in the control of silt entry into canal by enclosing a pocket of nearly still water and by separating it from turbulence and vagaries of the main river. Similarly on the downstream side, it should be sufficiently long to guard against action set up by the undersluice discharge damaging the spillway flexible apron on the side of the divide wall. Sometimes the downstream divide wall can be omitted if model experiments indicate to that effect.

The top of the divide wall on the upstream side near the diversion structure is always kept above the pond level with some free board. This gives an indication of the obstruction in the pond for any crafts coming into the pond for sounding, inspection, recreation etc. Beyond some safe distance, the top of divide wall can be lowered (subject to stability requirements). However, any decision should be based on the model test results. Due to difference in the bed levels in the spillway/river-sluice/undersluice portions, it becomes necessary to negotiate the difference in the levels over the length of divide wall in the upstream or downstream side. The slope usually adopted is 1 in 5 and the flexible protections are laid over this slope. Where the downstream divide wall has been omitted on the relevant considerations, the difference in the bed levels has to be suitably negotiated.

### **(f) *Glacis and stilling basin***

The sloping surface downstream of the crest (glacis) and its transition into the stilling basin should be designed so that a hydraulic jump occurs on it over the full range of discharges. The stilling basin is the most common form of energy dissipator converting the supercritical flow from the spillway

into subcritical flow compatible with the downstream river regime. The straightforward and often best method of achieving this transition is through a simple submerged jump formed in a rectangular cross-section stilling basin. Relation between upstream depth and downstream depth is given by the following expression

$$y_2 = \frac{y_1}{2} \left[ -1 + \left( 1 + 8 \frac{q^2}{g y_1^3} \right)^{1/2} \right] \quad \dots \quad (1.1)$$

where  $q$  is unit discharge.

Normally length of the hydraulic jump formed is about 5 times of the difference in water heads in upstream and downstream.

The glacis is the slope joining the crest the crest with the floor on the upstream or downstream side as the case may be. From actual observations at site and from calculations, it has been found that that flatter the glacis, the more intense is the wave and the greater the range of the tough, requiring heavy thickness along a much greater length of the floor. Theoretically, a stream requires more gradual expansion than contraction. From this, it follows that the downstream glacis should be flatter than that of upstream. Where there is considerable heavy material rolling over the crest, a flatter upstream slope would be indicated. It has thus been observed that slopes between 1:3 and 1:5 for the glacis are considered to be the most suitable both for maximum dissipation of energy and economy.

#### **(g) Undersluice**

Undersluices are the bays provided at the canal end of the diversion structure to keep the river under control aiming at the following:

- Maintain a clear and well defined river channel towards the head regulator.
- To enable the canal to draw silt free water from surface only as much as possible.
- Scour the silt deposited in front of the head regulator.
- In case of weirs fitted with falling shutters, to pass the maximum non-monsoon flood without necessitating the dropping of weir shutters.

The undersluice bays may be provided on only one flank or on both the flanks of the river depending on the number of the canals taking off. The layout of the undersluice bays should be thought of on the following considerations:

- The dimensions and level of undersluices should be such that there is the most effective exclusion of silt entry into the canal.

- The dimensions are conducive to maintaining a clear channel towards the canal.
- The capacity of the undersluices is also influenced by diversion requirements during construction or of fair weather escapage.

The dimensions of undersluice bays are best determined by the help of hydraulic model studies. However, a few general guidelines for fixing the dimensions of the undersluices are as given below:

- (a) For ensuring proper scouring capacity the discharging capacity of the undersluice bays at pond level should not be less than twice the capacity of the canal near which they are provided.
- (b) While a hard and fast rule can't be laid down regarding the percentage of the discharge to be passed through the undersluices, usually the capacity could be of the order of 10 to 20 percent of the maximum flood.
- (c) The width of undersluice should be greater than the width of canal regulator and very often it is near about 1.5 times the width of the head regulator.

### **1.3 General operational conditions of a barrage**

The general view of a barrage shown in Fig. 2 gives an idea that the pond or shallow reservoir behind a barrage (seen partially on the left bottom corner of the image) is rather shallow compared to the spatial extent in the horizontal plane. Also, a barrage is designed as a “floating structure”, much like that of a raft foundation, resting over the riverbed material, which may vary from sand in the alluvial reaches to coarse gravel in the hilly terrains. During the non-monsoon months, in order to maintain the pond level (which is necessary to cause a discharge through the head regulator into the off-taking canal) most of the gates are kept closed and those which are open partially are usually closer to the bank with the canal. This is done to keep the deeper section of the river flow nearer the bank with the off-taking canal. During this period, the water level on the downstream of the barrage is usually quite low as the net flow on the downstream side is small and there is a large difference in water level between the upstream and the downstream. This phenomenon causes a significant amount of seepage flow to take place underneath the barrage structure. The continuous operation of most of the gates closer to the bank with the canal also causes the formation of a deep channel towards this side of the river.





Fig. 1.2 View of a barrage looking downstream from upstream right wing wall

### 1.4 Stability issues for a barrage

The structural stability of a barrage depends primarily upon the forces of uplift on the solid floor from seepage flows or differential soil pressure on the underlying row of sheet piles due to scour of riverbed material by high river velocities. The former becomes important during low flows in the river, when a high head difference between the upstream pool and the river downstream may generate destabilizing upward pressure under the floor or cause bailing of sand just downstream of the floor. Flood flows, on the other hand, may cause scour of the river bed in the vicinity of the structure that may lead to its structural failure by overturning, sliding or collapse. The downstream apron and the row of sheet piles below it help to increase the structural stability of the entire structure against both seepage and surface flow forces. The apron length adds to the seepage path and the floor helps dissipate energy by hydraulic jump, thus reducing scour. Notably, publications on river diversion barrages like Leliavsky (1955), Novak et al. (1981), CBIP (1985), Garg et al. (2002) and Varshney et al. (2004) focus mostly on evaluating the seepage forces and estimating the corresponding stability of the structure. Primarily the objective is to calculate the depth of the sheet pile from considerations of hydraulic gradient of the emerging upward seepage flow from the downstream riverbed such that it remains below the critical value for the given soil type. From surface flow considerations, the sheet pile is recommended to be sufficiently deep for stability against general riverbed lowering due to scour under flood flows and is thus a function of the design

flood discharge. For alluvial rivers, the general riverbed scour formula proposed by Lacey (1930) is still commonly used in India and for gravel bed rivers that proposed by Sen (1997) or any other suitable relation is recommended. For silty and clayey river beds there does not appear to be any satisfactory recommendation yet but the alluvial river relation is sometimes used instead.

An examination of published literature shows that no systematic study has perhaps been conducted so far on the characteristics of local scour downstream of barrages, which is a function of discharge, pond level, gate opening and tail water level. The first three parameters are interrelated for free flowing undershot flow below gates. For submerged flows, the tail water level also affects the discharge and pond level. The pond level under uncontrolled flow with full gate opening depends only upon discharge for the free flowing condition and on both discharge and tail water level for submerged.

## **1.5 Planning considerations for barrages**

The planning and design of barrages usually involves the following:

- 1) Location of the barrage axis within a river reach.
- 2) Inclination of the barrage axis with respect to the predominant flow direction at the chosen location.
- 3) Waterway, or the effective open passage not considering the width of the piers, for allowing the design flood water to pass through the structure.
- 4) Number of bays and crest elevation of weir and undersluice bays.
- 5) Length and elevation of stilling basin.
- 6) Depth of sheet piles on the upstream and downstream of the barrage floor from scour conditions of surface flow and uplift conditions of seepage flow.

The first of the above decisions may be taken by studying topographic maps and foundation properties of the chosen site for a river with a fixed bank. Rivers with meandering characteristics, an additional criterion for locating a barrage has to be the nodal point, that is where the lateral migration of the river banks is minimum. This may be determined by studying the surveyed plans of the river from past as many years as possible. Satellite imageries of river plan can also be compared, but since satellite technology is a rather recent development comparison is not possible with earlier river courses.

The second decision of the above mentioned list is usually determined by studying site specific physical models. These studies are also related to the third decision on water- way, which is

tentatively fixed using Lacey's formula (Irrigation engineering and hydraulic structures). However, the deciding parameter for Lacey's waterway formula is the design discharge and a flood of a given return period. The waterway calculated for a design discharge is such that during the passage of the flood, all the gates of the barrage are open to let the peak discharge pass. A flood of a certain frequency (say N years) chosen as design discharge means that the barrage gates are all open only once in N years on an average and that too for probably a few days in that year.

As a result there is sedimentation in the upstream pool usually in front of the rarely opened gates causing formation of shoals. At the time when it is really necessary to open all the gates, as during the rare event of the design or larger flood passing through the barrage, there is skewed flow around the shoals, hitting the piers obliquely. As the flow hits the piers and moves past them, vertical vortices tend to generate.

The number of weir bays and undersluice bays, their crest elevation in relation to the corresponding stilling basin elevation and length are decided considering design flood with an increase of 20 percent, due to an assumed flow concentration. However, the percent increase is taken rather arbitrarily without any sound logic. It is generally reported that this flow concentration is due to the flow not being uniformly distributed even with all gates open since the shoals formed on the upstream of some bays tend to mask the flow through some bays while increasing that through others.

## **1.6 Operational problems**

The difficult operational situations which a barrage has to face during its life are the following:

1. Development of oblique flow
2. Siltation of the pond behind
3. Dangerous scour close to the barrage structure
4. Instability due to uplift

The development of oblique flow may be due to either of the following: (a) unequal gate operation; (b) sediment deposition in the form of shoals or mounds very close to the barrage axis; and (c) general inclination of the river, as in meanders. The first of these is usual for a barrage because of the reason that since a full design discharge would rarely pass a barrage, the gates would be unequally opened to pass the smaller discharges and more so towards the bank of the river with the off-taking canal. The second situation, in fact, often is a result of the previous that is unequal gate operation. With such sustained openings of the gates on one side of the barrage, the deposited

shoals are likely to get stabilized with time. Thus, when a large flood does occur and all the gates are nearly opened, the sediment mound remains quite firm and forces much of the water to be diverted at an angle towards the barrage. Sometimes, however, the oblique flow does occur due to the general flow direction of the river, as in a meandering stream. The next section presents the situation of certain barrages in India that are clearly affected by some of the above conditions.

The third situation is usually considered to occur during the flood flows and the anticipated scour is estimated by a general riverbed degradation formula, like that of Lacey's. However, there may be situations of scour locally near a part of the barrage due to unusual flow conditions, as in front of a particular gate that has broken down. The fourth situation of instability due to uplift may become critical if the floor length is not enough and the seepage pressures are high to cause larger upward forces that cannot be countered by the vertical stabilising forces.

## 1.7 Sedimentation behind barrages and oblique river flow

The following paragraphs discuss the present situation of sedimentation behind barrages and rivers obliquely inclined to barrage axes from images captured from “Google Earth” virtual world model. Please note that all the flows are from above to below.

### 1.7.1 Wazirabad Barrage on River Yamuna, Delhi



Here the river flow itself is obliquely inclined to the barrage axis on the upstream. Also, since the water withdrawal is from the right bank (divide wall may be seen closer to the right bank), a deep water channel (thalweg) has formed on that side. On the right bank, the bays are kind of masked by the protruding bank.

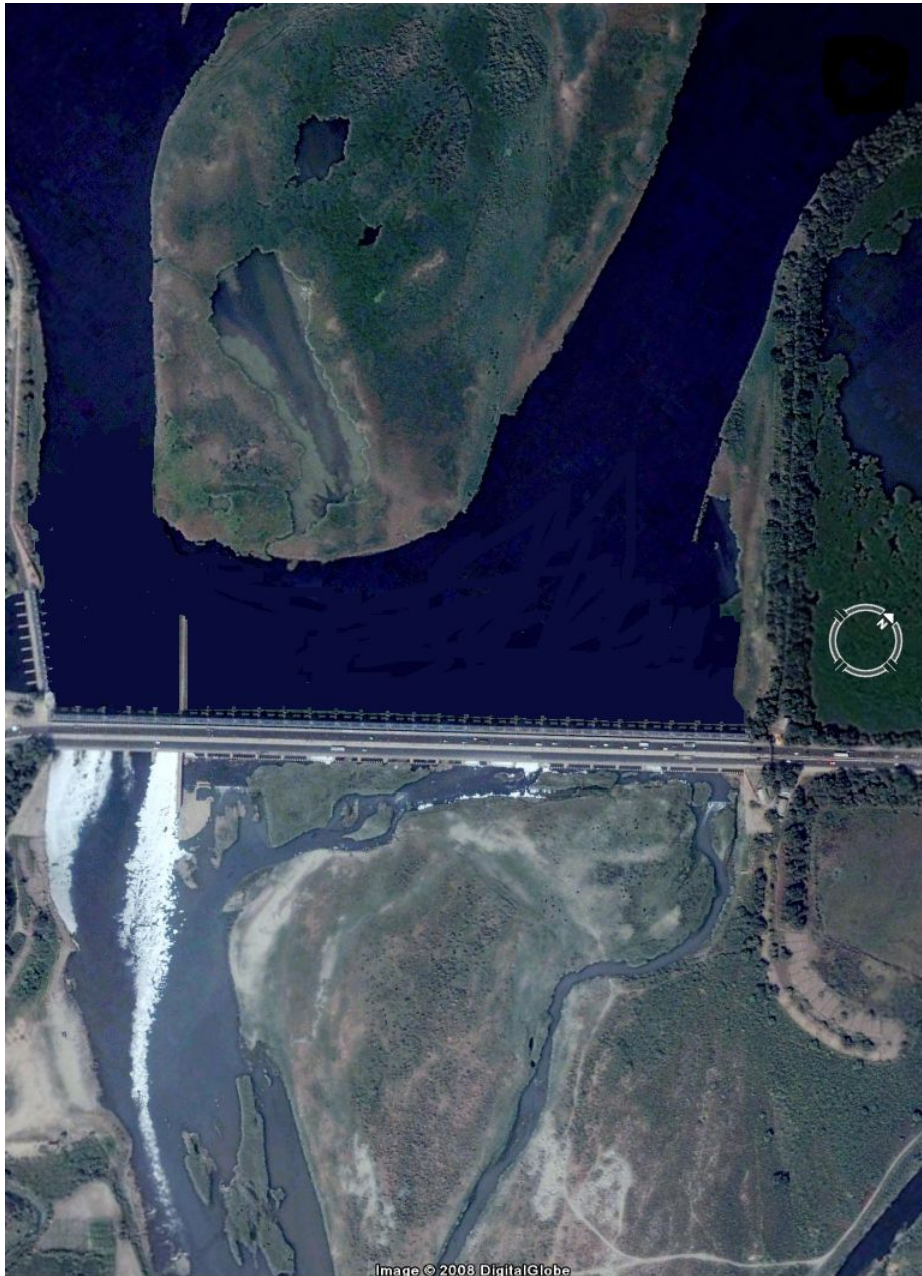


### 1.7.2 Barrage near ITO on River Yamuna, Delhi



For this barrage, there is a clear well defined shoal on the upstream apart from the river also being inclined, causing an oblique flow situation. The shoal appears to be very much stabilized, with signs of farming taking place at places. Naturally, even when a high flood comes, it might be very difficult to remove the shoal, unless assisted by artificial means like dredging, blasting, etc. Here too, the water withdrawal (though recirculatory, as it is required for the thermal power station nearby) from the right bank has led to the gates closer to this bank being kept open for longer times. This is apparent from the formation of the huge expanse of stabilized shoal near the left bank of the barrage on the downstream.

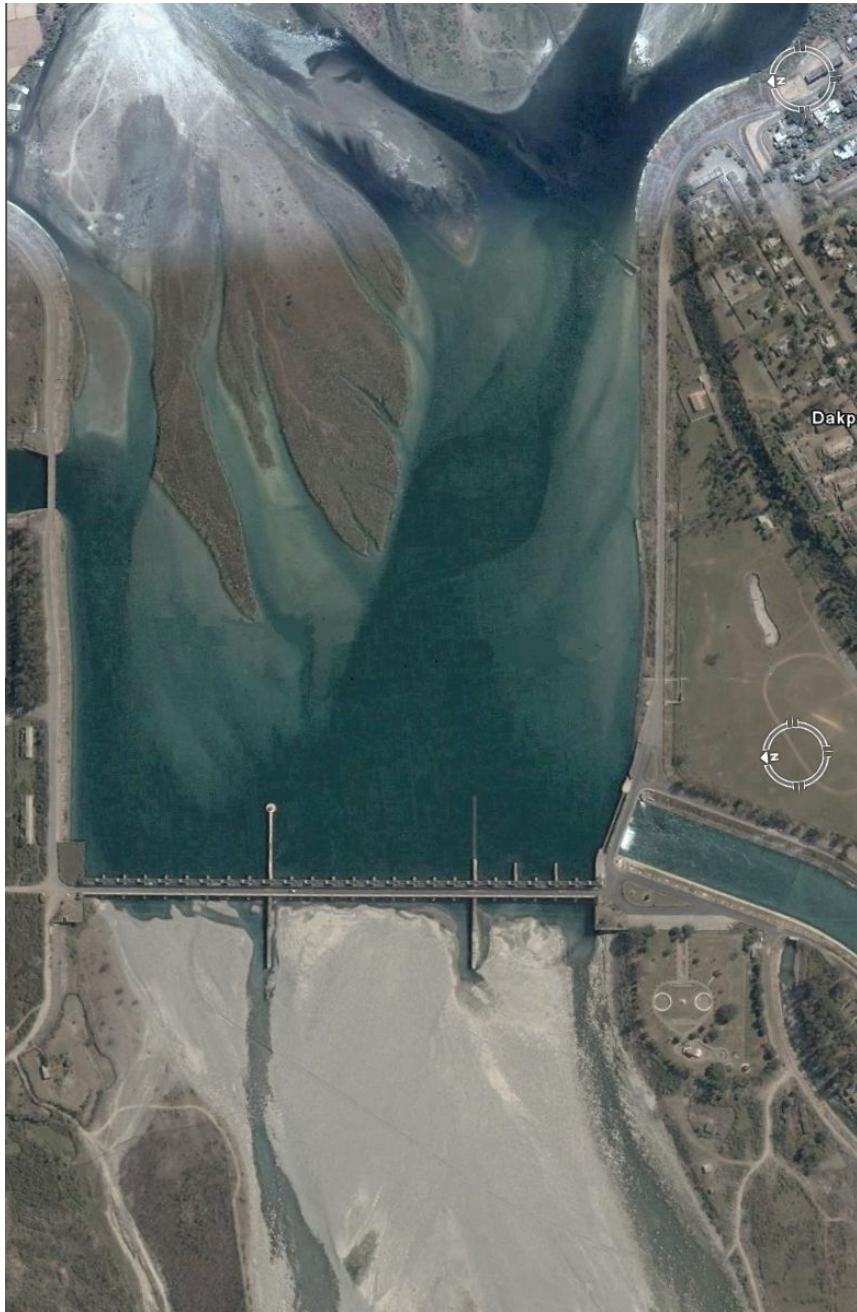
### 1.7.3 Okhla Barrage on River Yamuna, Delhi



This barrage is used to divert water to the Agra Canal (off-take seen on the right bank). The barrage has replaced the century old weir some distance upstream. However, the shoal formed in the pond of the barrage is much larger in size than the previous barrage. It may be noted that since the shoals are visible in the image (most likely taken during the non-monsoon period, as the images are clear) the pond level is at the normal level and the top of the shoal should be somewhat higher than this level. Thus the sediment mound must have got deposited during the high floods. It may be inferred that there would be an oblique flow even during floods.



#### 1.7.4 Dakpathar Barrage on River Yamuna, Delhi



This barrage, also on River Yamuna, is used for diverting water into a power channel (off-take seen on the right bank). The deep channel is appears to be on the left side of the river, as observed from the deeper coloured water body towards this bank on the upstream of the barrage. The tail race of the Khodri power generation scheme meets River Yamuna slightly upstream of the barrage on the right bank. The discharging water from this tail channel appears to have cleared some of the shoals towards the right bank. This barrage is situated in the hilly terrain in contrast to the others.



### 1.7.5 Barrage on River Ganga, Kanpur



This barrage near Kanpur was constructed relatively recently, for supply of drinking water to Kanpur city (lying towards the right bank of the river). Though there are no visible shoal formations in the pool just upstream of the barrage, the river itself is seen to be strongly inclined to the barrage axis. Certainly this is likely to cause oblique flow. This is also clear from the heavy sedimentation on the downstream of the barrage near its left bank. If noted carefully, it may be noticed that the flow emanating from the last few bays of the barrage is possibly taking a turn almost at right angles to the axis. This situation is likely to produce deep scour just downstream of the barrage floor.

### 1.7.6 Barrage on River Ganga, Haridwar



The Bhimgoda barrage on River Ganga was constructed downstream of the older weir to divert water into the eastern and western Ganga canals. There is visible sedimentation to some extent in the pool, but that is somewhat upstream of the barrage axis. However, a close look at the shade of blue in the water of the pond on the upstream provides a clue that the flowing water is rather quite inclined to the barrage axis. In fact, but for the extending divide walls, the flow is nearly parallel to the barrage axis in the pond nearer to the left bank of the barrage. This sort of parallel flows are very dangerous as it may create deep scour near the barrage structure.

### 1.7.7 Barrage on River Mahanadi, Cuttack



This important barrage on the River Mahanadi was also constructed to replace an older weir to divert water to the irrigation canals on either bank. The shoal formation in the pond, though not quite visible from the image, is rather high. In fact, the shoals have formed largely in the middle of the river and the deep channels are seen to be on the left and right banks of the river. Close observation of the flows near the barrage shows indication of very strong oblique flow situations.



### 1.7.8 Barrage on River Kosi



The Kosi barrage situated on the “alluvial fan” of River Kosi as it descends on the plains from the hills of Nepal, perhaps faces the most critical situation regarding the effect of sediment deposition on both upstream as well as downstream of the barrage. As is well known, the river has shifted westwards by about 150 kms over the last 200 years and the trend seems to be still on as seems from the flow of the river downstream of the barrage. Also, the inclination of the main channel of the river on the upstream is inclined substantially to the barrage. Naturally, there exists a very strong oblique flow across the barrage bays.

Interestingly, the canals can also be seen to be heavily silted, a topic of research of the water engineers for past few decades.

## 1.8 Situations causing variable hydraulic conditions for a barrage

The previous discussions highlight the fact that the “normal” conditions envisaged for a barrage often gets changed, particularly due to the deposition of sediment on the upstream as well as downstream and in the close vicinity of the barrage. On the upstream, usually the pond level would prevail for most of the time. Only during the flood season, the high discharge of the river would be allowed to pass by opening the gates. As the flood rises, more and more gates are opened but the relative balance of flow into the pond from the upstream and the outflow from below the gates of the barrage decides on the final elevation of the pond. For very high flows, when all the gates are opened, the pond level would naturally be high, reaching a High Flood Level (HFL). Usually, for design purposes, the HFL is estimated based upon the estimated afflux. However, for the ponds with heavy sedimentation, the HFL would consequently increase due to the rise of the bed.

The other feature of change in water level is that on the downstream. Soon after a barrage is constructed and the gates are installed, the bed level lowers as some of the sediment gets trapped. Thereafter, a deposition starts taking place as some of the water gets withdrawn by the barrage. Gradually, the bed level on the downstream side of the barrage rises and consequently the water level as well. Thus, the Gauge-Discharge (G-D) curve on the downstream shifts upwards meaning that for the same discharge, the water level would be higher.

Depending upon the relative position of water levels on the upstream and downstream of the barrage and opening of the gates four hydraulic conditions are possible for a barrage, quite similar to those occurring for very low height dams (USACE). Identified by corresponding acronyms, these conditions are described below.

- a) CF: Controlled flow (partial gate opening) with free hydraulic jump (Fig. 1.2a). This condition can be expected during low river discharges with substantial downstream riverbed retrogression, as during the first few years of operation of a newly commissioned barrage.
- b) CS: Controlled flow with submerged hydraulic jump (Fig. 1.2b). A condition that is common during periods of medium floods for barrages in alluvial rivers having mild slopes, subject to little or no retrogression.
- c) UCF: Uncontrolled flow (fully opened gate) with free hydraulic jump (Fig. 1.2c). A situation encountered during high floods for barrages in rivers with steep slopes or with riverbeds that have retrogressed substantially.
- d) UCS: Uncontrolled flow with submerged hydraulic jump (Fig. 1.2d). Rather a common occurrence during high floods for barrages in rivers with mild slopes. Also possible where

downstream bed level has aggraded, as observed for barrages after a number of years of operation.

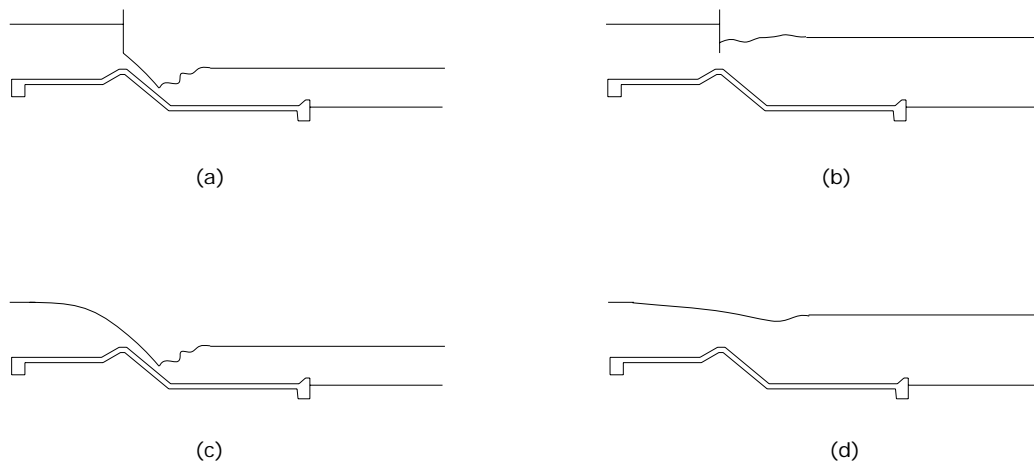


Figure 1.2. Different flow conditions possible for a barrage

Normally, these conditions are likely to occur under uniform opening of all gates and uniform distribution of water flow across the full width of the river. However, the gates often have to be unequally regulated especially during low discharges in the river. The following two situations, one normal and the other exceptional, may possibly produce strongly non-uniform flow situations during low discharge in the river when the tail water is correspondingly low.

- Few gates partially opened to allow the release of water for meeting riparian demands downstream, leading to controlled free (CF) flow situation.
- Collapse of a gate leading to uncontrolled free flow (UCF) situation.

Another extraordinary situation may arise from a partially opened gate during rising flood resulting in controlled submerged (CS) flow situation.

In this report we shall mainly be investigating the effects of the variable hydraulic conditions as discussed above on the energy dissipation system of a barrage. Prior to that we shall have a look at the relation between gate opening and shoal formation in the pond on the upstream of a barrage.

## References

1. CBIP (1981) Publication 148. Barrages in India. Central Board of Irrigation and Power, New Delhi, India.
2. Ackers, J. C. and Akhtar, M.A. (2000) Hydraulic model studies for the Ghazi-Barotha hydropower project, Pakistan. *ICE Proceedings, Journal of Water and Maritime Engineering*. Volume 142, Issue 1.
3. Leliavsky S. (1955) *Irrigation and Hydraulic Design*, London, Chapman & Hall Ltd. 37 Essc. Street, W.C 2,.
4. Novak P. Cabelka, J. (1981) *Models in Hydraulic Engineering: Physical Principle and Design Application*. Pitman Publishing, [ISBN 0-273-08436-4].
5. CBIP (1985) Publication 179. Manual on Barrages and weirs on permeable foundations, Volume-I. *Central Board of Irrigation and Power*, New Delhi, India.
6. Garg, N.K., Bhagat S.K. and Asthana B.N. (2002) Optimal Barrage Design Based on Subsurface Flow Considerations. *Journal of Irrigation and Drainage Engineering*, 128, No. 4, 253-263.
7. Varshney, R.S. (2004) *Irrigation Engineering and Hydraulic Structures*, Khanna Publishers, Delhi.
8. Lacey G., (1930) Stable Channels in alluvium. *Minutes and Proceedings of the Inst. of Civil Engineers*, London, U.K..
9. Sen, P. (1997) “Depth of Scour in Gravelly and Bouldery Rivers” *Journal of the Institution of Engineers (India)*, Vol. 77, 209-214.

## CHAPTER 2

### **GATE OPERATION AND ITS EFFECTS**

#### **2.1 Effect of gate operation on shoal formation**

This study investigates into the causes of shoal formation in the upstream pool formed on the upstream of a barrage and in the river on the downstream as a function of gate operation of the barrage. As is known all the gates of a barrage are not fully opened to the full extent simultaneously, except during the passage of the design flood, which is chosen as a high value like 1 in 100 years. Thus, theoretically, the chance of all gates being fully opened is likely to occur once every 100 years. Further, even in the year of the passage of the design flood, the flood peak may last, at the most, for a few hours. Hence, to maintain a constant pool level, some or all of the gates have to be gradually closed as the flood recedes. In this way, for most of the flood season, there would be partial gate opening of most of the bays. During the lean flow period, most of the gates are likely to be closed, except for the undersluice bays.

On the other hand, a river usually brings in sediment throughout the year and more so during the flood season. If all gates are not fully open at all times, suggesting a controlled flow for many gates, some of these sediments get deposited on the upstream pool due to the sluggishness of flow there. The aim of the experiments in this study is to have an insight into the effect of gate operation on the deposition of sediment. In other words, the series of experiments are aimed at studying the pattern of shoal formation in relation to barrage gate operation.

##### **2.1.1 Methodology for experimentation**

Experiments were done on full barrage model in a river modelling tank (Fig. 2.1), for the following gate operation condition: partial gate opening condition, uniform gate opening condition and arch type gate opening conditions. A model of a typical barrage, but approximately of the dimensions of the Durgapur Barrage in West Bengal, was constructed in the river modeling tank to a horizontal scale of 1 in 300 in the order to fit the entire barrage length within the width of the modeling tank. Considering a distortion of 5 times for



horizontal to vertical, corresponding vertical scale is established as 1 in 60. The prototype-model conformity calculations were made to establish the model bed sediment property. The calculations have been done following Novak and Cabelka (1981).



Figure 2.1. View of river modelling tank from upstream

### 2.1.2 Model scaling

Considering an element of non-uniform flow between the sections A and B separated by a distance  $\Delta l$ , (Fig. 2.2) and from Bernoulli's equation,

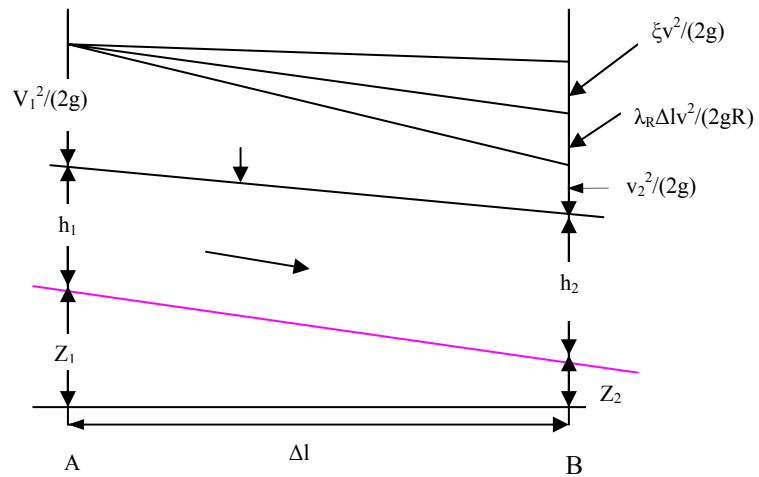


Figure 2.2. Definition sketch for calculation of similarity of water levels

$$Z_1 + h_1 + v_1^2/(2g) = Z_2 + h_2 + v_2^2/(2g) + \lambda_R \Delta l v^2/(2gR) + \xi v^2/(2g) \quad \dots (2.1)$$

Where,  $\xi v^2/(2g)$  includes all losses between the two sections with the exception of friction losses and  $\lambda_R \Delta l v^2/(2gR)$  is loss of energy through friction. ( $\lambda$  is resistance coefficient and is a function of  $(Re, k/D)$ ).

If we write now for  $(Z_2 - Z_1)$  the change in energy  $\Delta E_z$ , for  $(h_2 - h_1)$   $\Delta E_h$  etc., we obtain

$$\Delta E_z + \Delta E_h + \Delta E_v + \Delta E_f + \Delta E_\xi = 0 \quad \dots (2.2)$$

Introducing the model scale in the equation, for example  $M_h = h_p/h_m$ , the following equation is valid for prototype:

$$M_z \Delta E_z + M_h \Delta E_h + M_v^2 \Delta E_v + M_\lambda M_v^2 M_l M_R^{-1} \Delta E_f + M_\xi M_v^2 \Delta E_\xi = 0 \quad \dots (2.3)$$

From Equations (2) and (3), we obtain for similarity of non-uniform flow

$$M_z = M_h = M_v^2 = M_\lambda M_v^2 M_l M_R^{-1} = M_\xi M_v^2 \quad \dots (2.4)$$

From  $v = Q/A$  and for  $M_A = M_b M_h$ , it follows that

$$M_v = M_Q / M_A = M_Q / (M_b M_h) \quad \dots (2.5)$$

Further, the scale of the hydraulic radius  $M_R$  is a function of  $M_b$  and  $M_h$ . After substituting Equation (5) in Equation (4), we obtain

$$M_z = M_h \quad \dots (2.6)$$

$$M_Q = M_h^{3/2} M_b \quad \dots (2.7)$$

$$M_R = M_l M_\lambda \quad \dots (2.8)$$

$$M_\xi = 1 \quad \dots (2.9)$$

There are some more equations, such as

$$M_{so} = M_z / M_l = M_h / M_l = M_{se} \quad \dots (2.10)$$

And for a wide channel  $M_R = M_h$

$$M_\lambda = M_R / M_l = M_R M_h / M_l M_h = M_{se} M_R / M_h = M_{se} \quad \dots (2.11)$$

To arrive at a condition for similarity of the beginning of sediment motion we can use the well known Shields diagram. The diagram shows the relation between the ‘grain Froude number’  $Fr_*^2 = v_*^2 / (gd(s_s - 1))$  and the shear Reynolds number  $Re_* = dv_* / \nu$ , where  $d$  = grain diameter,  $v_*$  = the shear velocity =  $\sqrt{(gSR)} = \sqrt{(\tau_o / \rho)}$  and  $s_s$  = specific gravity of the sediment,  $R$  = hydraulic radius,  $S$  = slope,  $\rho$  = specific mass (density),  $\tau_o$  = wall shear stress.

For the region where the condition of incipient motion is expressed by  $Fr_*^2 = \text{Constant}$ , the condition of similarity may be simply derived from equating the value of  $Fr_*^2$ , that is,  $SR / (d(s_s - 1))$  on the model and prototype.

$$M_s M_R = M_d M_{(ss-1)} \quad \dots (2.12)$$

Noting that  $g\rho(s_s - 1) = \gamma'_s$  and for same fluid on model and prototype ( $M_\gamma = 1$ ) and for  $M_R = M_h$ , equation (12) may be expressed as

$$M_{\gamma'_s} = M_h M_{se} / M_d \quad \dots (2.13)$$

Considering sand ( $\gamma'_s = 1.65$ ) in model and sand ( $\gamma'_s = 1.65$ ) in prototype

$$M_{\gamma'_s} = 1.65 / 1.65 = 1.00 \quad \dots (2.14)$$

$$M_{\gamma'_s} = 12 / M_d \quad \dots (2.15)$$

Therefore,

$$M_d = 12 / 1.00 = 12.00 \quad \dots (2.16)$$

$$\text{Hence, } d_p / d_m = 12 \quad \dots (2.17)$$

From here, we calculate  $d_m$  to be nearly equal to 0.021 mm (assuming  $d_p$  to be 0.25mm)

Since the diameter of the sand required was very small, which could not be obtained practically in large quantities to conduct the experiment, it was finally decided to use an alternative material that would at least give a qualitative result. Hence, HIPS granules (relative density 1.05) in the form of tiny cylinders of diameter around 1mm and length around 3mm were used for conducting the model studies. Scaling calculations showed that HIPS granules of the order of 0.8mm diameter (preferably spherical) would have matched exactly, but since it was not available, we had to be satisfied with whatever available.

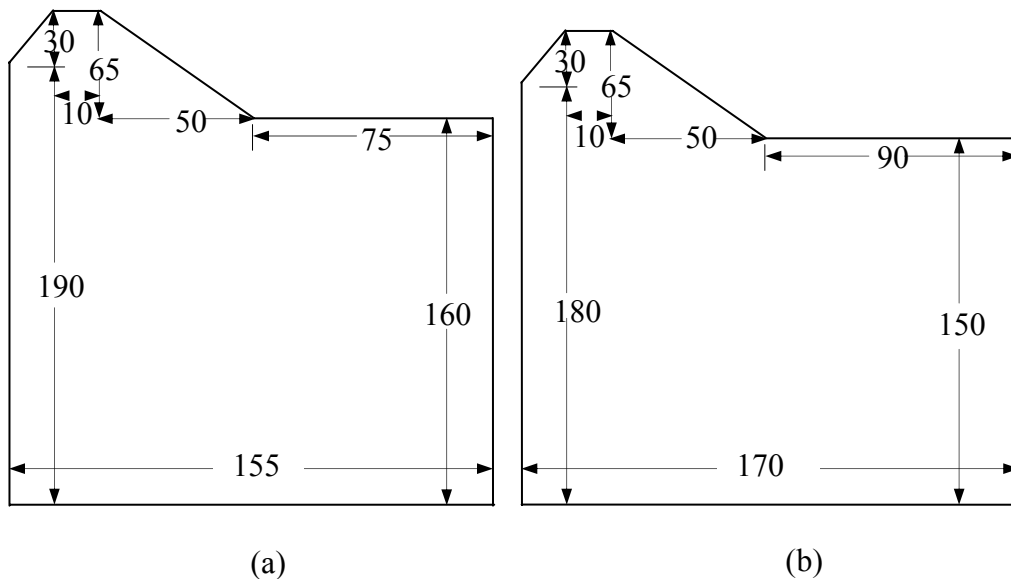
### 2.1.3 Model construction and operation

The weir bays and the undersluice bays were cast of concrete in formwork constructed specifically for the purpose (Fig. 2.3).



Figure 2.3 Concrete blocks for barrage bays

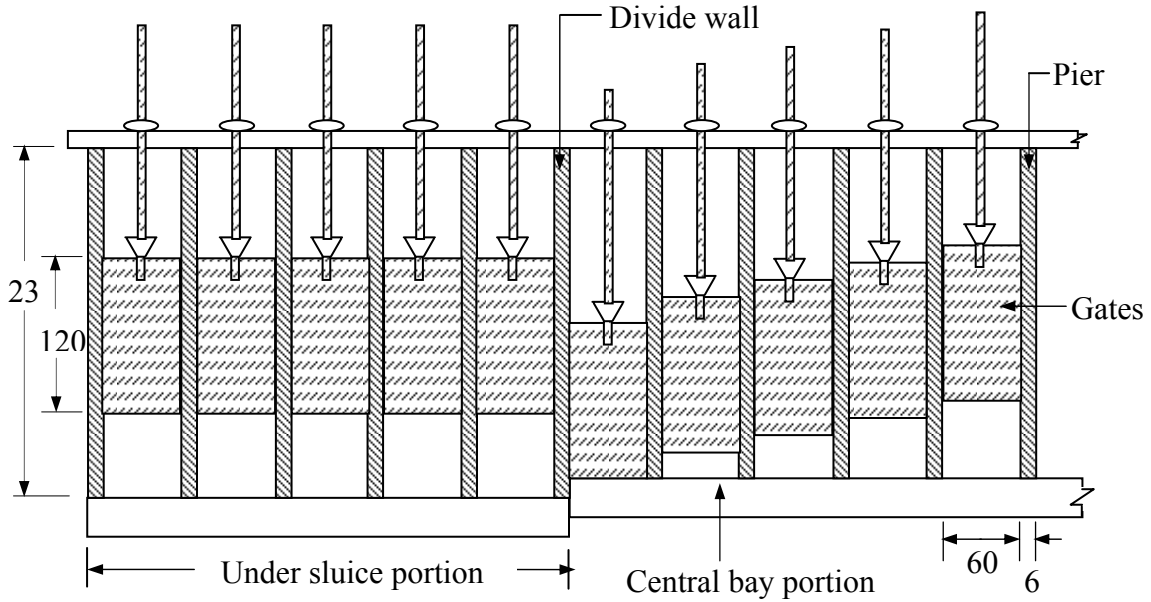
The model dimensions of the weir blocks of main river bays and the undersluice bays have been shown in Fig. 2.4.



All dimensions are in mm

Figure 2.4 Concrete blocks: (a) Spillway Bay and (b) Undersluice Bay

The rough casts were then chiseled out to obtain smooth surfaces. Intermediate piers were made of Perspex. The dimensions of the pier wall and gate arrangement have been shown in a close up view of the gate assembly in Fig. 2.5.



All dimensions are in mm

Figure 2.5: View of barrage gates from upstream

The entire setup was located in a river modelling tank of dimensions 5.1m (width) and 32m (length). The water was led into the tank from the upstream through a V-notch and a perforated baffle wall to damp any extra energy. The axis of the model barrage was located about 20m from the upstream end of the modelling tank. On the downstream, the water was collected in a depressed chamber through a wide tail gate.

The gates (34 in all) of the barrage model were first opened in above specified fashion. Water was made to run through the modelling tank, passing through the barrage. Discharge allowed was such to maintain maximum pool level (this condition was met in all the experiments). After attaining a stable pool level, wherein the level has to get stabilized, sand was fed into the tank some distance upstream of the guide bunds (at a distance of 4m upstream from the barrage axis). HIPS granules were fed into the tank in a controlled fashion using a hopper. The hopper was operated for uniform free fall of the granules.

As per the flow pattern prevailing under the site condition, the sand will tend to transport and get deposited in a particular pattern in the barrage near upstream. Experimentation was stopped when shoal formation had attained sufficient stability and the rate of bed load transport was observed to be less. This had taken around 24 to 28 hours to complete each set of experiment.

### Experiment 1: Partial gate operation

#### Experimental conditions:

Discharge = 80 litres per second

Upstream pool level = 110 mm

Downstream pool level = 60 mm

Gate operation sequence: (G denotes particular gate opening in mm)

G1	G2	G3	G4	G5	G6	G7	G8	G9	G1	G1	G1	G1	G1	G1	G1	G1
0	1	2	3	4	5	6	7	8	0	1	2	3	4	5	6	7
45	45	45	45	45	42	40	0	0	0	0	0	0	0	0	0	0
G1	G1	G2	G2	G2	G2	G2	G2	G2	G2	G2	G2	G3	G3	G3	G3	G3
8	9	0	1	2	3	4	5	6	7	8	9	0	1	2	3	3
10	18	25	25	40	40	50	50	50	50	55	55	50	50	50	50	50

#### Observations:

Observations were made for shoal heights using Laser Displacement Sensor (Appendix 2). Readings were taken at regular intervals of 10 cm in longitudinal direction and 5 cm in cross-sectional direction. The corresponding contour map (Fig. 2.6) and surface plot (Fig. 2.7) were drawn for the readings observed. Flow vector plots were drawn and are shown in Fig. 2.8.

### Experiment 2: Uniform gate operation

#### Experimental conditions:

Discharge = 90 litres per second

Upstream pool level = 110 mm

Downstream pool level = 60 mm

Gate operation sequence: (G denotes particular gate opening in mm)

G1	G2	G3	G4	G5	G6	G7	G8	G9	G1	G1	G1	G1	G1	G1	G1	G1
									0	1	2	3	4	5	6	7
50	50	50	50	50	30	30	30	30	30	30	30	30	30	30	30	30
G1	G1	G2	G2	G2	G2	G2	G2	G2	G2	G2	G2	G3	G3	G3	G3	G3
8	9	0	1	2	3	4	5	6	7	8	9	0	1	2	3	3
30	30	30	30	30	30	30	30	30	30	30	30	50	50	50	50	50

Observations:

Observations for shoal heights were done using Laser Displacement Sensor. Readings were taken at regular intervals of 10 cm in longitudinal direction and 5 cm in cross-sectional direction. Contour map (Fig. 2.9) and surface plot (Fig. 2.10) were drawn for the readings observed. Flow vector plots were drawn and are shown in Fig. 2.11.

### Experiment 3: Arch-type gate operation

Experimental conditions:

Discharge = 85 litres per second

Upstream pool level = 110 mm

Downstream pool level = 60 mm

Gate operation sequence: (G denotes particular gate opening in mm)

G1	G2	G3	G4	G5	G6	G7	G8	G9	G1	G1	G1	G1	G1	G1	G1	G1
									0	1	2	3	4	5	6	7
0	0	0	0	0	0	44	52	59	61	68	70	75	77	81	83	85
G1	G1	G2	G2	G2	G2	G2	G2	G2	G2	G2	G2	G3	G3	G3	G3	G3
8	9	0	1	2	3	4	5	6	7	8	9	0	1	2	3	3
85	83	81	77	75	70	68	61	59	52	44	0	0	0	0	0	0

Observations:

Observations were made for shoal heights and readings were taken at regular intervals of 10 cm in longitudinal direction and 5 cm in cross-sectional direction. Contour map (Fig 2.12) and surface plot (Fig. 2.13) were drawn for the readings observed. Flow vector plots were drawn and are shown in Fig. 2.14.

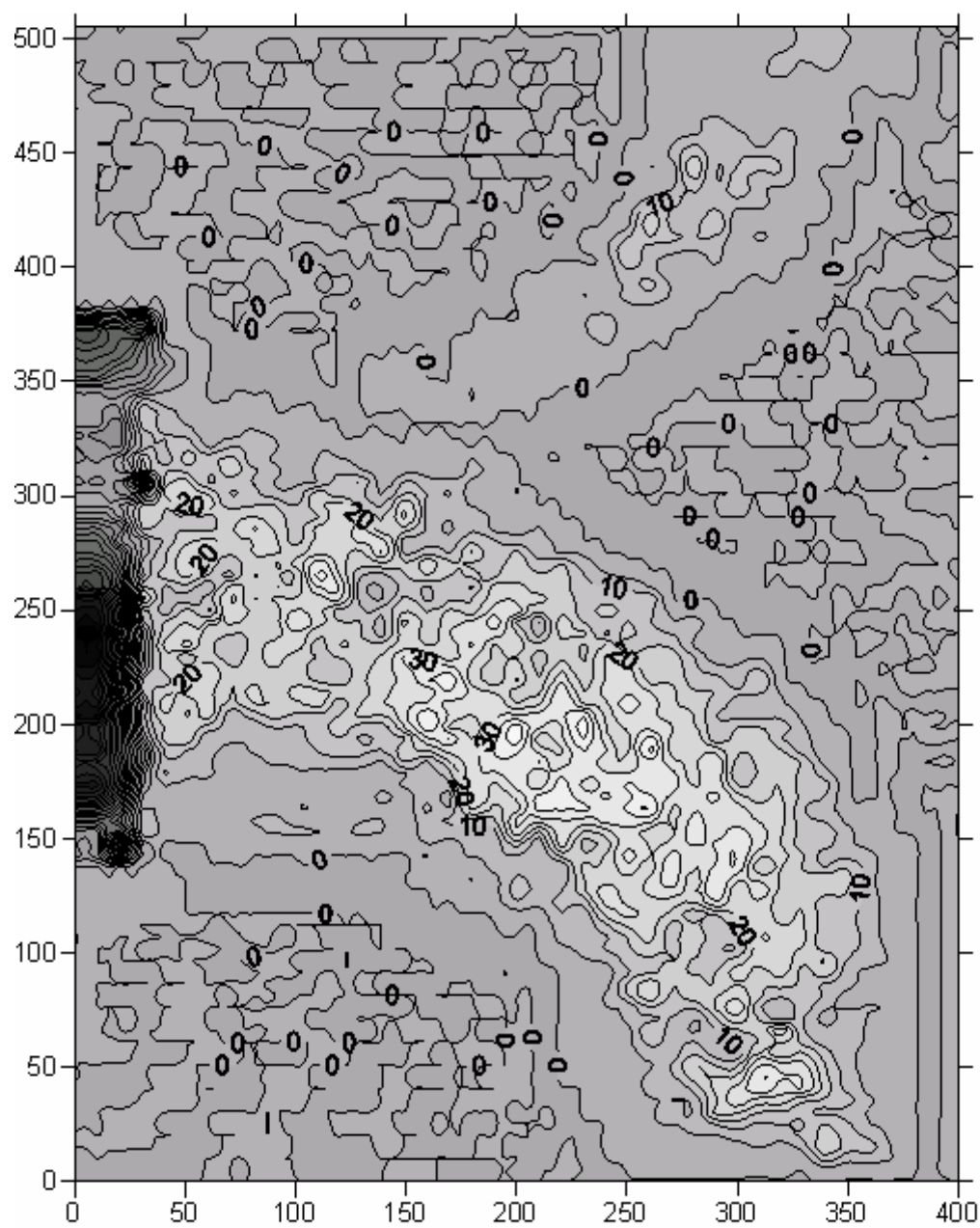


Figure 2.6 Bed contour map for experiment 1



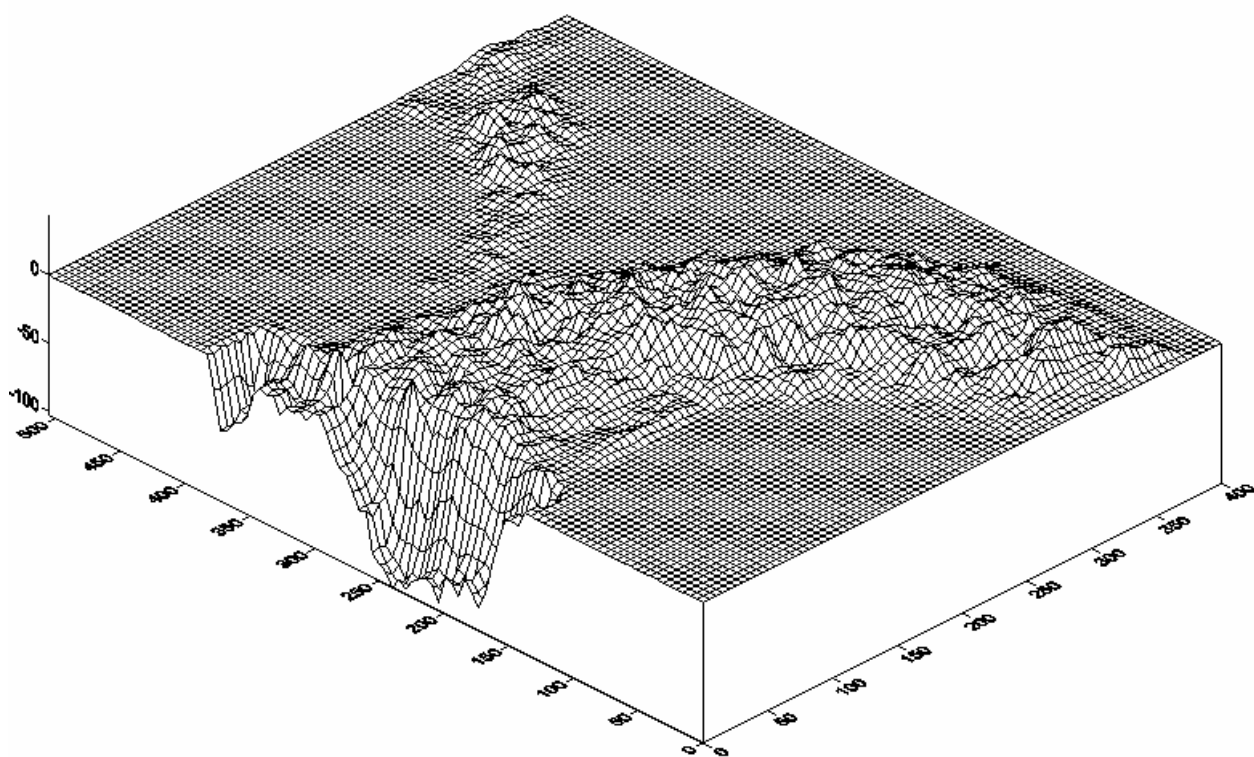


Figure 2.7 Surface plots for experiment 1

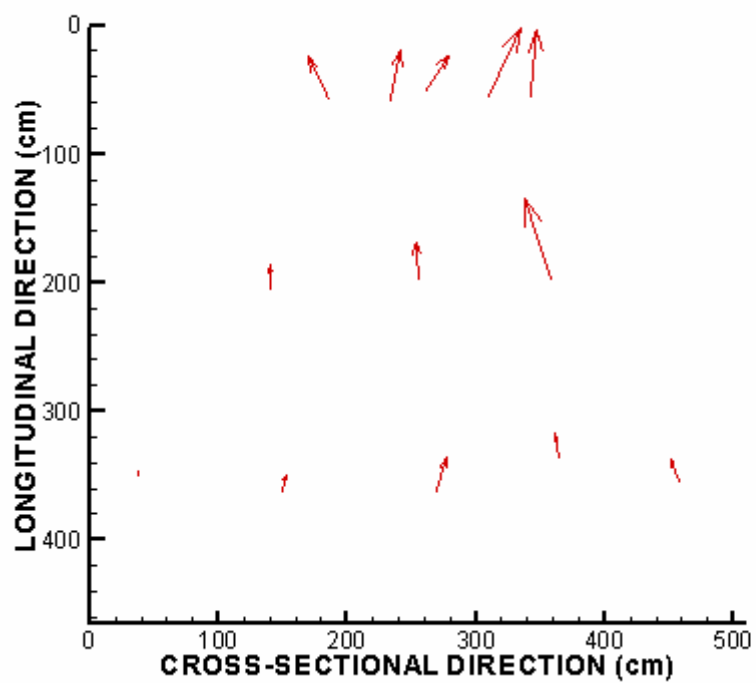


Figure 2.8 Flow vector for experiment 1

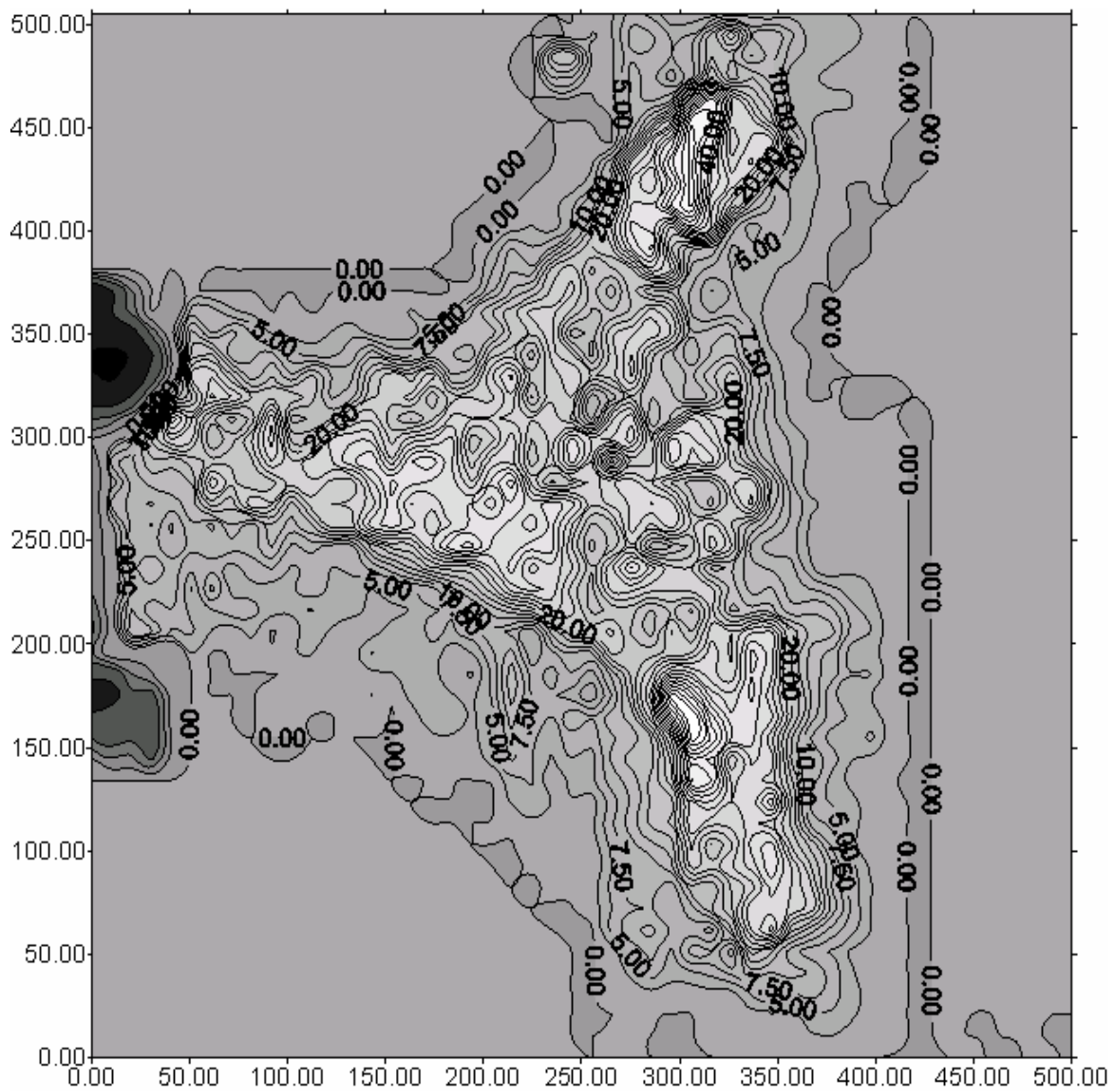


Figure 2.9 Bed contour map for experiment 2

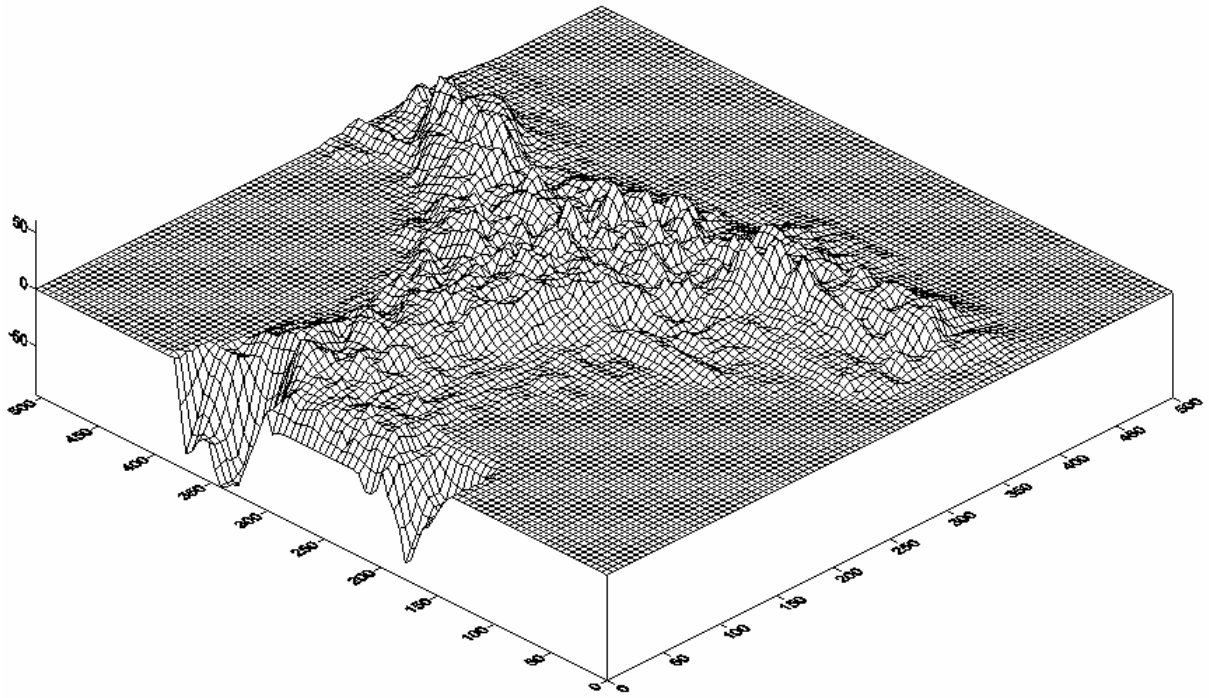


Figure 2.10 Surface plots for experiment 2

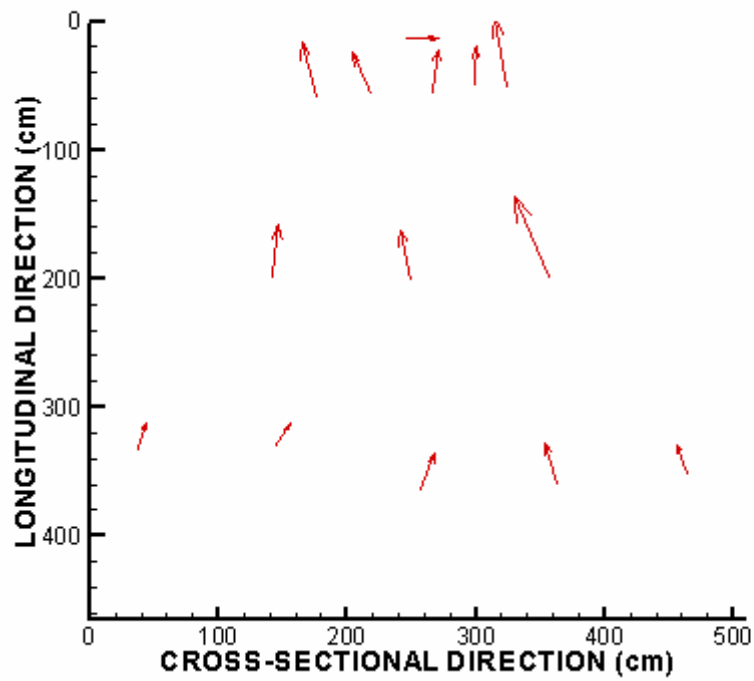


Figure 2.11. Flow vector for experiment 2

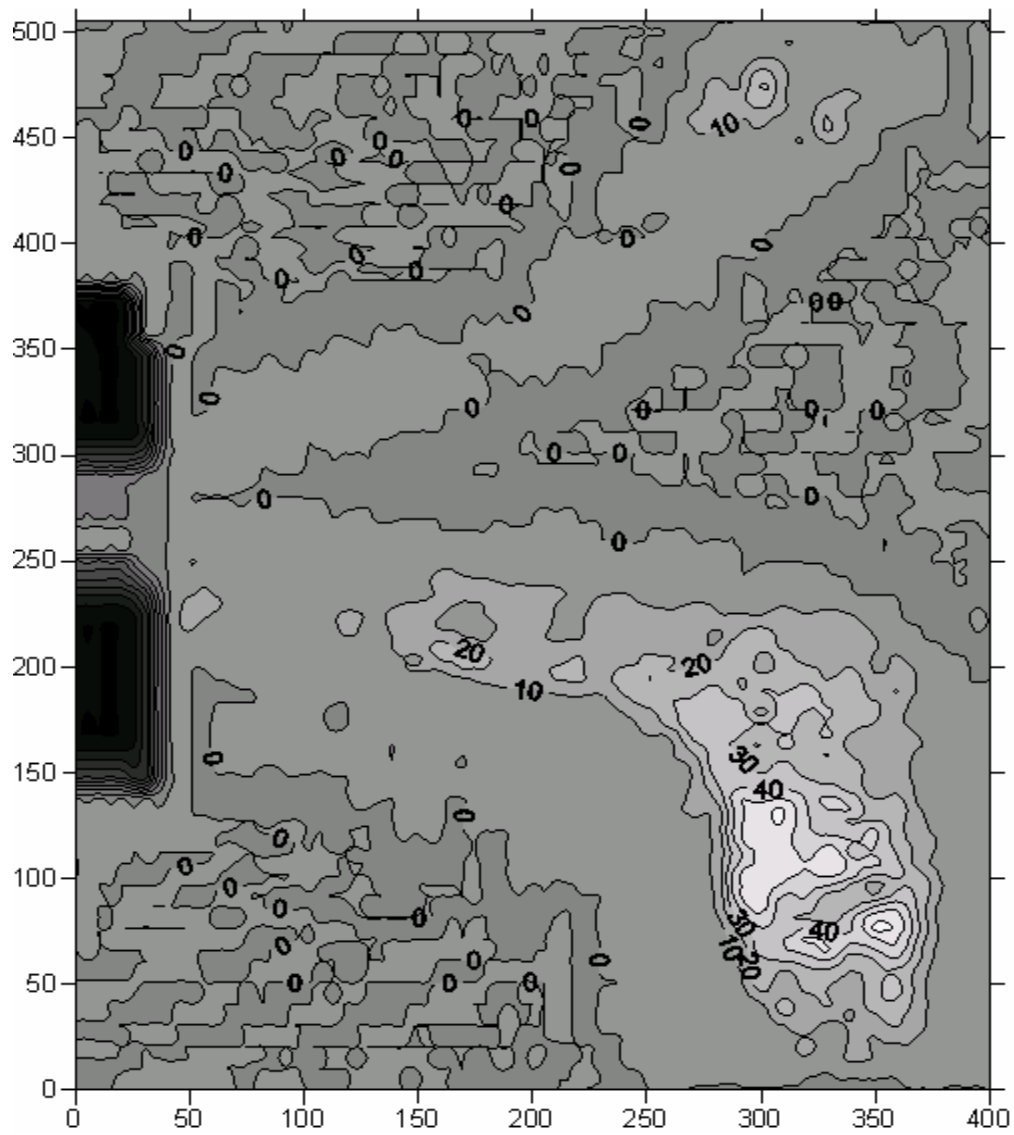


Figure 2.12 Bed contour map for experiment 3

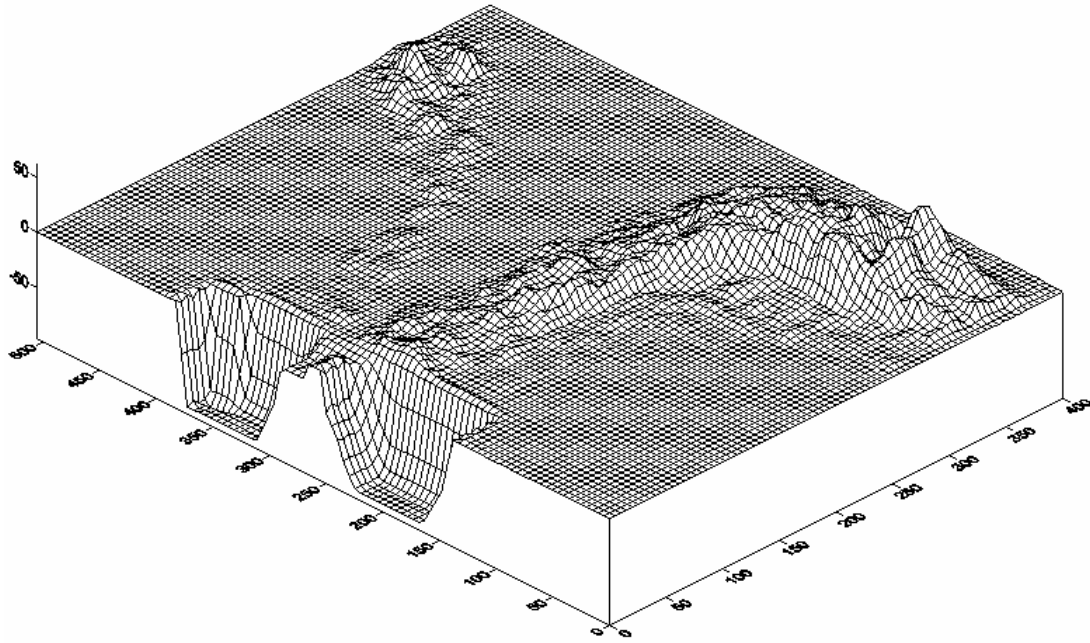


Figure 2.13 Surface plots for experiment 3

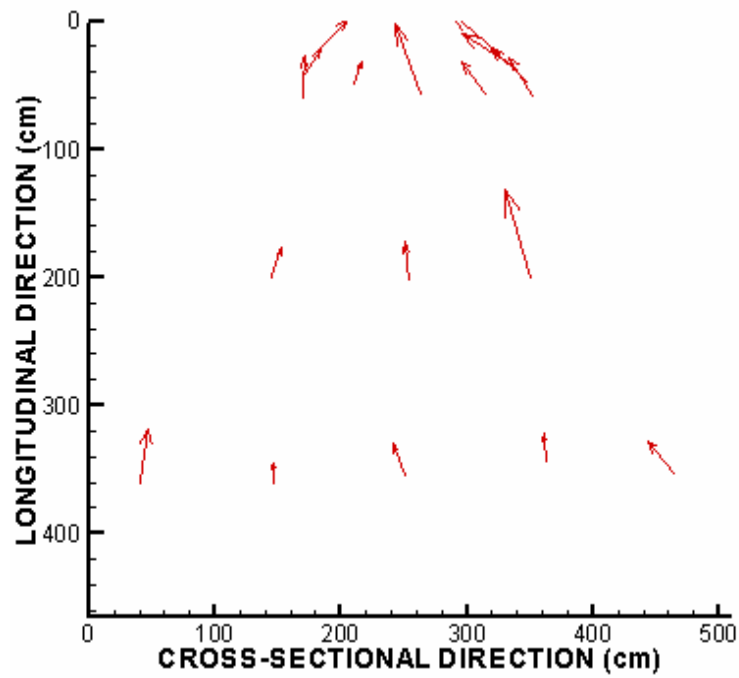


Figure 2.14 Flow vectors for experiment 3

#### **2.1.4 Analysis of shoal formation**

The set of experiments carried out under this study focuses mainly on bed load transport. Suspended load transport was completely neglected as there was no proper setup to generate the same. Even the sediment size was large enough to destroy any generation of suspended load in the flow. Actually, in real barrages suspended load plays a major role in sediment deposition and shoal formation upstream of barrage. Thus, this study restricts itself to bed load transport only.

The observation of sediment deposition pattern for different barrage gate opening condition reveals that shoal has formed, in general, where the gates are closed. It was observed that the shoal height was constantly decreasing towards the barrage. Larger shoal was found to be formed far from the barrage axis and near the barrage smaller dunes were formed.

Guide bunds divert entire river flow to a constricted barrage width. Vector plots for flow velocity shows that more velocity is generated adjacent to guide bund. This causes no shoal formation adjacent to entire guide bund length. Ripples were observed to form after some distance away from guide bunds and more shoal height was observed towards the centre of river width.

Uniform gate operation caused sedimentation in the entire region of study. This is a very rare case of regulation sequence for actual barrages, which has been studied. More shoals were formed towards the central region of river width. There was practically no sediment flushing observed in this operation sequence. Flow pattern observed in uniform gate operation reveals that there is considerable amount of flow parallel to barrage axis. This encourages cross scour just upstream parallel to barrage axis. Scour was observed to be more in the region around the divide wall, which is caused due to vortex generated by it.

Partial gate operation is a more general regulation pattern for actual barrages. Sediment deposition pattern observed for this case shows that more shoal has formed near the gates which were completely closed. As some of the gates were partially opened in an increasing opening sequence, the scour just upstream of barrage axis has also progressively followed the path. Where the gates were more open it paved way for sediment flushing through them. Surface plot shows the extent of bed exposure due to sediment getting flushed out.

Arch-type gate operation is the last case of study in this course for sediment deposition. In this case all the undersluice gates were completely closed and spillway gates were opened in an arch fashion. This gate opening pattern causes more flow velocity concentration towards the centre of river width. Further, the guide bunds again do the same purpose. Vector plot validates this observation. Sediment deposition pattern shows that there is much less shoal formation compared to other two cases. The reason behind this can attributed to greater sediment flushing through the barrage bays. Surface plot shows the extent of bed exposure due to sediment getting flushed out.

## **2.2 Effect of gate operation on flow pattern**

This study deals with flow pattern just upstream of barrage, and more primarily on ‘angle of attack’ of approaching flow to the barrage bays. Angle of attack is a composite phenomenon wherein many parameters comes into picture, like, physical conditions prevailing at the site, number of barrage gates, gate opening (condition and magnitude) of both spillway and undersluice bays, flow velocity, pool level, sediment deposition etc. Shoals formed in the upstream of barrage plays a major role in masking flow and generation of oblique flow into the barrage bays. This oblique flow is of designer’s interest which causes vortices over the spillway affecting design of stilling basin and prediction of scour downstream of the solid apron.

In the present model study the flow pattern and angle of attack was analyzed for gate operation condition only. Spillway gates were opened in a particular angle and undersluice gates were uniformly closed or opened for experimentation. Colour image processing has the pivotal role in analyzing the flow vector and finding the angle of attack.

### 2.2.1 Methodology for experimentation

Experiments were done on the barrage model for study of angle of attack for the approaching flow upstream of barrage. Right half of the barrage was chosen for observations. Observations were made for a sequence of gate opening in right undersluice and angled opening of right half of barrage spillway portion. The entire set of experiments were divided broadly into three phases considering gate opening in middle spillway gate (G18), angle of opening for other right spillway gates (G19 to G29), and right undersluice gates (G30 to G34). If we denote G18 gate opening as “a”, undersluice gates opening as “b”, angle of opening for other right spillway gates as “ $\delta$ ”, and angle of attack of flow as “ $\alpha$ ”, the entire set of experimentation can be explained in Fig. 2.15. Vector plots for flow just upstream of barrage and maximum angle of attack were shown in the subsequent experiments.

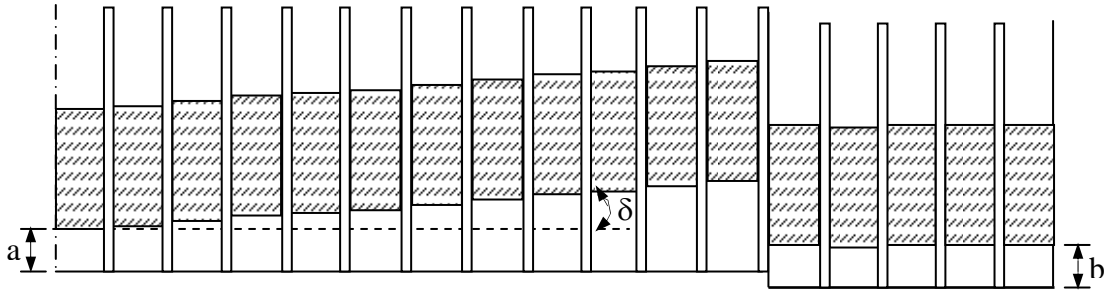


Figure 2.15 Sketch showing flow visualization experimental parameters a, b and  $\delta$

It may be mentioned that the engineer in charge of managing the gate operation of a barrage is often advised to open the gates in a wedge shaped pattern, with the gate openings varying from one end to the other. At the same time, the undersluice bays are almost always nearly kept opened to equal extents. Hence, this study attempts to investigate the effect of this kind of varied openings on the flow pattern in the pool behind the barrage. As mentioned earlier, the surface velocities were observed by capturing the images of floating thermocol particles released on the pool from above and comparing the subsequent images to analyse the flow vectors. The gate opening parameters and the respective flow patterns are provided in the subsequent pages.

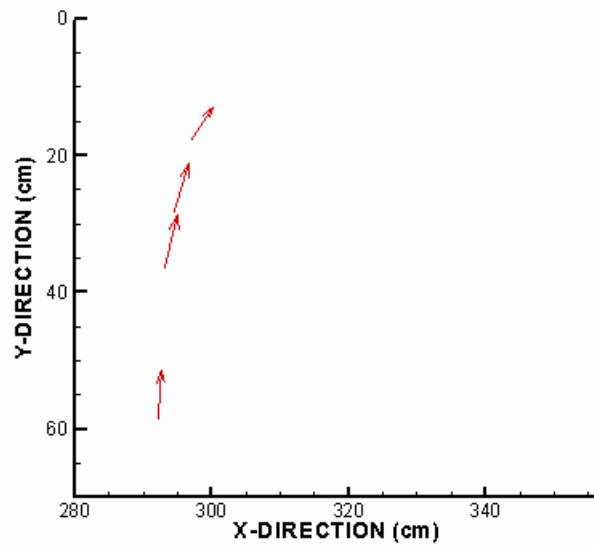


## Phase 1

### Experiment 1.1

$b = 0$ ;  $a = 0$ ;  $\delta = 4$  degrees

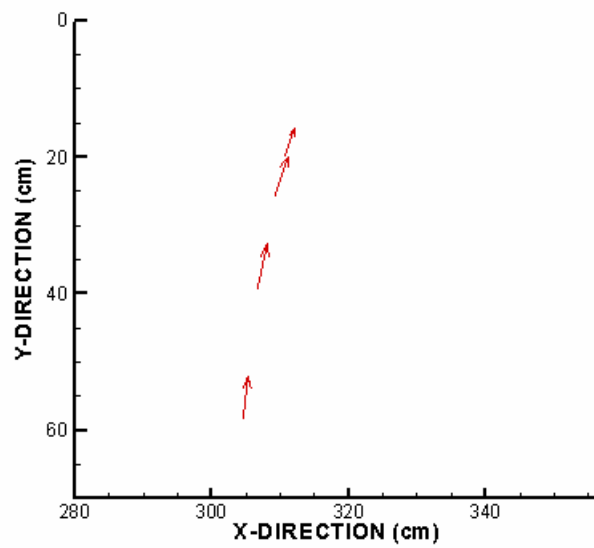
Observed  $\alpha_{\max} = 124.22$  degrees



### Experiment 1.2

$b = 0$ ;  $a = 0$ ;  $\delta = 5$  degrees

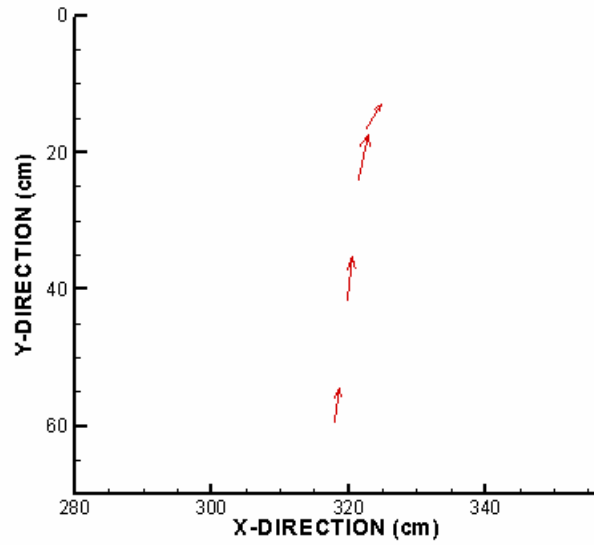
Observed  $\alpha_{\max} = 109.80$  degrees



### Experiment 1.3

$b = 0$ ;  $a = 0$ ;  $\delta = 6$  degrees

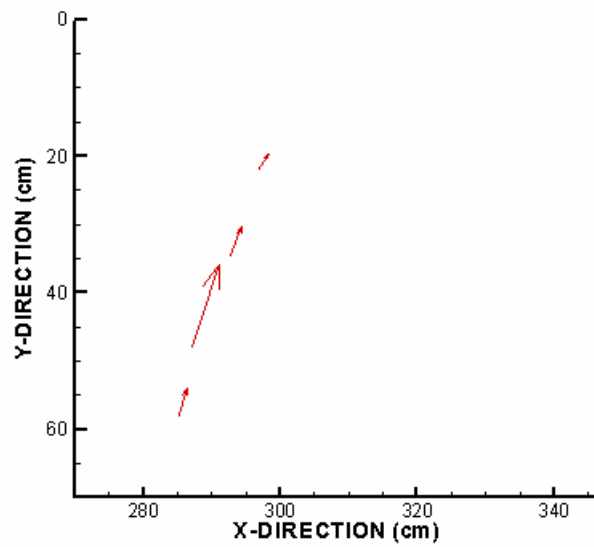
Observed  $\alpha_{\max} = 121.33$  degrees



### Experiment 1.4

$b = 0$ ;  $a = 0$ ;  $\delta = 7$  degrees

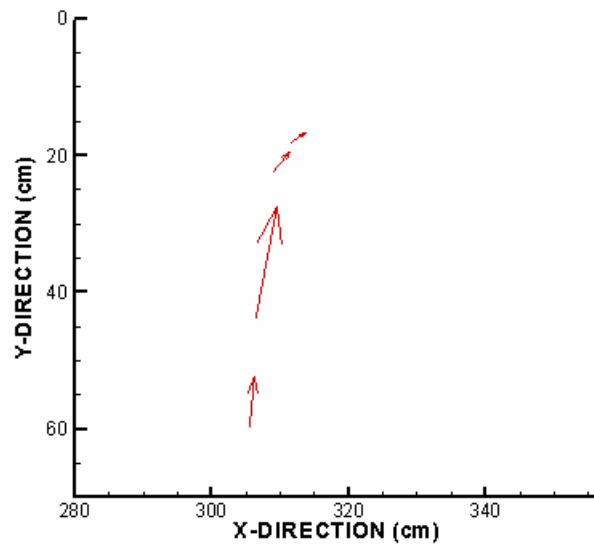
Observed  $\alpha_{\max} = 125.39$  degrees



### Experiment 1.5

$b = 0$ ;  $a = 5$  mm;  $\delta = 4$  degrees

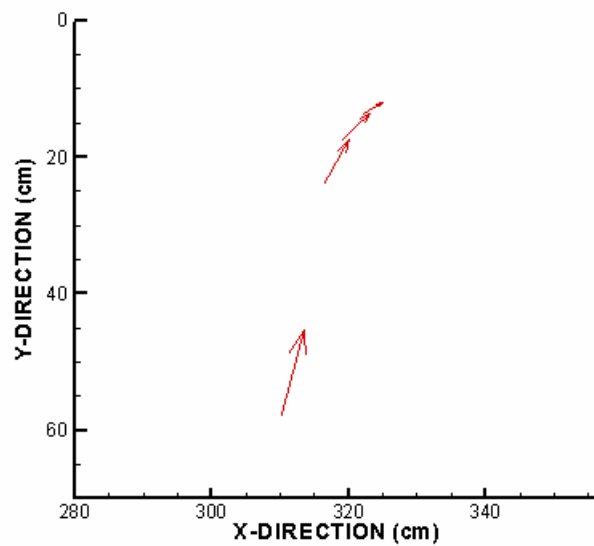
Observed  $\alpha_{\max} = 145.71$  degrees



### Experiment 1.6

$b = 0$ ;  $a = 5$  mm;  $\delta = 5$  degrees

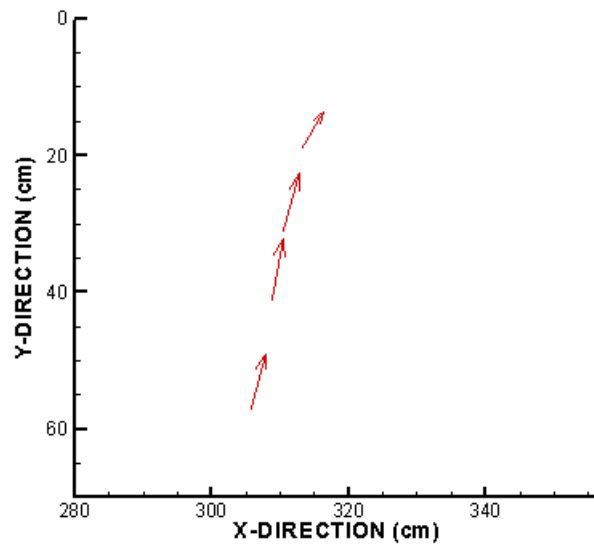
Observed  $\alpha_{\max} = 147.26$  degrees



### Experiment 1.7

$b = 0$ ;  $a = 5$  mm;  $\delta = 6$  degrees

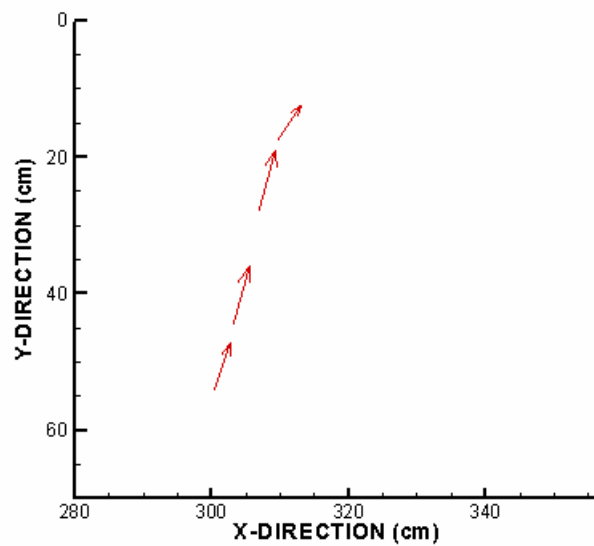
Observed  $\alpha_{\max} = 121.50$  degrees



### Experiment 1.8

$b = 0$ ;  $a = 10$  mm;  $\delta = 4$  degrees

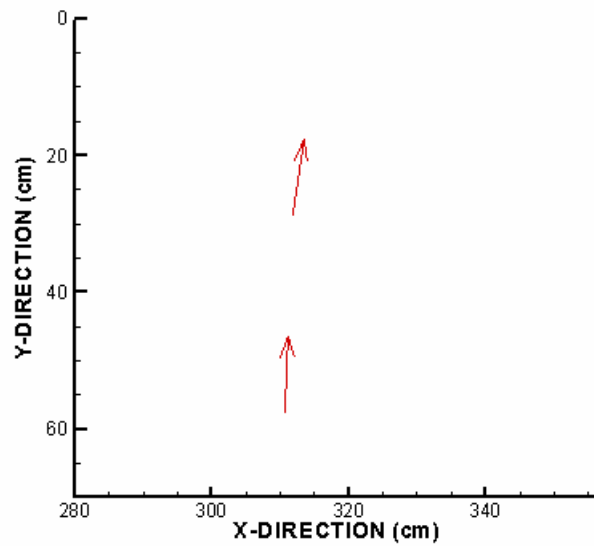
Observed  $\alpha_{\max} = 124.99$  degrees



### Experiment 1.9

$b = 0$ ;  $a = 10$  mm;  $\delta = 5$  degrees

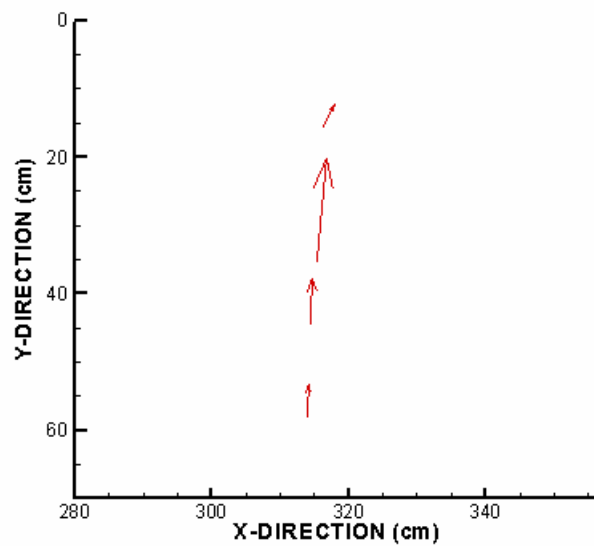
Observed  $\alpha_{\max} = 121.50$  degrees



### Experiment 1.10

$b = 0$ ;  $a = 10$  mm;  $\delta = 6$  degrees

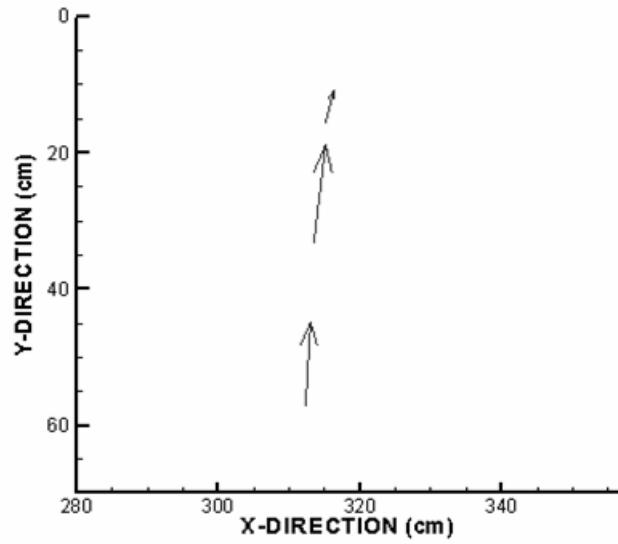
Observed  $\alpha_{\max} = 117.76$  degrees



### Experiment 1.11

$b = 0$ ;  $a = 15$  mm;  $\delta = 4$  degrees

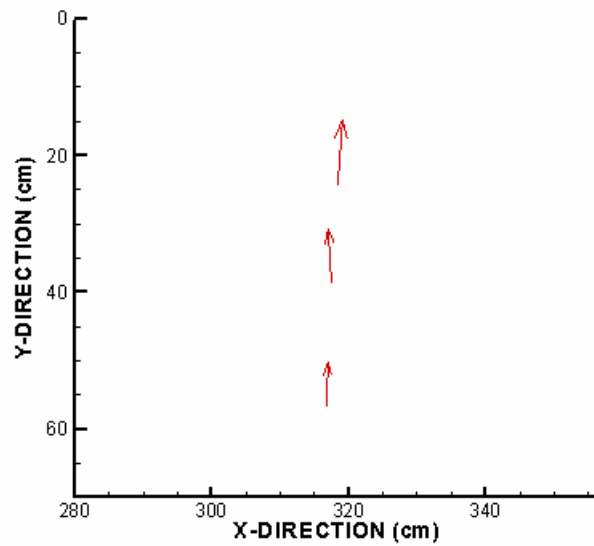
Observed  $\alpha_{\max} = 103.63$  degrees



### Experiment 1.12

$b = 0$ ;  $a = 15$  mm;  $\delta = 5$  degrees

Observed  $\alpha_{\max} = 94.51$  degrees

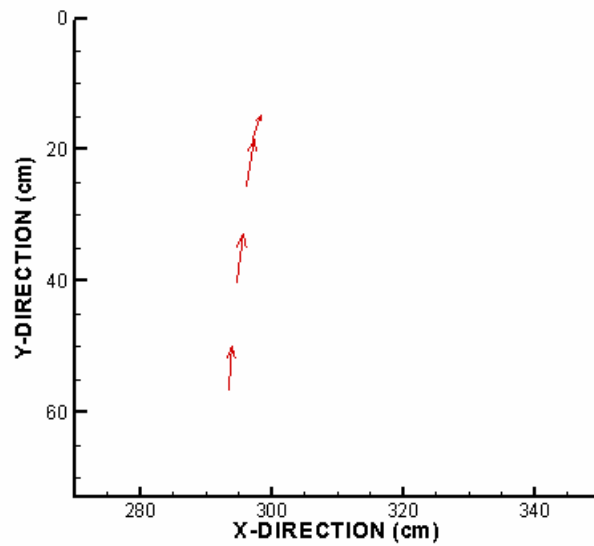


## Phase 2

### Experiment 2.1

$b = 15 \text{ mm}$ ;  $a = 0$ ;  $\delta = 4 \text{ degrees}$

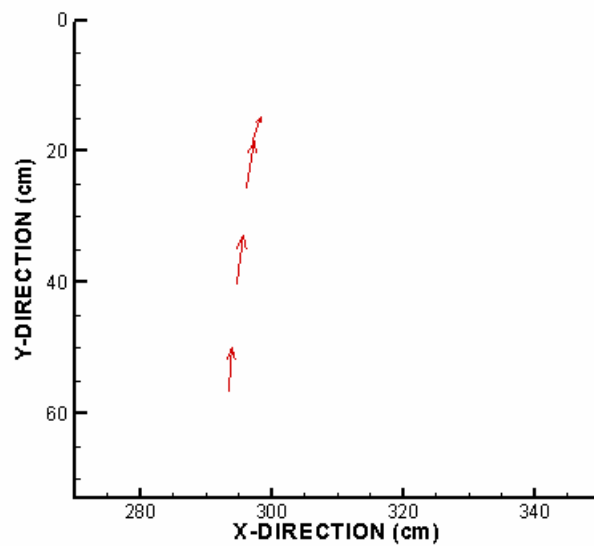
Observed  $\alpha_{\max} = 112.99 \text{ degrees}$



### Experiment 2.2

$b = 15 \text{ mm}$ ;  $a = 0$ ;  $\delta = 5 \text{ degrees}$

Observed  $\alpha_{\max} = 114.44 \text{ degrees}$

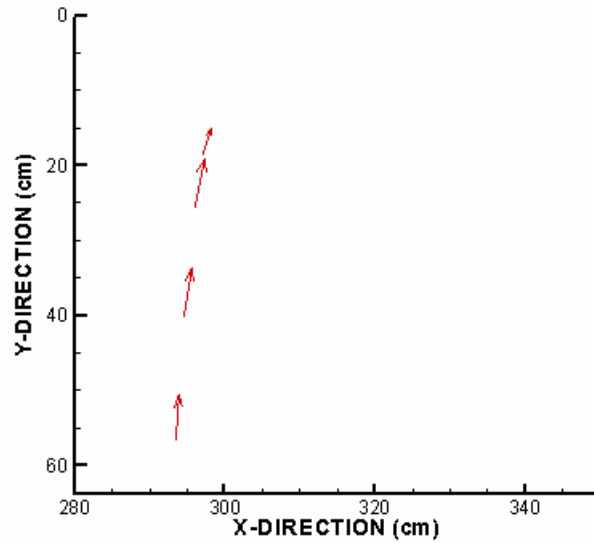




### Experiment 2.3

$b = 15 \text{ mm}$ ;  $a = 0$ ;  $\delta = 6 \text{ degrees}$

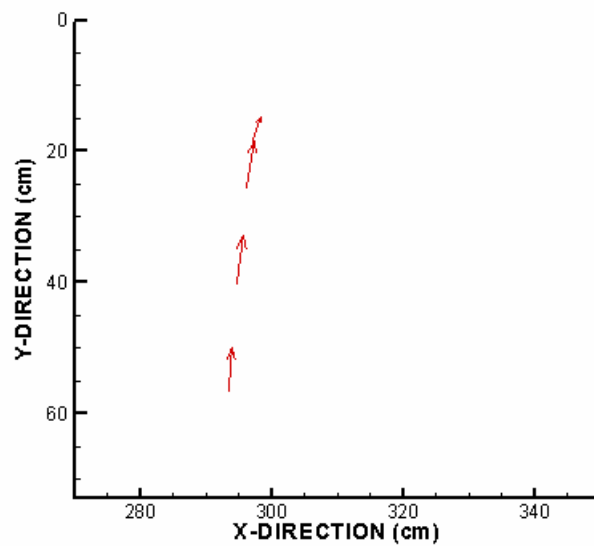
Observed  $\alpha_{\max} = 107.35 \text{ degrees}$



### Experiment 2.4

$b = 15 \text{ mm}$ ;  $a = 0$ ;  $\delta = 7 \text{ degrees}$

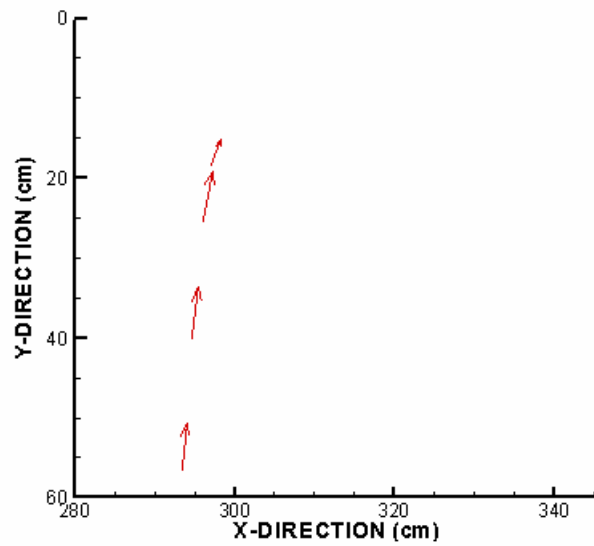
Observed  $\alpha_{\max} = 124.38 \text{ degrees}$



### Experiment 2.5

$b = 15 \text{ mm}$ ;  $a = 5 \text{ mm}$ ;  $\delta = 4 \text{ degrees}$

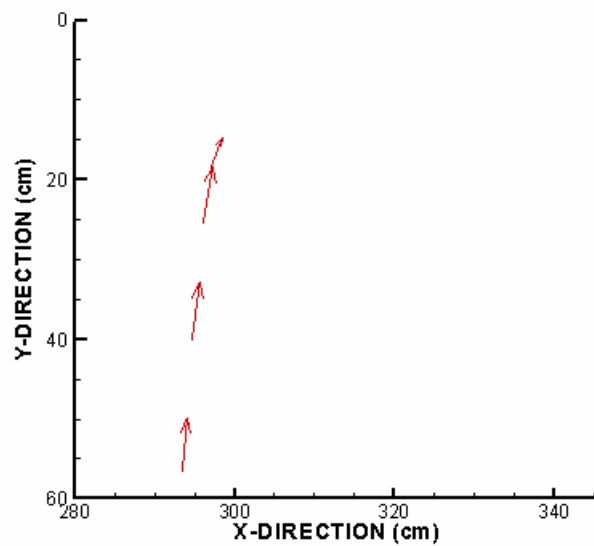
Observed  $\alpha_{\max} = 106.82 \text{ degrees}$



### Experiment 2.6

$b = 15 \text{ mm}$ ;  $a = 5 \text{ mm}$ ;  $\delta = 5 \text{ degrees}$

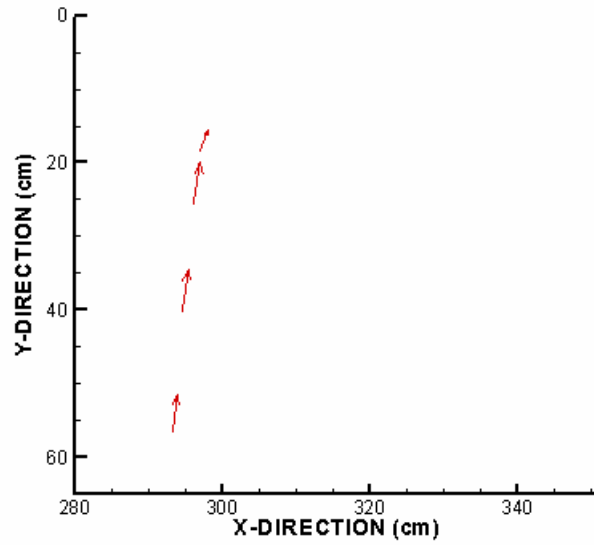
Observed  $\alpha_{\max} = 109.98 \text{ degrees}$



### Experiment 2.7

$b = 15 \text{ mm}$ ;  $a = 5 \text{ mm}$ ;  $\delta = 6 \text{ degrees}$

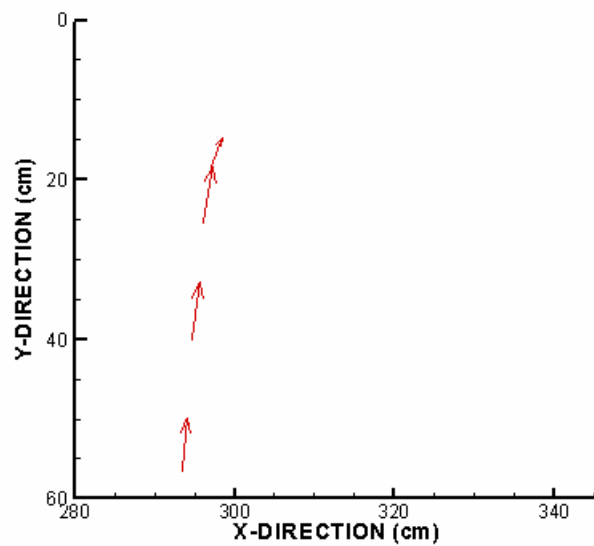
Observed  $\alpha_{\max} = 106.98 \text{ degrees}$



### Experiment 2.8

$b = 15 \text{ mm}$ ;  $a = 10 \text{ mm}$ ;  $\delta = 4 \text{ degrees}$

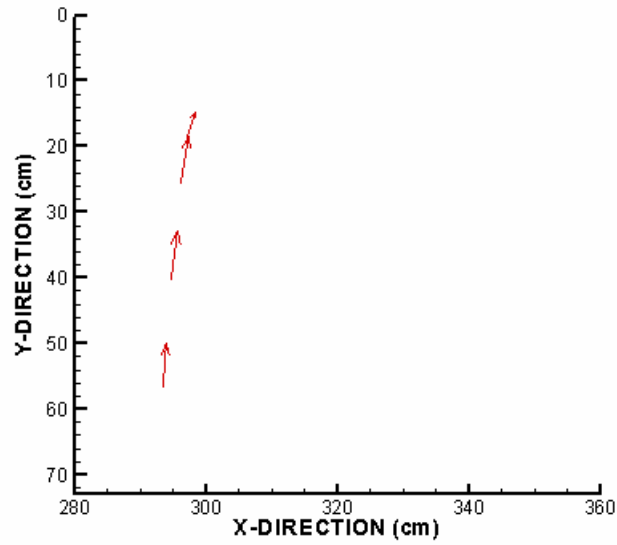
Observed  $\alpha_{\max} = 118.44 \text{ degrees}$



### Experiment 2.9

$b = 15 \text{ mm}$ ;  $a = 10 \text{ mm}$ ;  $\delta = 5 \text{ degrees}$

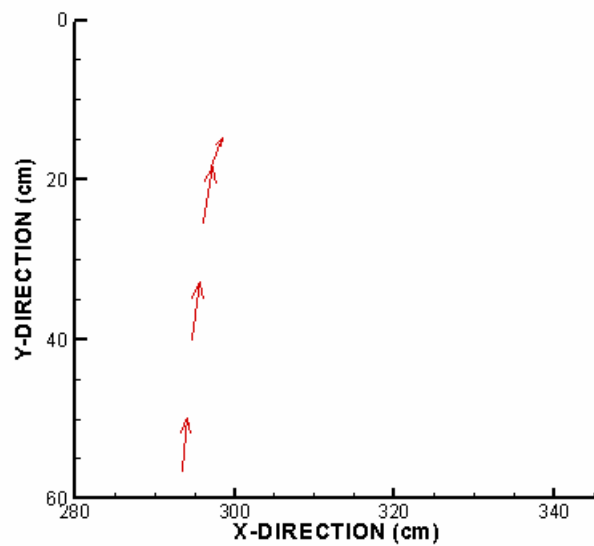
Observed  $\alpha_{\max} = 112.25 \text{ degrees}$



### Experiment 2.10

$b = 15 \text{ mm}$ ;  $a = 10 \text{ mm}$ ;  $\delta = 6 \text{ degrees}$

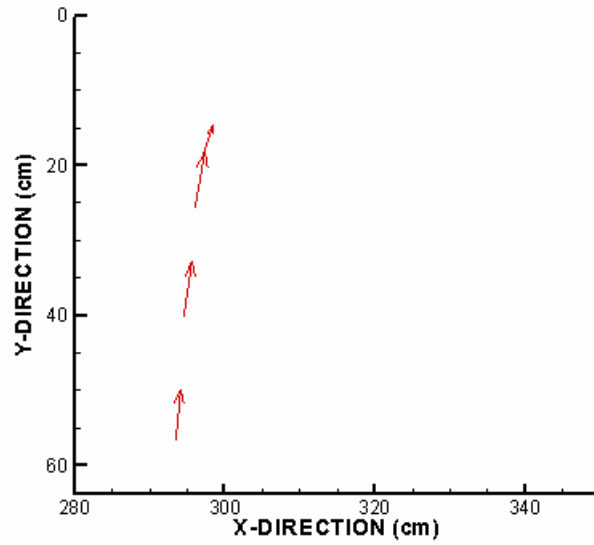
Observed  $\alpha_{\max} = 111.80 \text{ degrees}$



### Experiment 2.11

$b = 15 \text{ mm}$ ;  $a = 15 \text{ mm}$ ;  $\delta = 4 \text{ degrees}$

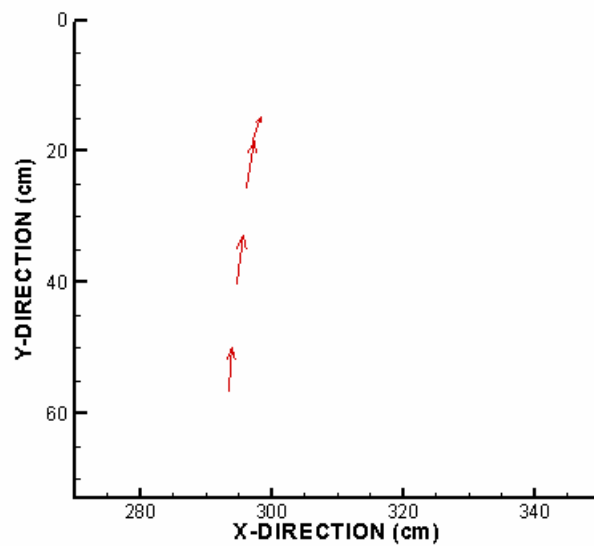
Observed  $\alpha_{\max} = 112.07 \text{ degrees}$



### Experiment 2.12

$b = 15 \text{ mm}$ ;  $a = 15 \text{ mm}$ ;  $\delta = 5 \text{ degrees}$

Observed  $\alpha_{\max} = 99.36 \text{ degrees}$

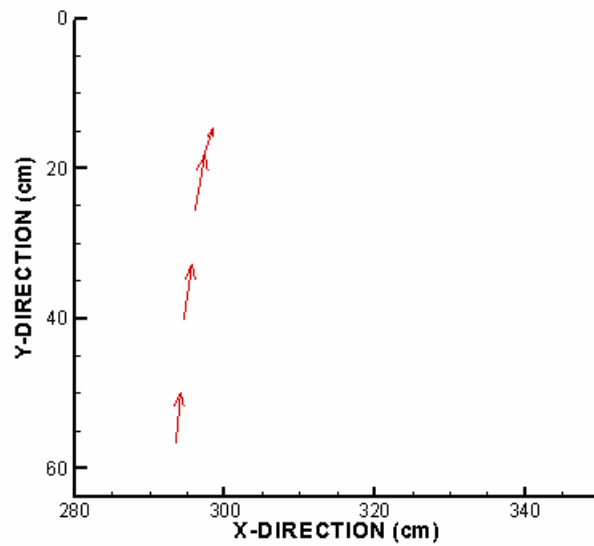


### Phase 3

#### Experiment 3.1

$b = 30 \text{ mm}$ ;  $a = 0$ ;  $\delta = 4 \text{ degrees}$

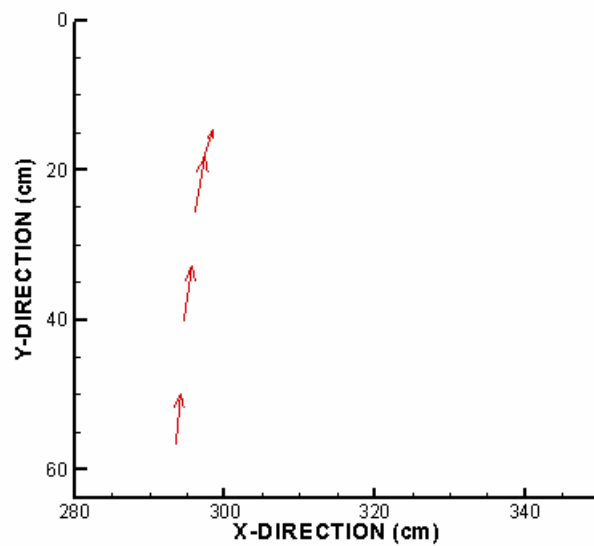
Observed  $\alpha_{\max} = 136.97 \text{ degrees}$



#### Experiment 3.2

$b = 30 \text{ mm}$ ;  $a = 0$ ;  $\delta = 5 \text{ degrees}$

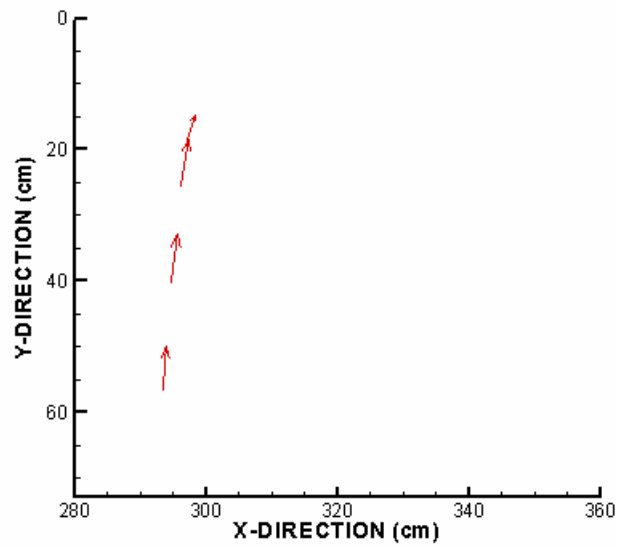
Observed  $\alpha_{\max} = 151.61 \text{ degrees}$



### Experiment 3.3

$b = 30 \text{ mm}$ ;  $a = 0$ ;  $\delta = 6 \text{ degrees}$

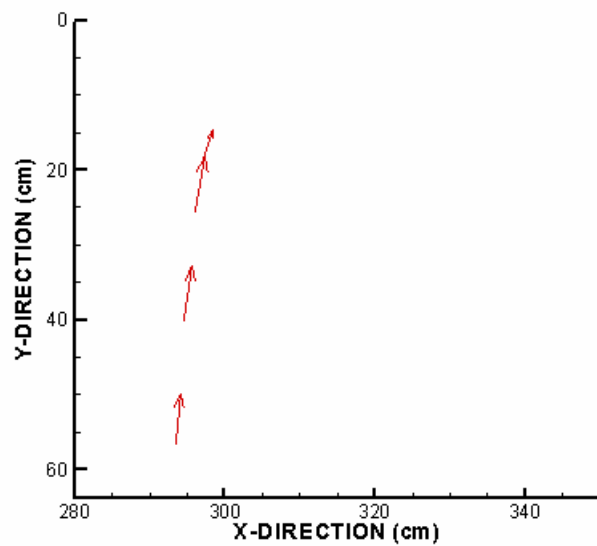
Observed  $\alpha_{\max} = 127.97 \text{ degrees}$



### Experiment 3.4

$b = 30 \text{ mm}$ ;  $a = 0$ ;  $\delta = 7 \text{ degrees}$

Observed  $\alpha_{\max} = 102.53 \text{ degrees}$

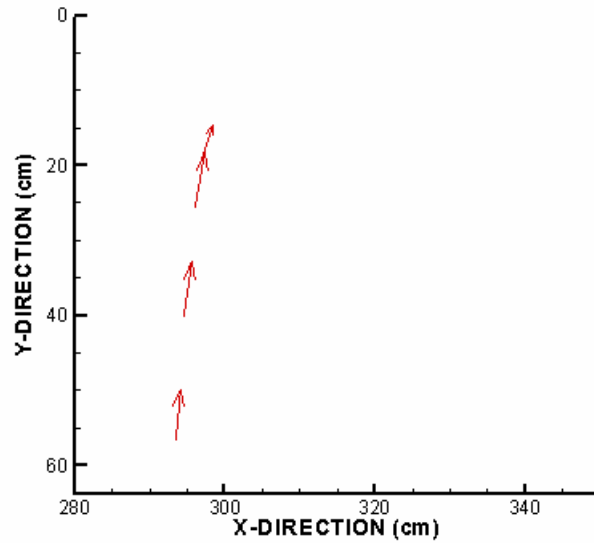




### Experiment 3.5

$b = 30 \text{ mm}$ ;  $a = 5 \text{ mm}$ ;  $\delta = 4 \text{ degrees}$

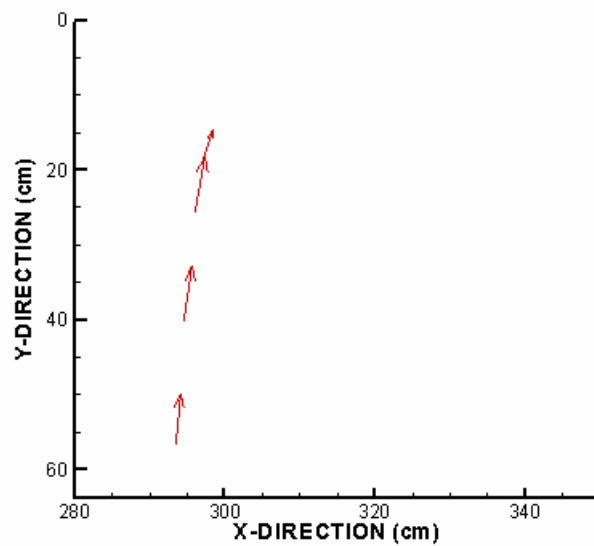
Observed  $\alpha_{\max} = 136.30 \text{ degrees}$



### Experiment 3.6

$b = 30 \text{ mm}$ ;  $a = 5 \text{ mm}$ ;  $\delta = 5 \text{ degrees}$

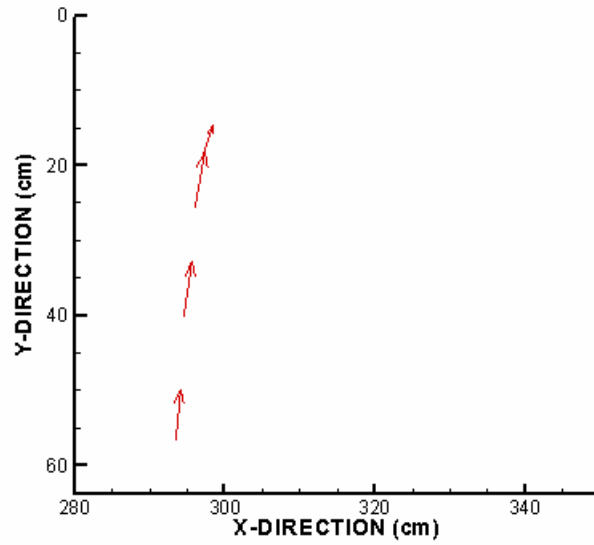
Observed  $\alpha_{\max} = 107.74 \text{ degrees}$



### Experiment 3.7

$b = 30 \text{ mm}$ ;  $a = 5 \text{ mm}$ ;  $\delta = 6 \text{ degrees}$

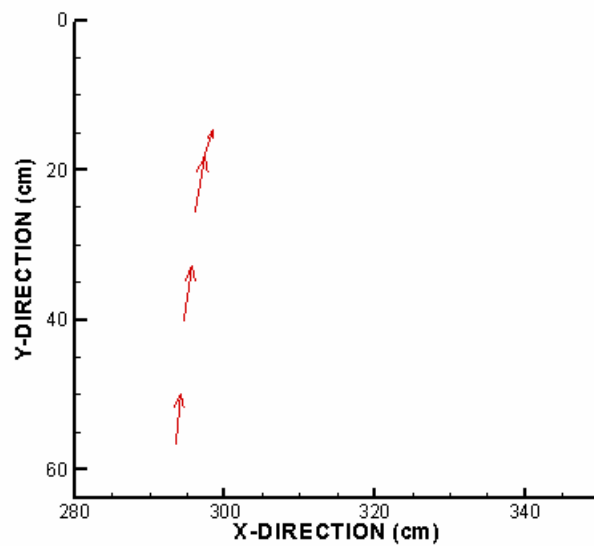
Observed  $\alpha_{\max} = 111.54 \text{ degrees}$



### Experiment 3.8

$b = 30 \text{ mm}$ ;  $a = 10 \text{ mm}$ ;  $\delta = 4 \text{ degrees}$

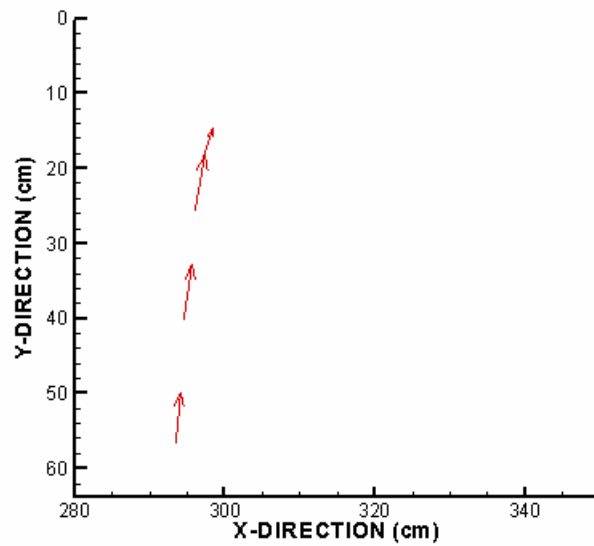
Observed  $\alpha_{\max} = 128.37 \text{ degrees}$



### Experiment 3.9

$b = 30 \text{ mm}$ ;  $a = 10 \text{ mm}$ ;  $\delta = 5 \text{ degrees}$

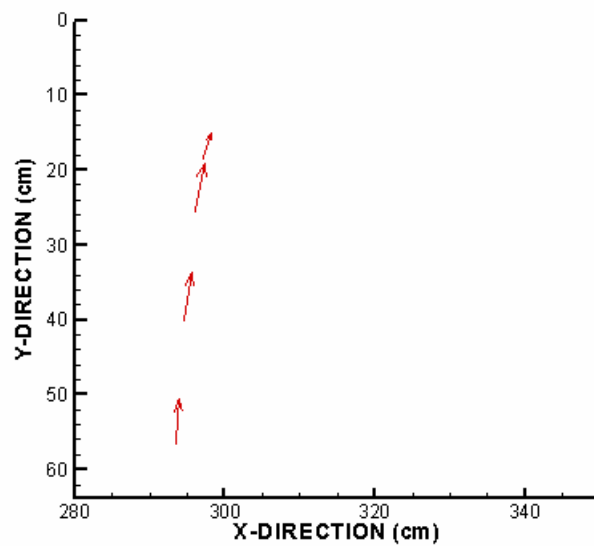
Observed  $\alpha_{\max} = 126.25 \text{ degrees}$



### Experiment 3.10

$b = 30 \text{ mm}$ ;  $a = 10 \text{ mm}$ ;  $\delta = 6 \text{ degrees}$

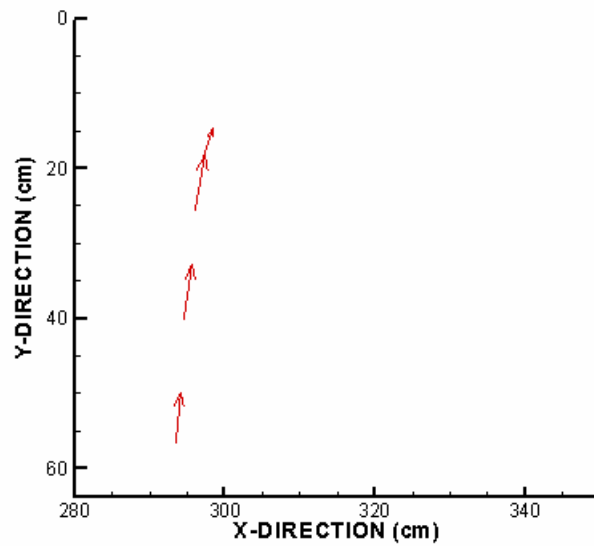
Observed  $\alpha_{\max} = 110.22 \text{ degrees}$



### Experiment 3.11

$b = 30 \text{ mm}$ ;  $a = 15 \text{ mm}$ ;  $\delta = 4 \text{ degrees}$

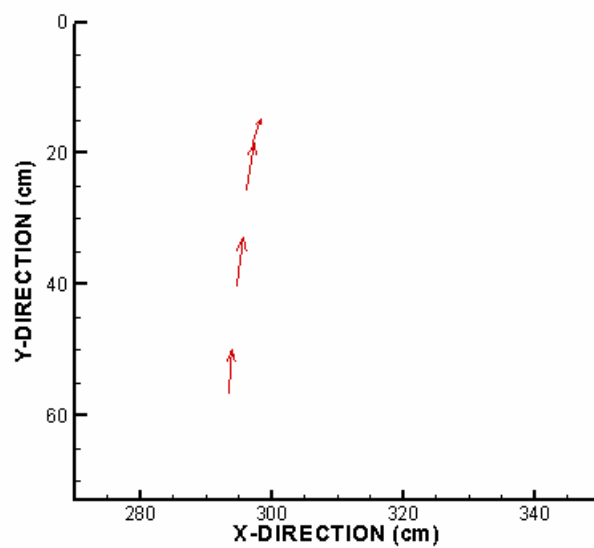
Observed  $\alpha_{\max} = 112.07 \text{ degrees}$



### Experiment 3.12

$b = 30 \text{ mm}$ ;  $a = 15 \text{ mm}$ ;  $\delta = 5 \text{ degrees}$

Observed  $\alpha_{\max} = 99.36 \text{ degrees}$



### 2.2.2 Inferences drawn from the experiments on flow patterns

The observed data shows that there is a mixed trend inherent in the phenomenon of angle of attack. Generally, the angle of attack increases with angle of gates opening. But there was found some break in the trend where in the angle of attack suddenly got decreased and again it started increasing with lesser magnitude. The cause for this observation can be attributed to the vortex generated across the divide wall and in-turn which causes change in water level in neighbouring bays of the divide wall (Fig. 2.16). The vortex effect counters the oblique flow into the spillway bays neighbouring the divide wall. It was observed that with larger angle of gate opening vortex generated across the divide wall starts increasing and tries to influence more number of spillway bays adjacent to divide wall. The vortex was even more when undersluice gates were completely closed. The decrease in water level in the spillway bays neighbouring the divide wall sometimes have caused uncontrolled flow over the spillway bays with water level well below the gate opening.

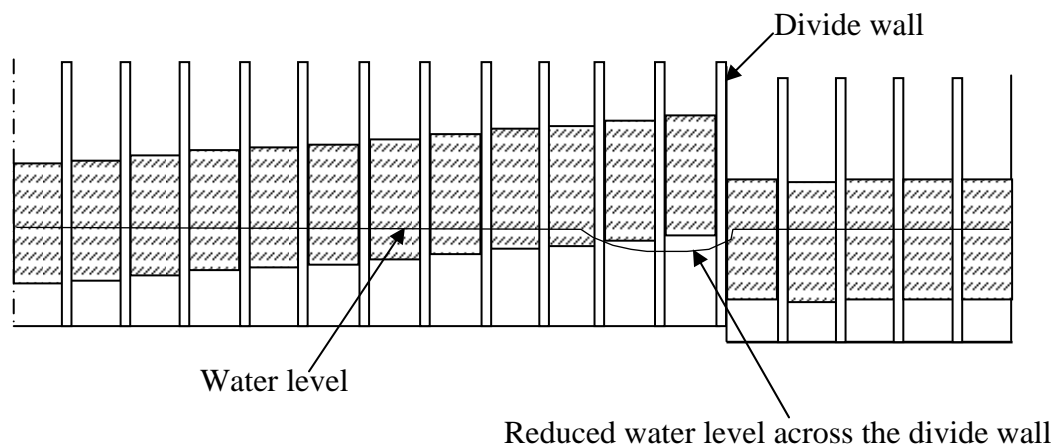


Figure 2.16 Sketch showing phenomena of reduction in water level across the divide wall

The reduced water level in neighbouring bays of the divide wall gives a scope for future investigation. This difference in water level across the divide wall can cause hydrostatic

pressure on the divide wall. So, the divide walls have to be designed taking this phenomenon also into consideration.

For larger angle of gate opening which is accompanied by increased velocity, there was more a linear kind of flow pattern observed because the velocity accompanied by these larger angles of opening were large enough to counter the vortex effect and oblique flow generated by gate operation. In fact with increasing 'a' value and greater 'δ' value, there was consistent decrease in the angle of attack 'α'. As such, the largest angle of attack was found to be 147 degrees, a deviation of as much as 57 degrees from the normal 90 degrees.

In the still pond system of barrage regulation, the undersluice gates are kept closed so long as the canal is flowing. The velocity of flow in the pocket is thus small and further the divide wall helps in separating the main flow in the river from the flow in the pocket. In this case as there is less flow velocity in the pocket, there won't be much vortex generation across the divide wall and angle of attack increases with increasing angle of gate opening. After some period of still pond operation, sediment gets deposited in the pocket and the canal starts drawing sediment. Under such conditions, the canal is closed and the deposited material is scoured away by opening the undersluice. Still pond system of operation has been found to be a satisfactory method for sediment control and can give much better results than the semi-open flow system.

In the semi-open flow system, the undersluice gates are kept partially open while the canal is flowing. This increases the flow velocity in the pocket and hence brings more sediment into the pocket. This sediment is continuously washed out through the under-sluices. This system has the advantage that since sediment is continuously flushed through the undersluices, the bed level in the pocket is lower than that in the former system. But as there is some flow velocity in the pocket it encourages generation of vortex across the divide wall and can cause extensive scour around the divide wall. Also there is constant churning of sediment particle in the pocket which can cause canal to draw sediment. With increase in undersluice opening there is drawing of more water in the pocket causing increase in angle of attack in the spillway bays. Observation data shows that with increase in 'b' value there is increase in 'α' value. Hence, this system is not advocated except during high floods.

Another interesting event observed was the generation of small local vortices around the upstream of the barrage piers (Fig. 2.17). These vortices force a part of incoming flow jump

over to immediate next bay, encouraging parallel flow just upstream of barrage axis. Further studies can be done on this observation to help fixing the projection of piers from the barrage crest.

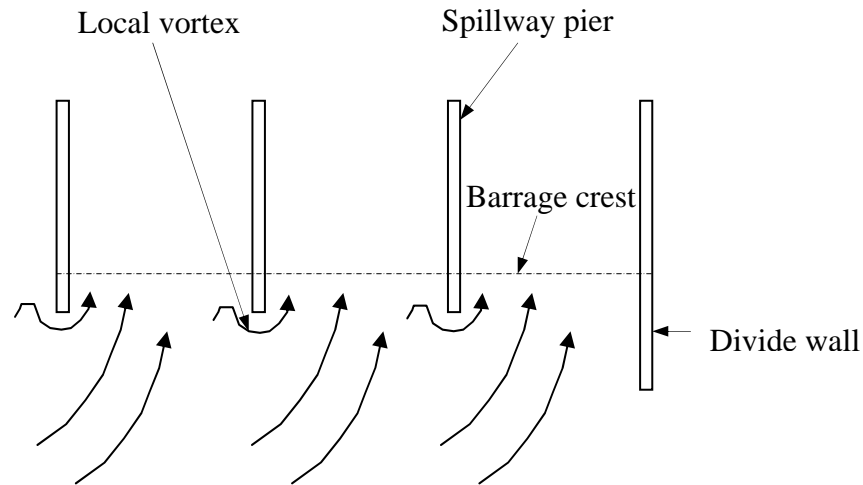


Figure 2.17 Figure showing local vortex around spillway piers

The observation of oblique flow caused due to gate operation validates the cause for increased estimation of approaching flow through the spillway bays. Present Indian practice allows for 20 percent increment in the estimation of incoming discharge over the spillway bays. Further studies can be done on this to find more accurate and sound percentage value.

This entire discussion can give an insight for designers and planners of the barrage on the concept of oblique flow. Thus, the designers should take due care on the concept of angle of attack and its effects on the design of stilling basin and scour after that. Designers should incorporate this phenomenon in their design for fixing up of barrage width, bay width and number of bays. The formation of shoals and its accompanied generation of oblique flow add more to the problem. The planners of the barrage should give sufficient importance to this phenomenon in drawing a proper barrage regulation sequence.

### Reference:

Novak, P. and Cabelka, J. (1981). *Models in Hydraulic Engineering: Physical Principles and Design Applications*. Pitman Advanced Publishing, Inc.



## CHAPTER 3

### UNIFORM GATE OPERATION

#### **3.1 Uniform gate operation condition**

As such, uniform gate opening for the entire barrage is not always possible to be maintained by the engineer in charge of barrage operation because of certain operational considerations as discussed earlier. However, quite often some or a few adjacent bays of the barrage may be opened to the same extent. This section discusses the experimental setup to investigate into the flow characteristics and its effects on scour for this condition.

##### **3.1.1 Objective of the study**

The data obtained from experimental observations under uniform flow conditions were collected to study the following:

1. To find out a formula for the maximum scour and its location based upon the different flow variables.
2. To model the scoured profile using Artificial Neural Networks (ANN)
3. To analyse the flow field with a numerical model using a commercially available CFD software FLUENT
4. To identify the significant parameters affecting scour

#### **3.2 Experimental setup and materials used**

Investigations into the behaviour of scour for the four distinct hydraulic conditions were carried out by the authors in a physical model representing three bays of a typical barrage in a 12m long, 0.90m wide and 0.7m deep horizontal flume. The model, made of Perspex (Fig. 3.1), was located within the glass walled section of the flume. The 0.02 m wide crest of the weir was kept at 0.075m and 0.04m above the downstream stilling basin apron and upstream rigid bed elevations respectively. The 0.76m long stilling basin consisted of a 0.015m high end-sill at its downstream end. The upstream and downstream slopes of the glacis of the weir were inclined at 1H: 1V and 3H: 1V. The concrete block composed flexible apron was replaced by a sand bed since during high scouring conditions, the apron material generally

gets washed out or sinks below the underlying sand. Hence, just downstream of the solid floor representing the stilling basin apron, a sand bed of 1.8 m length was installed to study the scouring. The entire setup was a part of a recirculatory flume at the Indian Institute of Technology at Kharagpur. At the test section the transparent glass walls of the flume were fitted with a scale for visual inspection and tracing of the scour profile. The water levels were measured by point gauges placed on the upstream and downstream ends of the model and at the weir section. While carrying out the experiments, all three gates of the model were operated independently, though in this paper the studies conducted for uniform gate openings only have been reported. The properties of sands used are summarized in Table 3.1 and the flow variables attempted with are shown in Table 3.2.

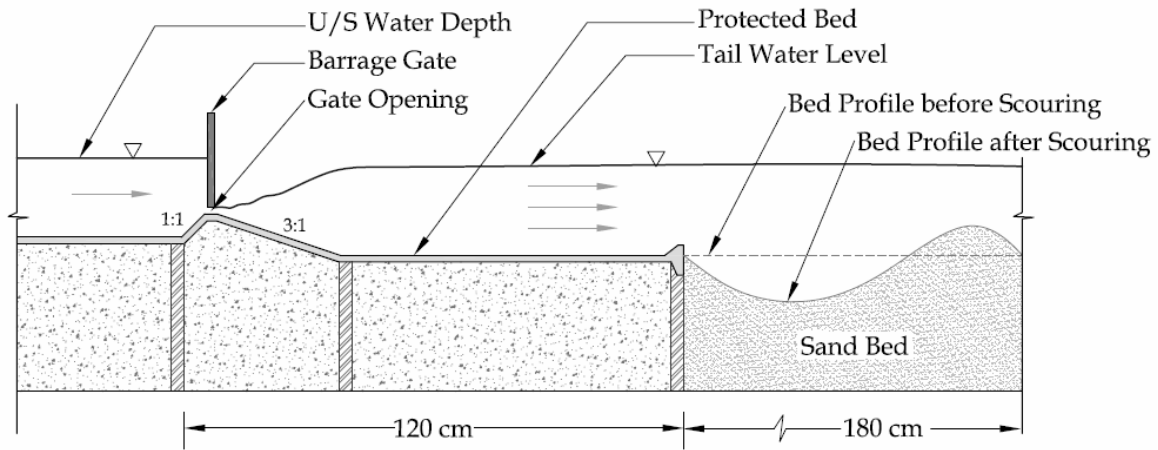


Figure 3.1 Experimental setup for conducting uniform flow experiments

Table 3.1 Details of bed material used for the experiments

Type of sediment	Sample	Median diameter $d_{50}$ (mm)	Relative density $s$	Porosity $\rho_o$	Geometric standard deviation $\sigma_g$	Angle of repose $\varphi$ (degree)
Uniform	A	0.24	2.65	0.42	1.38	29.0
	B	0.49	2.65	0.41	1.24	29.5
	C	0.92	2.65	0.40	1.17	30.0

Table 3.2 Range of Experimental Data (Head and Tail water levels are measured relative to the elevation of the solid apron)

Sl. No.	Parameter	Units	Range
1	Gate opening (for controlled flow)/ Depth of flow above crest (for uncontrolled flow) ( $G$ )	m	0.02 - 0.25
2	Head water (upstream) level, $H_u$	m	0.153 - 0.525
3	Tail water (downstream) level, $H_d$	m	0.105 - 0.258
4	Incoming discharge per unit width, $q$	m <sup>2</sup> /s	0.0298 – 0.0807
5	Mean velocity at crest, $U$	m/s	0.40 – 2.35
6	Mean bed material size $d_{50}$	m	0.00024-0.00092

### 3.3 Experimental observation procedures

At the start of the experiment to obtain the data, the discharge was increased slowly to predefined discharge,  $Q$ , which is maintained constant until the formation of the asymptotic scour hole. During this period, the bed profile was measured at different time intervals through the glass wall. When the bed profile reached an equilibrium stage, the velocity profile of instantaneous velocity components were then measured at selected sections using ADV (Acoustic Doppler Velocimeter). The ADV, of SONTEK make, measures the instantaneous velocity vector at a number of sections within a water column. The ADV operates on a pulse-to-pulse coherent Doppler shift to provide a three-component velocity at a rate of 25 Hz. Acoustic waves with a frequency of  $f_o$  are emitted by a transducer (emitter). These waves pass through a water column and arrive at the measuring point which is located about 5 cm below (for down looking ADV) the transducer. At this point they are reflected by the ambient particles within the flow (the air bubbles in the turbulent open channel flow). The waves reflected toward the receiver have a frequency  $f_r$ . The difference between  $f_o$  and  $f_r$  is the Doppler Shift frequency. Each receiver of the ADV measures the projection of the 3D water velocity onto its bistatic axis by detecting the Doppler-shift frequency. The bistatic axis is the midaxis between the receiver and the transmitter axis. Knowing the relative orientation of the three bistatic axes for the three receivers allows calculation of the 3D water velocity. Because of the inference due to echoes from the

boundaries (flume bed or water surface), the received signal might be disturbed, which may result in inaccurate velocity measurement. In this study, a few points near the bed were found to be influenced in this way. The velocity measurement by the ADV probe was not possible in the zone, which was 5cm below the free surface. The ADV readings were taken along several vertical lines at different section along the flume.

The ADV conceived and developed by SONTEK, measures the instantaneous velocity vector at a number of sections within a water column. The ADV operates on a pulse-to-pulse coherent Doppler shift to provide a three-component velocity at a rate of 25 Hz. Acoustic waves with a frequency of  $f_0$  are emitted by a transducer (emitter). These waves pass through a water column and arrive at the measuring point which is located about 5 cm below (for down looking ADV) the transducer. At this point they are reflected by the ambient particles within the flow (the air bubbles in the turbulent open channel flow). The waves reflected toward the receiver have a frequency  $f_r$ . The difference between  $f_0$  and  $f_r$  is the Doppler Shift frequency. Each receiver of the ADV measures the projection of the 3D water velocity onto its bistatic axis by detecting the Doppler-shift frequency. The bistatic axis is the midaxis between the receiver and the transmitter axis. Knowing the relative orientation of the three bistatic axes for the three receivers allows calculation of the 3D water velocity. Because of the inference due to echoes from the boundaries (flume bed or water surface), the received signal might be disturbed, which may result in inaccurate velocity measurement. In this study, a few points near the bed were found to be influenced in this way. The velocity measurement by the ADV probe was not possible in the zone, which was 5cm below the free surface. The ADV readings were taken along several vertical lines at different section along the flume.

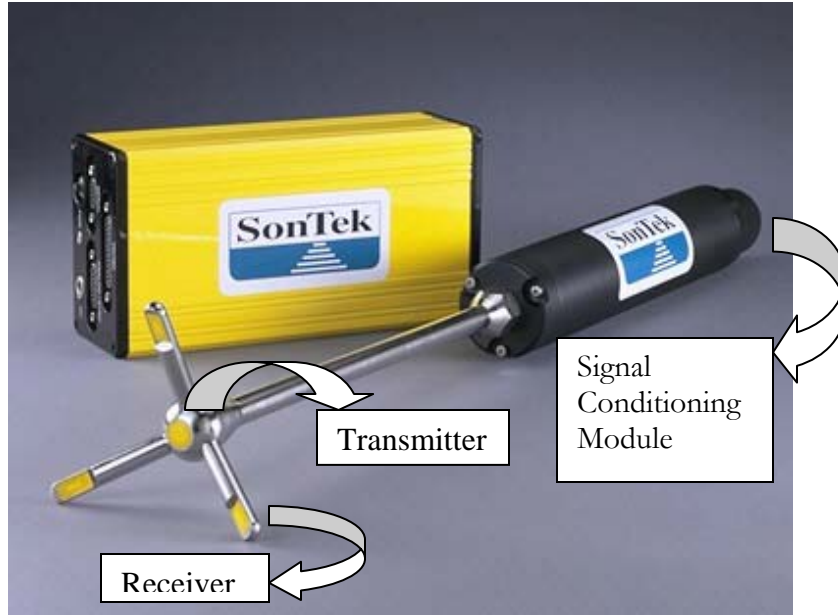


Fig 3.2 Different components of Acoustic Doppler Velocimeter

After taking all data from ADV, it was processed with the help of the software WinADV. WinADV provides an integrated environment for viewing and processing data collected using Acoustic Doppler Velocimeter. Data processing is the second major task handled by WinADV. Summary statistics files and raw data files can be produced that may be easily imported into spreadsheets. Raw data files combine both velocity and signal quality/signal strength data in one convenient file format. WinADV provides the capability to filter data on-the-fly and quickly view graphs of the filtered data. About 1500 samples of data were taken for each point at different section.

The time development of scour represents a very complicated flow phenomenon involving the movement of sediment-water mixture along the bed of the scour hole. Because of the continuously changing flow boundary as scour progress with time, the velocity distribution pattern in the scour hole would likewise be different at different stages of the erosion process. The bed shear stress is a function of the local bed velocity and the friction factor, which is often assumed to be constant, therefore, measurements of the bed velocity and distributions in a scour hole will enable the scouring process to be examined. Based on the measured floor velocity, a boundary shear stress was calculated as given below:

$$\tau_b = \frac{\rho f u_b^2}{8} \quad \dots\dots\dots(3.1)$$

Where  $\tau_b$  = shear stress near the bed  $\rho$  = fluid density;  $u_b$  = velocity at 0.4 cm from the bed and  $f$  = friction factor obtained using the Colebrook-White equation:

$$\frac{1}{f^{1/2}} = -2 \log_{10} \left( \frac{k_s}{14.83 H_T} + \frac{2.52}{f^{1/2} R_H} \right) \quad \dots\dots\dots (3.2)$$

Where  $k_s$  is the height of sand roughness; and  $H_T$  = local water depth and  $R_H = u_b H_T / \nu$ .  $\nu$  is the kinematic viscosity of the fluid. The effective roughness height of a movable plane bed surface may be about  $2d_{50}$ . In this case  $K_s = 2d_{50}$ .  $K_s$  value were reported by Kamphuis as  $K_s = 5.1d_{84}$  and Gladki as  $K_s = 2d_{80}$ . Both the measured particle velocity are best represented for  $K_s/d_{50} = 2$  to  $3$ .

The intensity of turbulence in a flow is described by the relative magnitude of the root mean square value of the fluctuating component with respect to the time mean velocity. It is defined as

$$T_u = \sqrt{\frac{1}{3} (\overline{u'^2} + \overline{v'^2} + \overline{w'^2})} / U_\infty \quad \dots\dots\dots (3.3)$$

Where  $u'$  = fluctuation of velocity in x-direction

$v'$  = fluctuation of velocity in y-direction

$w'$  = fluctuation of velocity in z-direction

### 3.4 Analysis of maximum scour depth and position of maximum scour

In order to formulate relationships for the maximum scour depth ( $d_s$ ) and its location measured downstream from the end sill ( $X_s$ ), all the affecting parameters (Table 3.2) were non-dimensionalized by  $h_p$ , the difference between upstream and downstream water levels.

These and the Froude number ( $Fr$ ) are grouped as below,

$$\left( Fr, \frac{H_u}{h_e}, \frac{H_d}{h_e}, \frac{G}{h_e}, \frac{d_{50}}{h_e} \right) \dots (3.4)$$

Since different Froude numbers may be employed depending upon the chosen flow section four definitions were considered for the study, as indicated in Table 3. Of these, the densimetric Froude number ( $Fr_{din}$ ) is as proposed by Liriano et.al (2002) and defined as

$$Fr_{din} = U / \sqrt{gd_{50}(\rho_s - 1)} \dots (3.5)$$

Where  $\rho_s$  is relative density of sand and  $d_{50}$  is the median diameter of sediment and  $U$  is average velocity at the section.

The methods of Non-linear Multiple Regression Analysis and the Back-Propagation Artificial Neural Network (ANN) techniques were used to relate the independent variables of the dimensionless group (1) and the modelled variables  $d_s$  and  $X_s$ , non-dimensionlized by  $h_p$ , the head difference between upstream and downstream. The SPSS (2000) software package is used for the regression analysis to obtain relational expressions using the Levenberg-Marquardt (LM) algorithm. This widely used optimization algorithm is an iterative technique that locates the minimum of a multivariate function expressed as the sum of squares of non-linear real-valued functions. The ANN analysis is carried out with the MATLAB (2003) software tool. This technique, though being used often nowadays in many engineering applications involving data processing (ASCE Task Committee, 2000), would be given a brief overview for the sake of completeness.

Fundamentally an ‘artificial neural network’ is a mathematical model that maps an n-dimensional real input ( $x_1, x_2, x_3, \dots, x_n$ ) to an m-dimensional output ( $y_1, y_2, y_3, \dots, y_m$ ) by modelling a function  $F: \mathbb{R}^n \rightarrow \mathbb{R}^m$  (Rojas, 1996). Here the basic computing unit, usually called a node, calculates the weighted sum of the inputs and compares it with a threshold (or



bias) and sends a signal to the output. The set of nodes that receive the input from the data set or those which deliver the predicted outputs are called the input and output layers, respectively. There may be other set of nodes, called the hidden layers, with no direct connection to the outside but are related to the input, output and other hidden layers. The ANN is trained, that is, the weights connecting the various nodes are adjusted through an iterative process starting from assumed values and working out till the overall error is reduced in the network below a tolerance level. Usually, the experimental or available data set is divided into two unequal sets and the network is trained with the larger and validated or tested with the smaller.

In the present work a single hidden layer, as is usual for this kind of data processing, is chosen. For training, the back-propagation algorithm is employed, the use of which is quite common due to its ease and simplicity. To expedite convergence, the Levenberg-Marquardt algorithm is used. This configuration is implemented for both modelling of maximum scour depth and its location from the end-sill. The use of ANN models in obtaining suitable relations between the flow variables and scour parameters, though relatively new, is gaining popularity. Azmatullah et al. (2005) have recently applied this technique for modelling of flow and scour variables below dams.

### ***Maximum scour depth***

The regression model employed to derive a relation between the nondimensionalized scour depth to the nondimensionalized flow variables uses 250 data sets randomly chosen from the observed 310. Thus around 80 percent of the observed data, belonging to all the four cases, are used for calibration. Of the four Froude numbers (Table 3),  $Fr_{din}$  was found to

yield a relation with the best correlation coefficient (R) compared to the equations modelled with the other three. The relation that is obtained is as follows:

$$\hat{d}_s = 2.98(Fr_{din})^{3.15}(\hat{H}_u)^{-1.25}(\hat{H}_d)^{-1.50}(\hat{G})^{2.51}(\hat{d}_{50})^{1.05} \quad \dots(3.6)$$

Where  $\hat{d}_s$ ,  $\hat{H}_u$ ,  $\hat{H}_d$ ,  $\hat{G}$  and  $\hat{d}_{50}$  are the non-dimensional values of scour depth, upstream and downstream water levels measured above the downstream apron elevation, flow aperture at gate section and particle size respectively.

The ANN model developed to predict the maximum scour depth considers the same parameters as for the regression analysis. Thus the input layer of five nodes receives the four non-dimensionalised independent variables and the Froude number  $Fr_{din}$ . The output layer, comprising of a single node, predicts the non-dimensional scour depth. A single hidden layer with 20 nodes was finally adopted after trials that searched for the minimum root mean square error. The maximum number of epochs for training the network was taken as 500. The input and output parameters were normalized to the scale of -1 to +1 as is required for a ANN model. In the regression analysis, 250 data sets were randomly chosen to train the ANN. The remaining 60 data sets were used for testing the network. Both the training and testing data sets comprised of data covering all the four flow conditions. A comparison of the predicted normalized scour depths by the regression and the ANN approaches is presented in Fig. 4, which uses only the 60 data sets that are used for testing. As may be observed the ANN model appears to fare rather well in comparison with the regression model. Interestingly, the cluster of points with the lower values of normalized scour depths belong to the controlled flow region and those with higher values to the uncontrolled region.

### ***Position of maximum scour***

Similar to modelling maximum depth of scour, both regression and ANN techniques are implemented for modelling the location of the point of maximum scour measured from the edge of the downstream apron. The independent parameters considered are also the same. The generalized regression equation, obtained by fitting 250 of the 310 data sets, is found to be as follows:

$$\hat{X}_s = 12.20 (Fr_{din})^{2.07} (\hat{H}_u)^{-1.69} (\hat{H}_d)^{0.2} (\hat{G})^{1.46} (\hat{d}_{50})^{0.75} \quad \dots(3.7)$$

Where  $\hat{X}_s$  is the distance, measured from the edge of the apron normalized with the head difference  $h_e$  between the upstream and downstream water levels. The independent parameters carry the same meaning as for the analysis of scour depth.

The ANN model for this analysis comprises of five input and one output nodes. There is a single hidden layer containing 25 nodes, the configuration being chosen to ensure the least root mean square error. The network is trained with 250 data sets and tested with the remaining 60. Comparison of the predictions made by the regression and ANN models is illustrated in Fig. 5. The regression model appears to be fitting better in this case, with the correlation coefficient ( $R = 0.9964$ ) being slightly better than that of the ANN analysis. In order to evaluate the relative predictive capabilities of the regression and ANN models, the models are compared through four performance parameters. The performance parameters are the Correlation Coefficient ( $R$ ), Average Error ( $AE$ ), Average Absolute Deviation ( $d$ ) and Root Mean Square Error ( $RMSE$ ) and are as described by Azmatullah et al.<sup>29</sup> The ANN model apparently performs better by the standard of  $R$ ,  $AE$  and  $d$  but trails behind the regression model on  $RMSE$ .

### 3.5 Similarities in the profile of scour holes

From the experiments conducted, it is observed that the shape of the scoured hole formed in the sand bed downstream of the solid apron of a barrage differs according to the prevailing hydraulic condition. The elevation of the scoured profile on the upstream (at the edge of the solid apron) varies between the crest levels of the end sill to some depth below depending upon the flow condition. The general shape of the scour holes for all the cases show a concave upward shape which inflexes back to a convex upward profile in the shape of hump as shown in Fig. 3.3 to Fig. 3.6 by plotting non-dimensional scour depth against non-dimensional distance for the four different hydraulic conditions. Though not shown in the Figures, the profiles change back asymptotically to the original horizontal level further downstream. The convex upward hump is seen to be most pronounced for the case of controlled submerged flow and least for the uncontrolled free flow conditions.

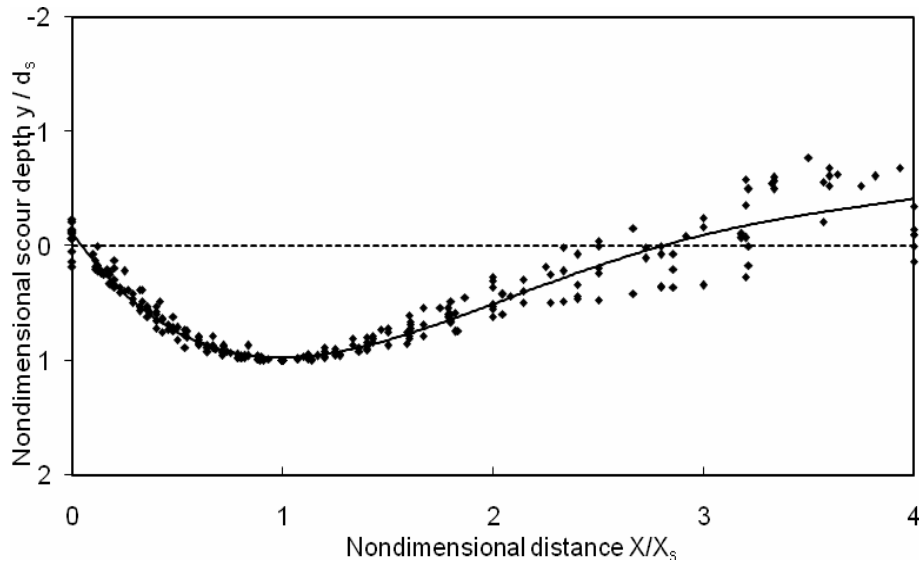


Figure 3.3 Dimensionless equilibrium scour profile for controlled free flow (CF) condition

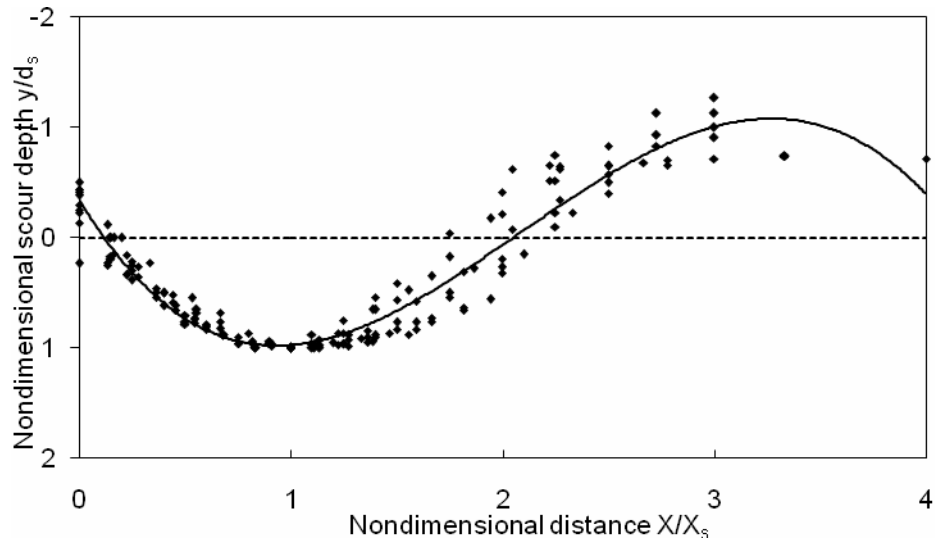


Figure 3.4 Dimensionless equilibrium scour profile for controlled submerged flow (CS) condition

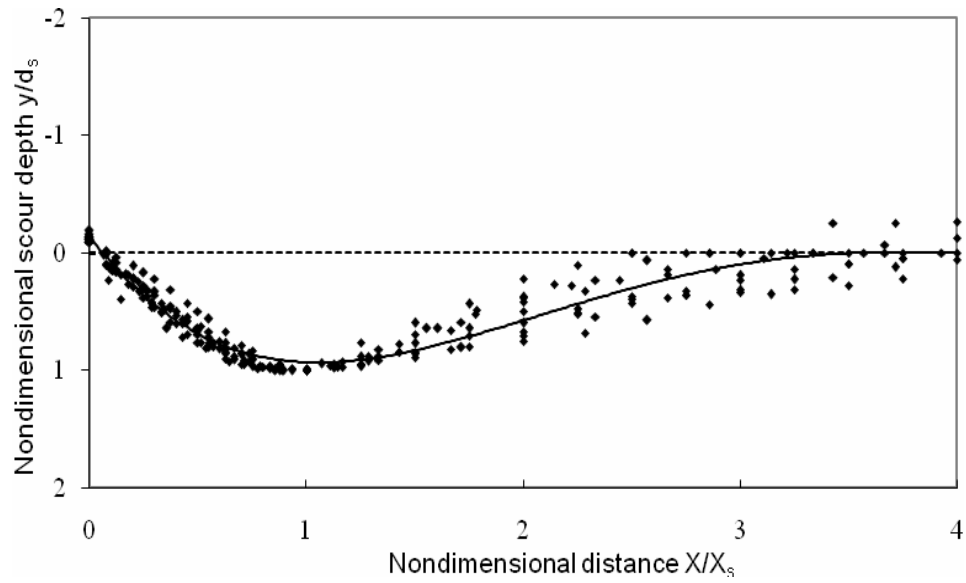


Figure 3.5 Dimensionless equilibrium scour profile for uncontrolled free flow (UCF) condition

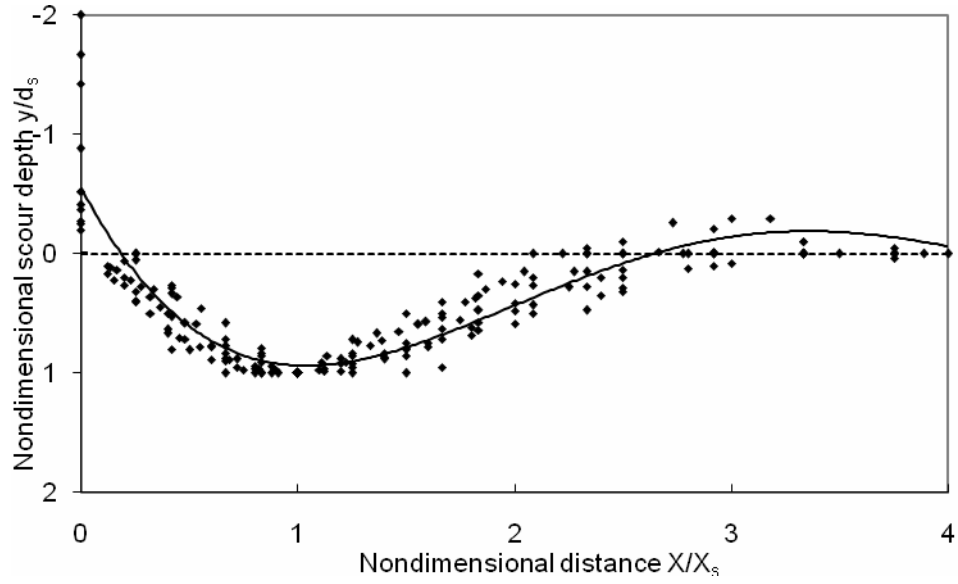


Figure 3.6 Dimensionless equilibrium scour profile for uncontrolled submerged flow (UCS) condition

The similarity of the scour profiles for the different cases prompted the development of an ANN model that can predict the profiles of the scoured bed depending on the various hydraulic parameters. The input variables are the same as those used for modelling of maximum scour depth and modelling of position of maximum scour are the hydraulic variables. The output neurons correspond to the scour depths at certain specified locations, normalized with the maximum scour depth in each case. Eleven sections have been chosen here, which are located at 0 cm, 3 cm, 5 cm, 8 cm, 10 cm, 15 cm, 20 cm, 25 cm, 30 cm, 40 cm, and 50 cm respectively downstream of the edge of the solid apron.

### 3.5.2 ANN application for modelling the profile of scour hole

A neural network model is developed for predicting the scouring pattern downstream of a barrage solid apron. Here the input parameters are the same as for previous cases and are non-dimensionalized by dividing with  $h_c$ . Unlike the previous two cases the configuration of the model here is a little different here. Here following the same procedure i.e., the hit and trial procedure, the best possible configuration is achieved. It has been observed that while considering all the sections observed experimentally for the model study, the ANN model tried didn't predict well. It is seen that for the end sections the ANN model is not working well. This may be due to the variations in the scour profile. For most of the cases like for uncontrolled and submerged cases, it is zero scour at the end sections. For free and controlled condition there is some scouring though small, but also for some cases it is significant and sometimes the scour hole extends beyond the erodible bed studied for the model. These variations in scouring lead to inefficient modelling of the neural network. Hence, only eleven sections out of twenty-seven sections are considered for predicting the scour profile. These eleven sections are at 3 cm, 5 cm, 8 cm, 10 cm, 15 cm, 20 cm, 25 cm, 30 cm, 35 cm, 40 cm and 50 cm distances from the end sill considering the scour hole portion only as the maximum  $d_s$  occurs in this region. The scour depths at these sections are the outputs of the ANN model which are non-dimensionalized by the maximum scour depth at those sections. Similarly as in the previous cases, all the input and output parameters were normalized between -1 to 1 for the sake of using the tansig transfer function. Here, the output layer has thus eleven neurons and input layer has five neurons. For this complexity out of different training functions trainlm and trainscg (Scaled Conjugate Gradient) functions were found suitable. Though trainlm function converges fast in achieving the learning rate, it becomes very slow for complex models. The trainscg function is not as fast converging as trainlm but it performs better when it comes to the time required for a desired training. Testing both the function several times finally trainlm function is found to be suitable for better testing. Here also, eighty percent dataset have been used for training and the rest is used for testing the model. The specifications of the model adopted for predicting the scour profile is presented below:

Number of input neurons	: 5
Number of hidden layers	: 1
Number of neurons in hidden layer	: 45
Number of output neuron	: 11
Number of epochs for training	: 1500
Training function	: trainlm
Transfer function	: tansig
Performance Function	: MSE (Mean Square Error)
Value of MSE to be achieved in training	: 0.001

The goal achieved in the successful training was 0.002. The performance of the training can be seen from Figures (3.7) to (3.17) which show the comparison of output from the trained model and the target given to the model for training.

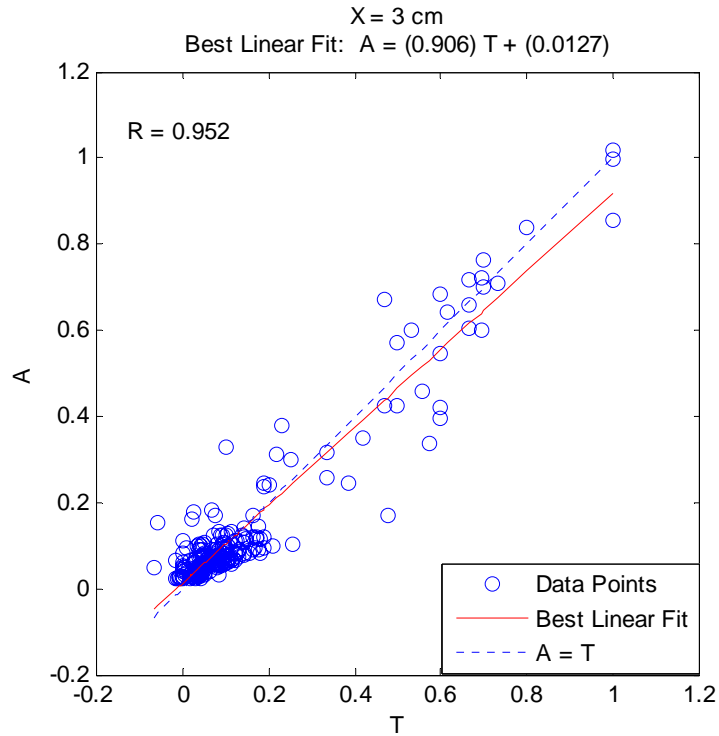


**Fig. 3.7 Comparison of Training Output and the Measured Relative Scour Depth for Combined Flow Conditions at X = 3 cm from End Sill**



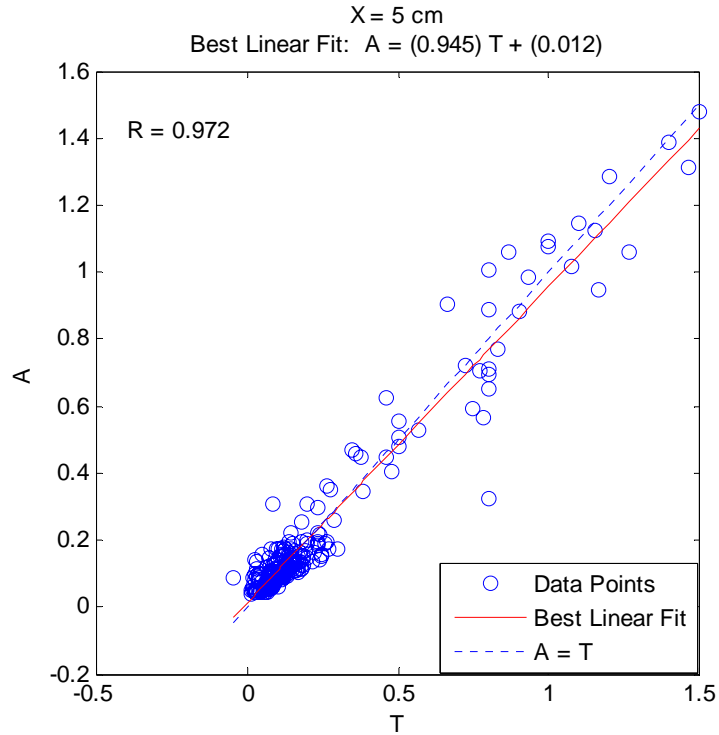


**Fig. 3.8 Comparison of Training Output and the Measured Relative Scour Depth for Combined Flow Conditions at X = 5 cm from End Sill**

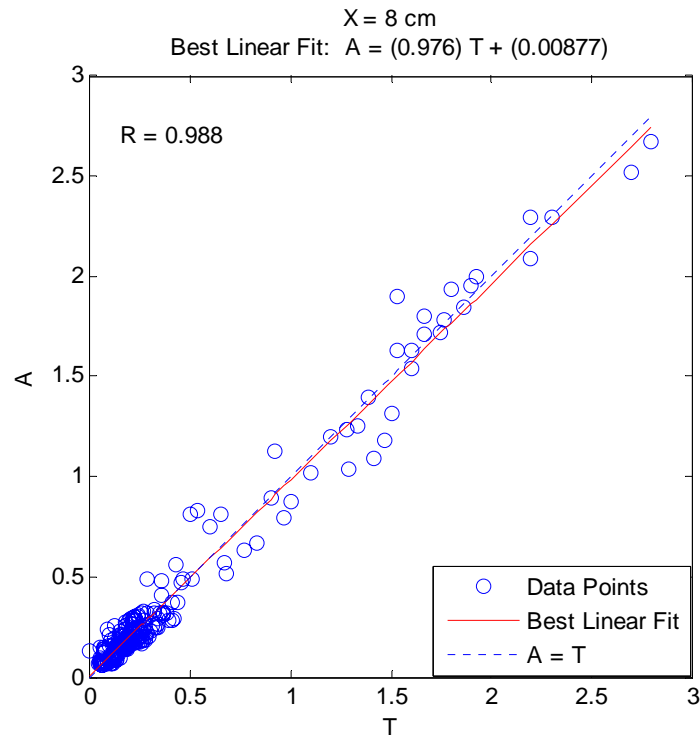


**Fig. 3.9 Comparison of Training Output and the Measured Relative Scour Depth for Combined Flow Conditions at X = 8 cm from End Sill**

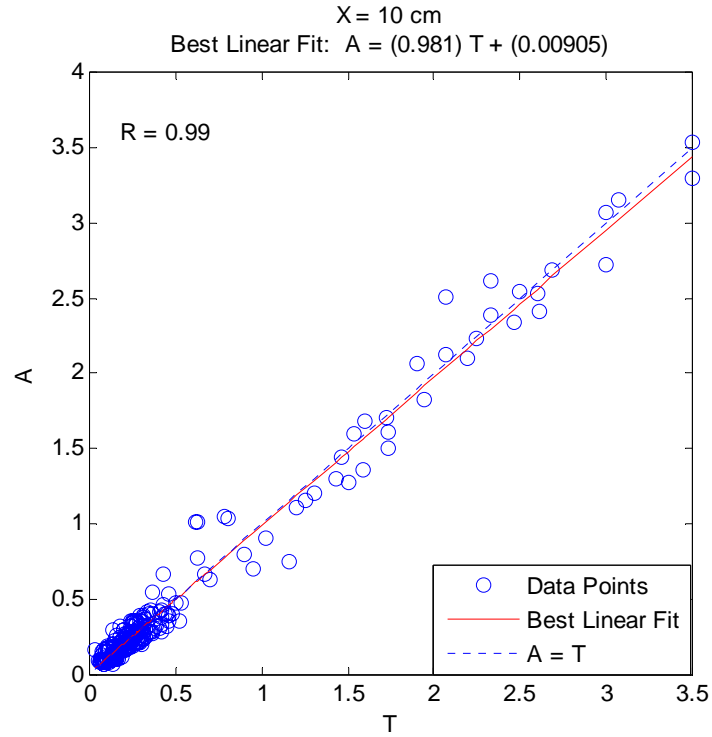


**Fig. 3.10 Comparison of Training Output and the Measured Relative Scour Depth for Combined Flow Conditions at X = 10 cm from End Sill**

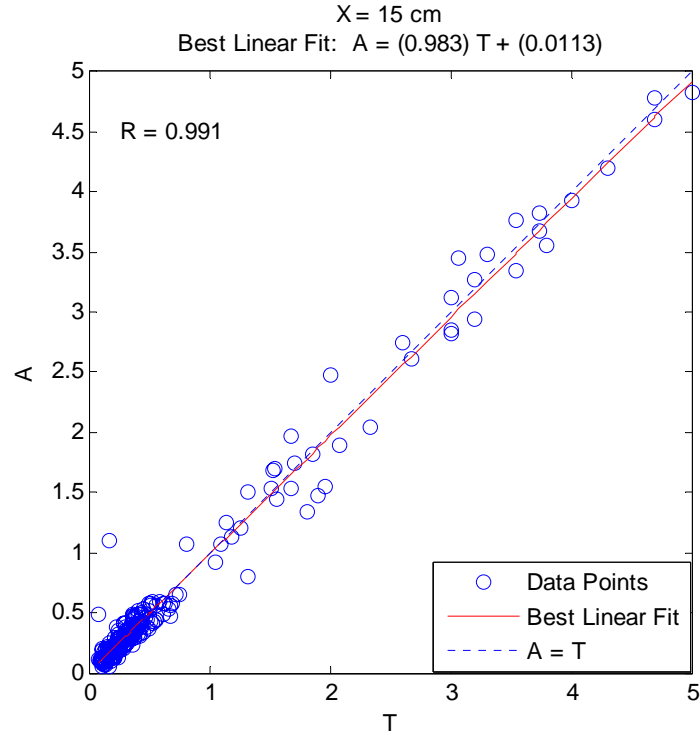


**Fig. 3.11 Comparison of Training Output and the Measured Relative Scour Depth for Combined Flow Conditions at X = 15 cm from End Sill**

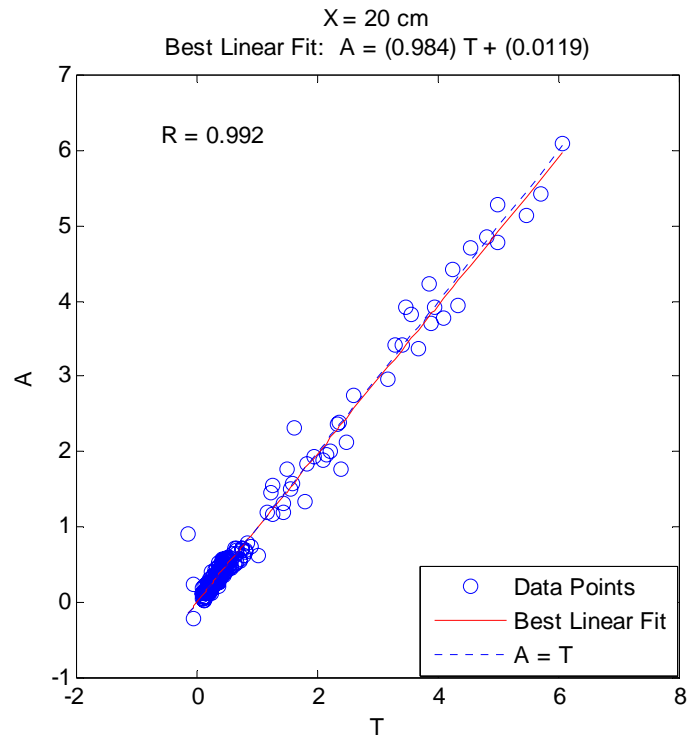


**Fig. 3.12 Comparison of Training Output and the Measured Relative Scour Depth for Combined Flow Conditions at X = 20 cm from End Sill**

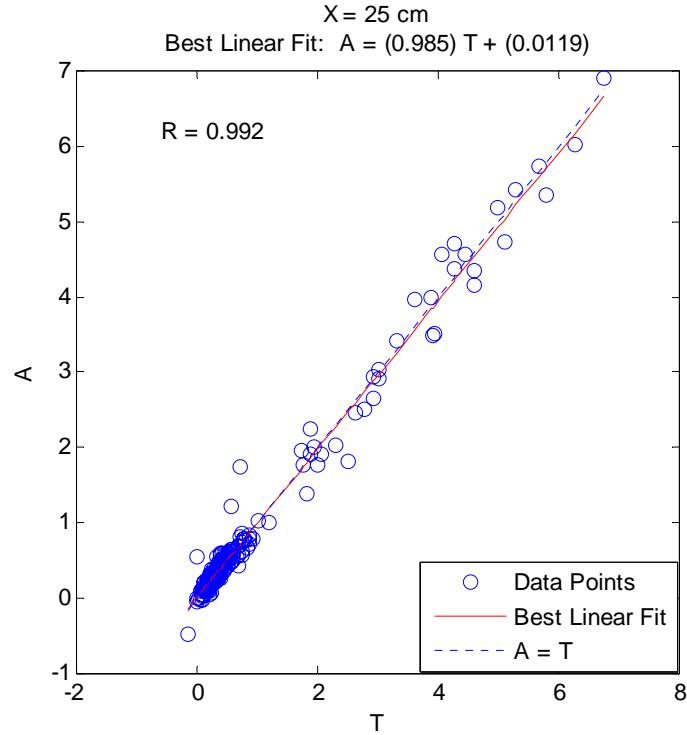


**Fig. 3.13 Comparison of Training Output and the Measured Relative Scour Depth for Combined Flow Conditions at X = 25 cm from End Sill**

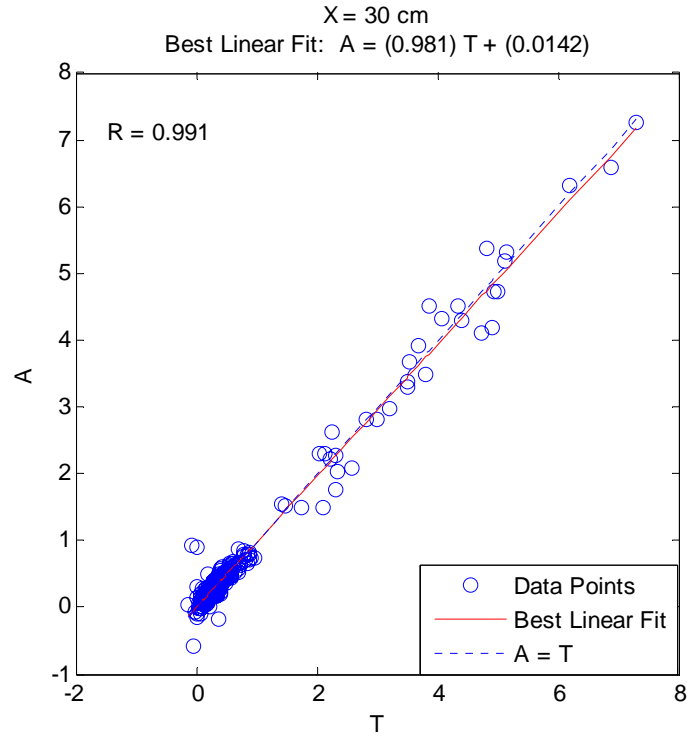


**Fig. 3.14 Comparison of Training Output and the Measured Relative Scour Depth for Combined Flow Conditions at X = 30 cm from End Sill**

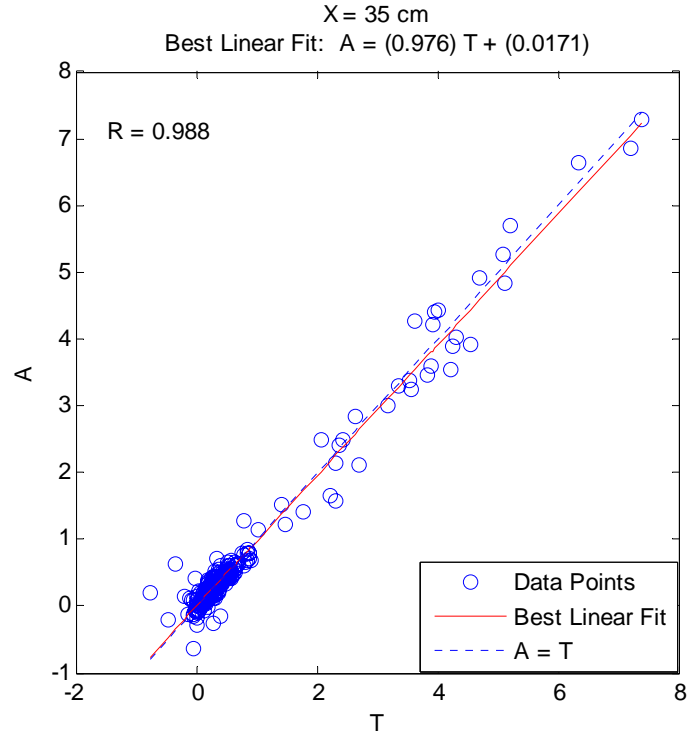


**Fig. 3.15 Comparison of Training Output and the Measured Relative Scour Depth for Combined Flow Conditions at X = 35 cm from End Sill**

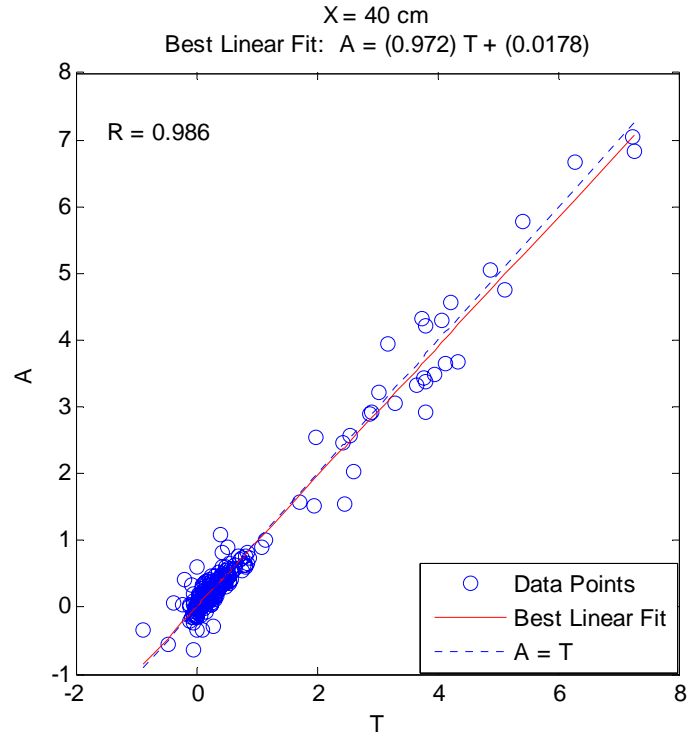


**Fig. 3.16 Comparison of Training Output and the Measured Relative Scour Depth for Combined Flow Conditions at X = 40 cm from End Sill**

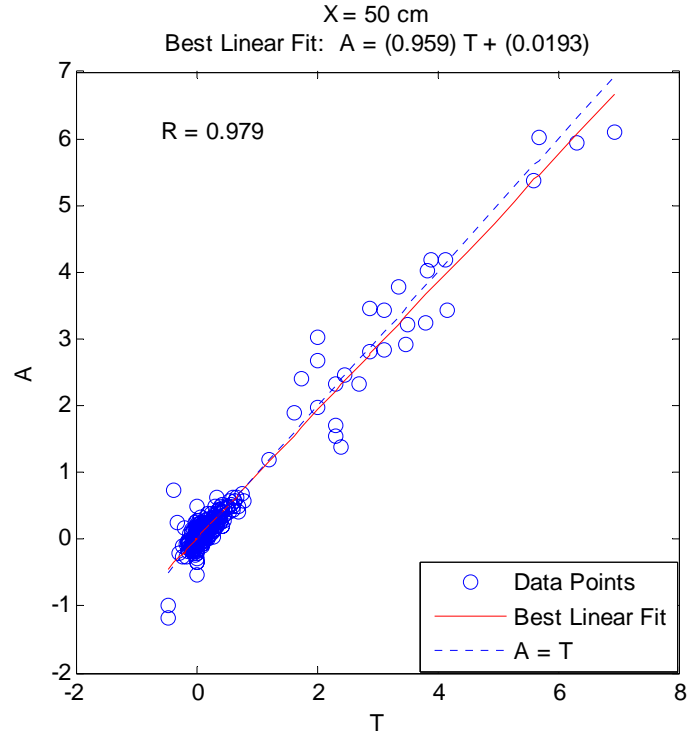


**Fig. 3.17 Comparison of Training Output and the Measured Relative Scour Depth for Combined Flow Conditions at X = 50 cm from End Sill**

From the preceding figures it is seen that the ANN model has well trained with correlation coefficients are as high as 0.952, 0.972, 0.988, 0.99, 0.991, 0.992, 0.992, 0.991, 0.988, 0.986, 0.979 respectively with a MSE of 0.002. It is observed that at the sections, at the beginning and at the end of scour hole considered the training is a little less accurate than the middle sections. This may be due to the fact that, at these end sections the scour depth variations are more compared to the middle sections, or more precisely for most of the submerged and uncontrolled flow conditions the scour depth is zero at these sections while at the middle sections the scour depth value are almost comparable for all the dataset. This is the same result which was described earlier in selecting only eleven sections for the modelling. As the performance of the trained model is quite satisfactory, this model is adopted for testing the rest of the dataset. This well trained model is tested with the twenty percent dataset and the comparison of experimental and the tested output of the model are shown in Figures (3.18) to (3.28).

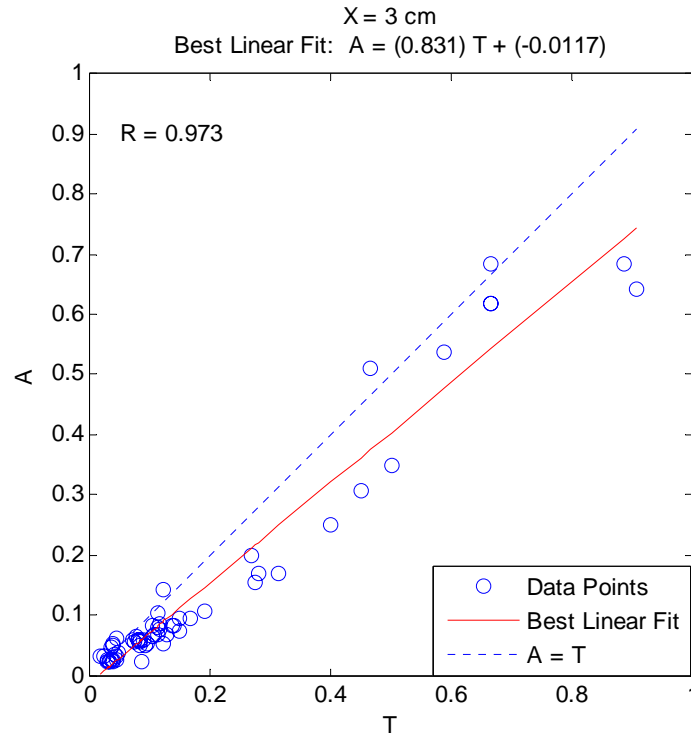


**Fig. 3.18 Comparison of Testing Output and the Measured Relative Scour Depth for Combined Flow Conditions at X = 3 cm from End Sill**

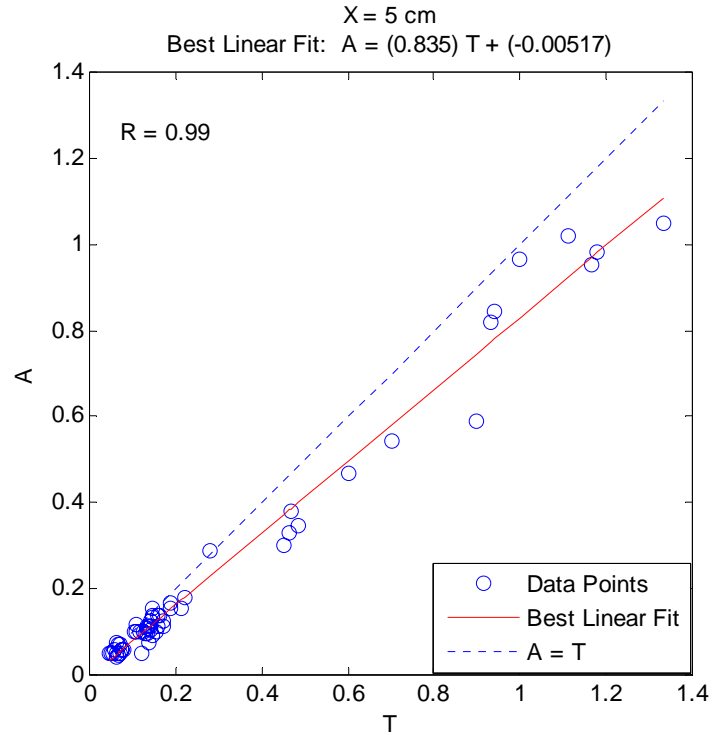


**Fig. 3.19 Comparison of Testing Output and the Measured Relative Scour Depth for Combined Flow Conditions at X = 5 cm from End Sill**

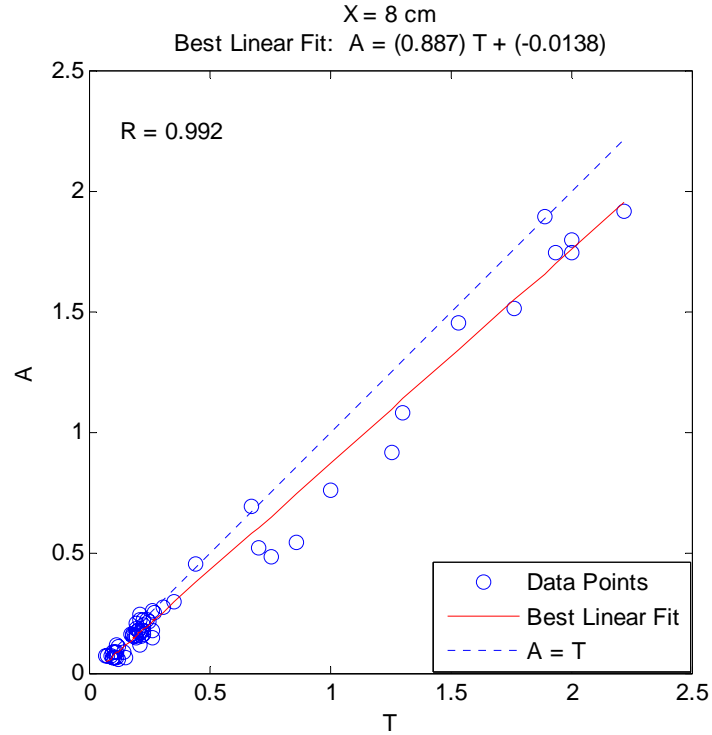


**Fig. 3.20 Comparison of Testing Output and the Measured Relative Scour Depth for Combined Flow Conditions at X = 8 cm from End Sill**

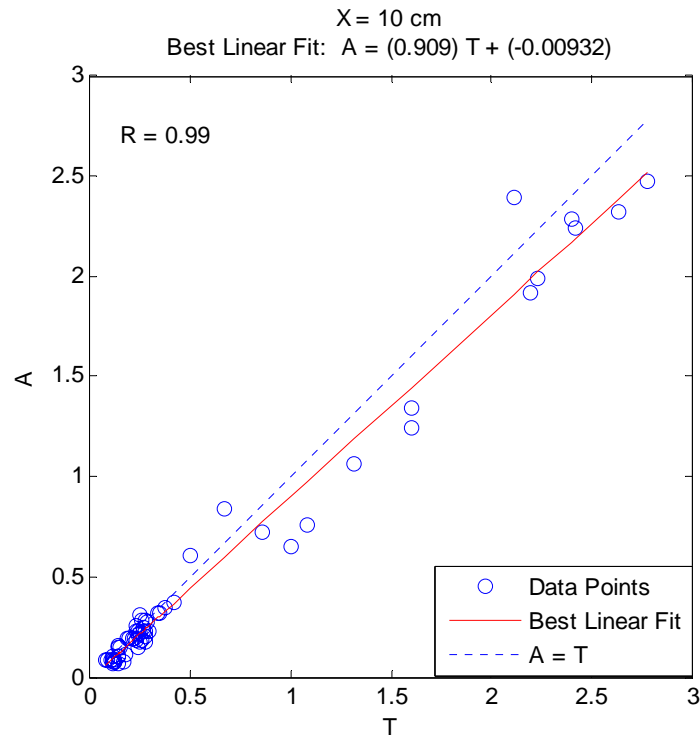


**Fig. 3.21 Comparison of Testing Output and the Measured Relative Scour Depth for Combined Flow Conditions at X = 10 cm from End Sill**

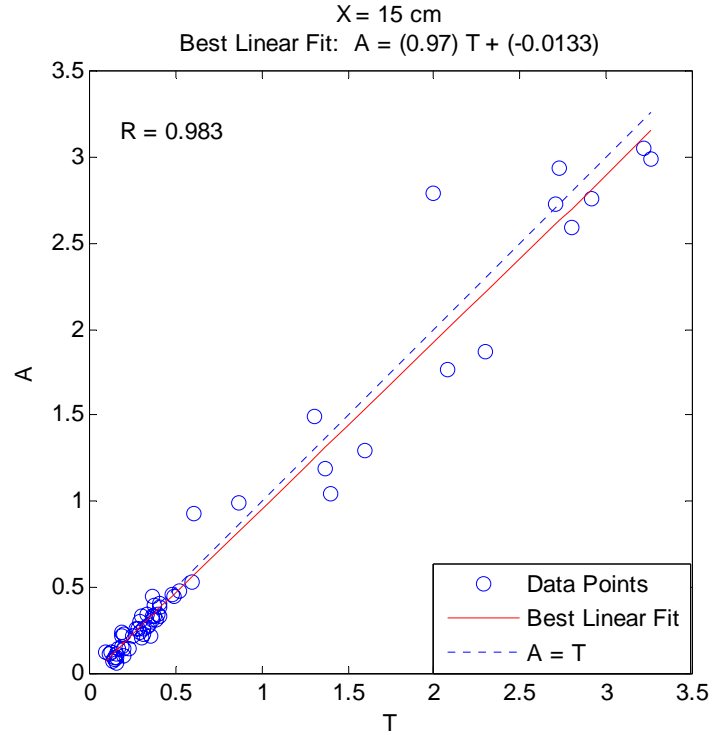


**Fig. 3.22 Comparison of Testing Output and the Measured Relative Scour Depth for Combined Flow Conditions at X = 15 cm from End Sill**



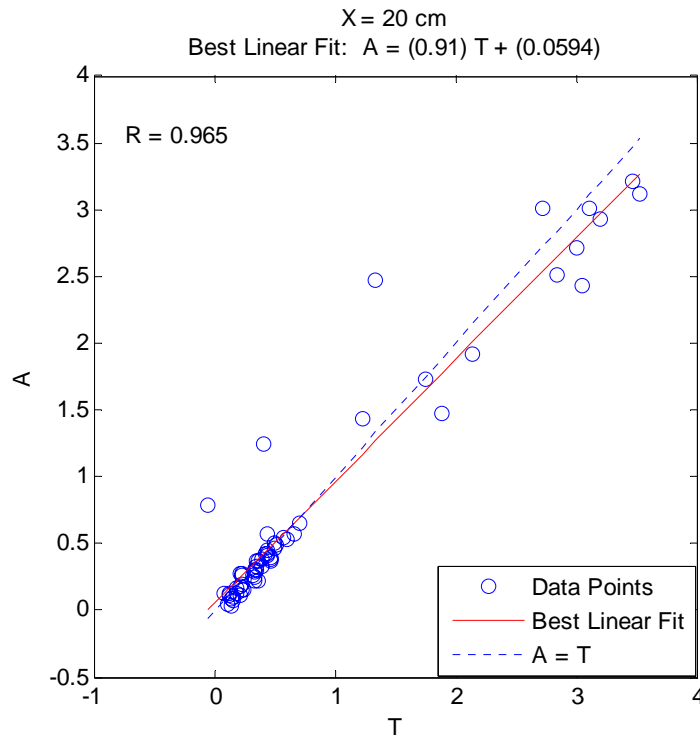


**Fig. 3.23 Comparison of Testing Output and the Measured Relative Scour Depth for Combined Flow Conditions at X = 20 cm from End Sill**

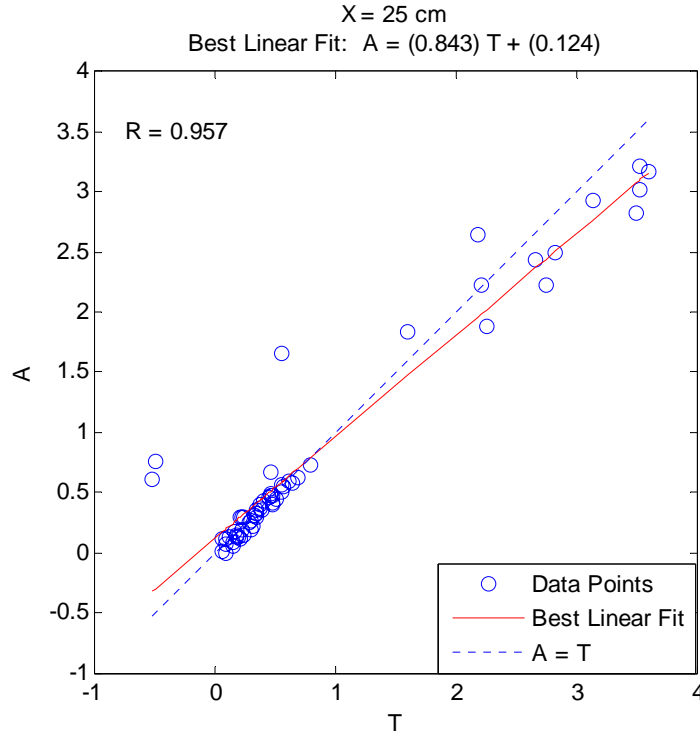


**Fig. 3.24 Comparison of Testing Output and the Measured Relative Scour Depth for Combined Flow Conditions at X = 25 cm from End Sill**

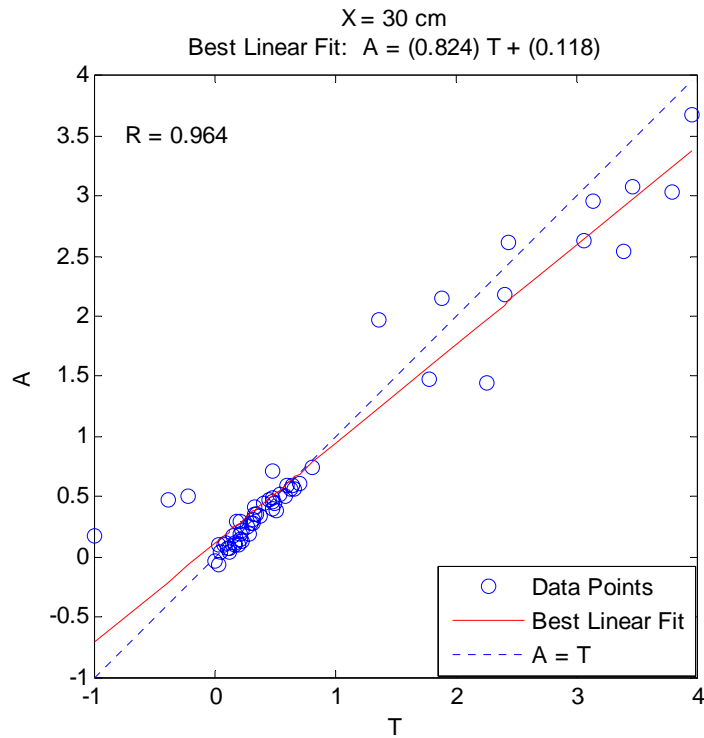


**Fig. 3.25 Comparison of Testing Output and the Measured Relative Scour Depth for Combined Flow Conditions at X = 30 cm from End Sill**

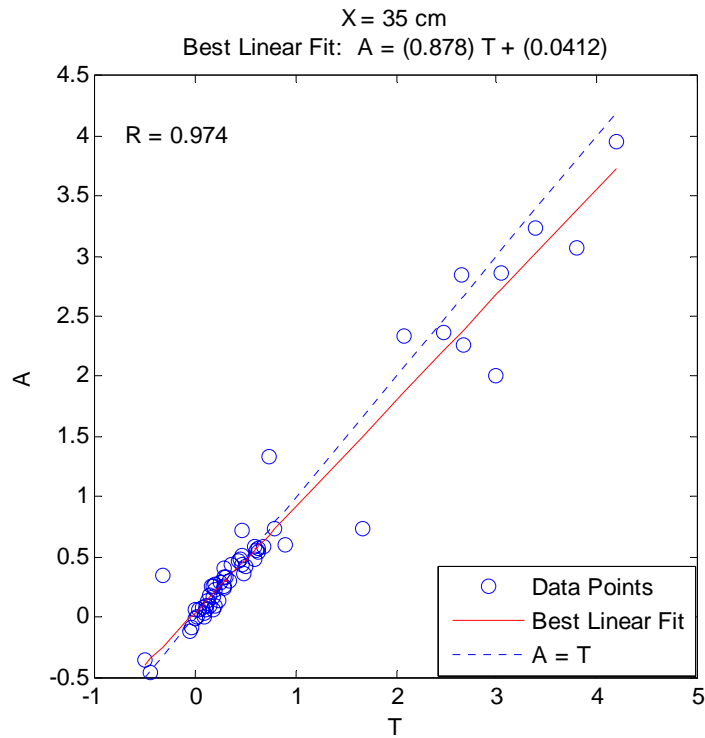


**Fig. 3.26 Comparison of Testing Output and the Measured Relative Scour Depth for Combined Flow Conditions at X = 35 cm from End Sill**

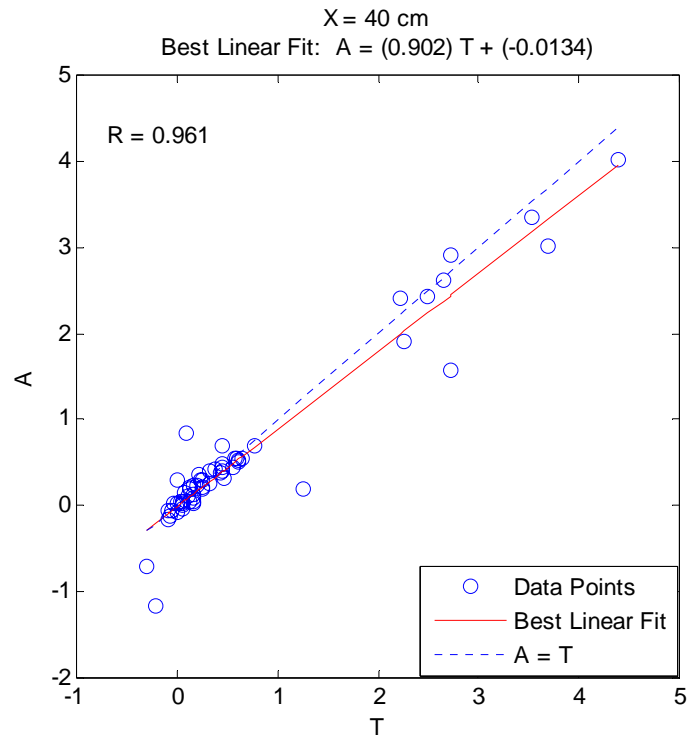


**Fig. 3.27 Comparison of Testing Output and the Measured Relative Scour Depth for Combined Flow Conditions at X = 40 cm from End Sill**

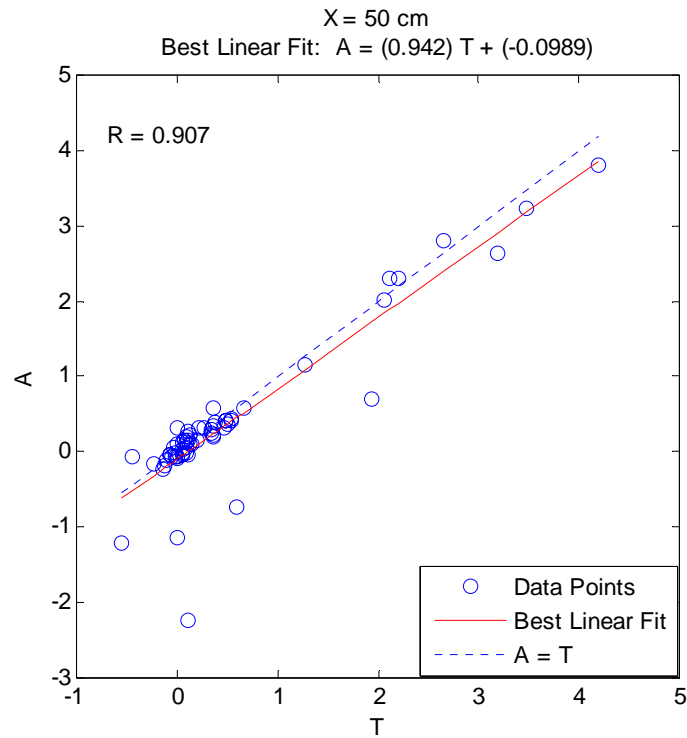


**Fig. 3.28 Comparison of Testing Output and the Measured Relative Scour Depth for Combined Flow Conditions at X = 50 cm from End Sill**

The correlation coefficients for the above testing datasets are 0.973, 0.99, 0.992, 0.99, 0.983, 0.965, 0.957, 0.964, 0.974, 0.961, and 0.907 respectively and with MSE of 0.004, which is really a sign of a better model for prediction although a little variation is there which can be expected from ANN modelling. The training dataset, which covers a wide range of possible flow situation, can be attributed to the successful testing of the model. It is also known as ANN performance significantly depends upon the range of dataset considered for training and testing. Its performance increases with the increase in the training dataset. Also it is important to have almost all the possible conditions or situations with a very wide range for the training dataset for a good ANN model though in some cases it becomes very difficult to collect such a wide range of data.

The outputs of tested ANN data are plotted against their corresponding experimental observations. Out of all tested dataset only eighth sample comparisons are shown in Figs. 3.29 to 3.36, two for the first four cases mentioned earlier. From these comparisons the accuracy in prediction of the model is clearly visible.

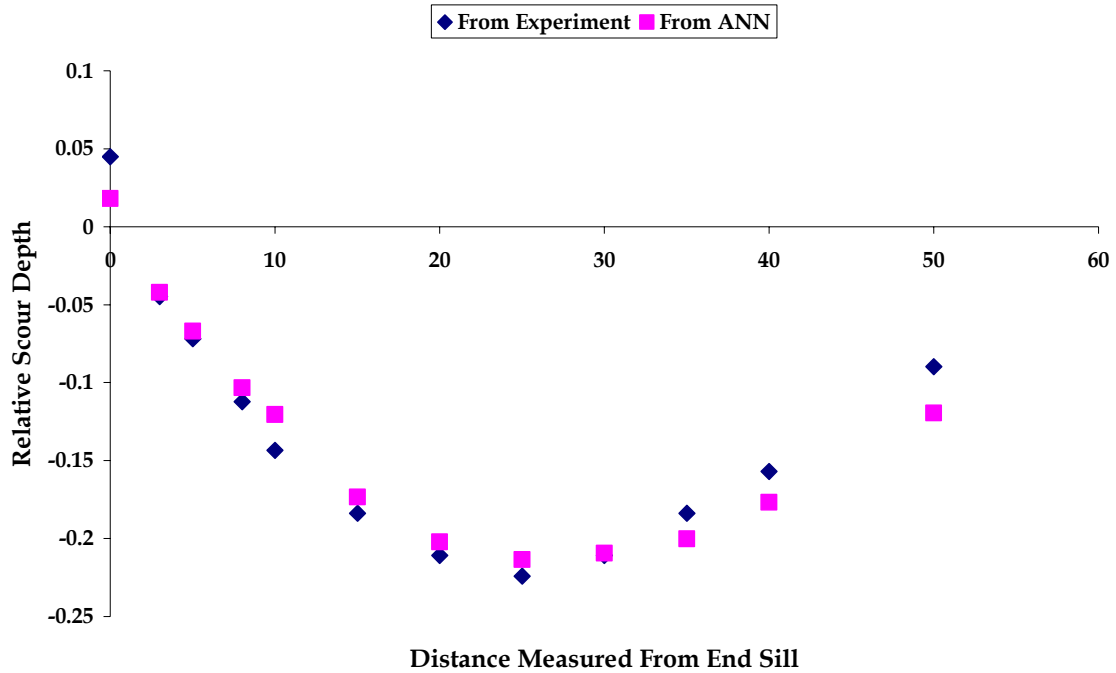


**Fig. 3.29 Comparison of Relative Scour Depth from Experiment and ANN:  
Controlled-Free Flow Test Set 1**

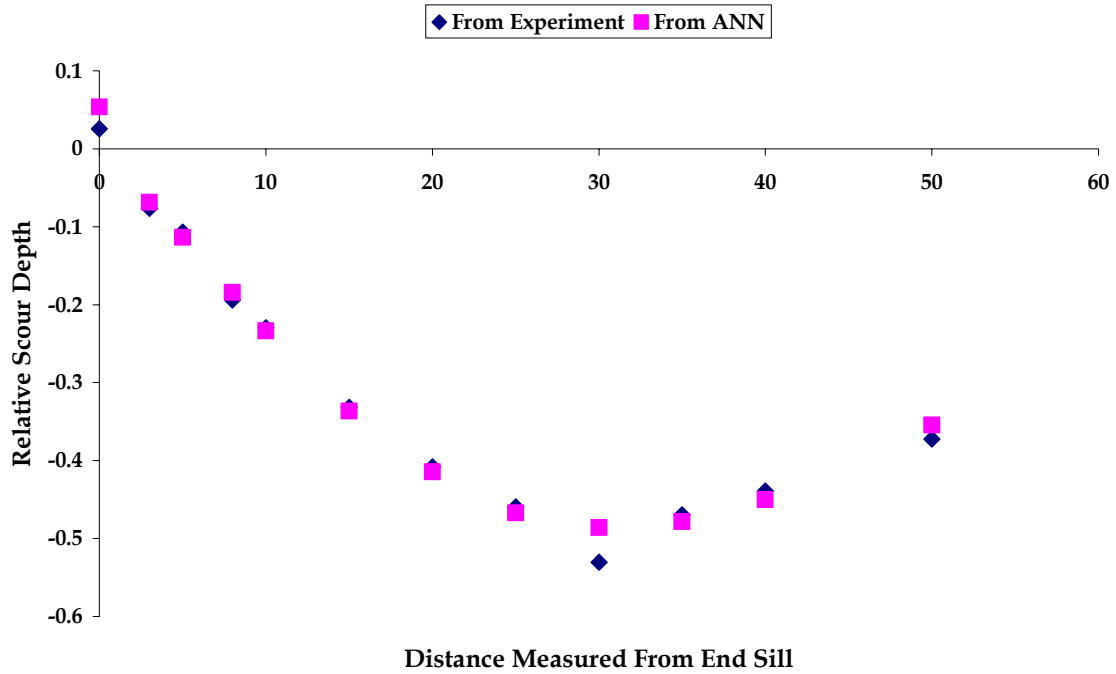


**Fig. 3.30 Comparison of Relative Scour Depth from Experiment and ANN:  
Controlled-Free Flow Test Set 2**

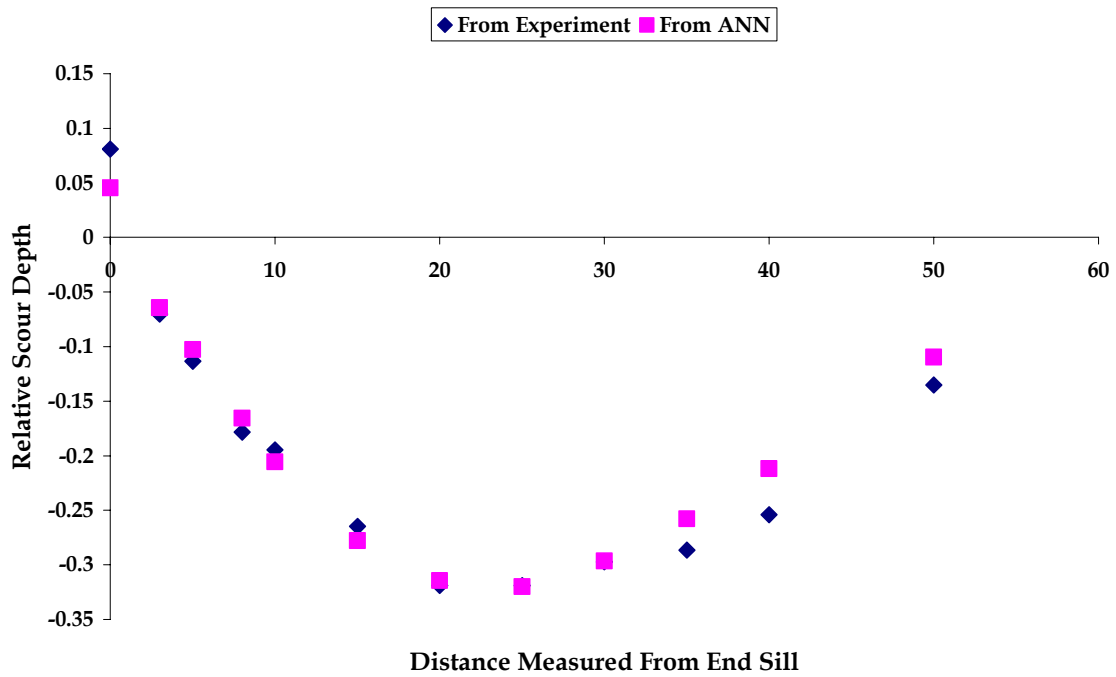


**Fig. 3.31 Comparison of Relative Scour Depth from Experiment and ANN:  
Controlled-Submerged Flow Test Set 1**

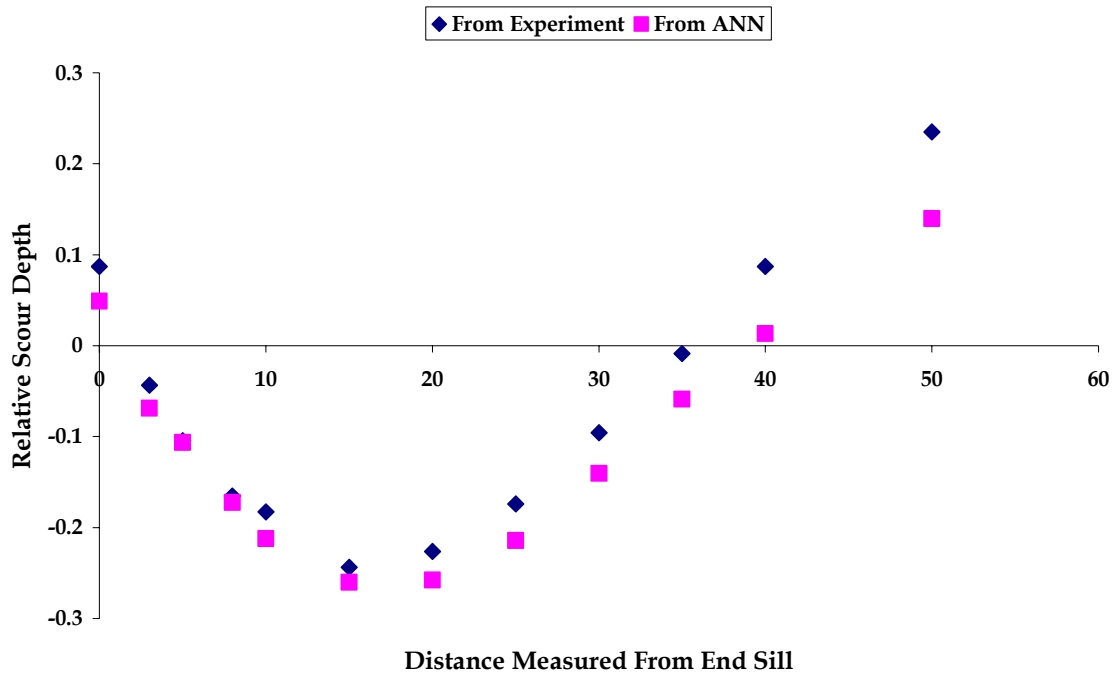


Fig. 3.32 Comparison of Relative Scour Depth from Experiment and ANN:  
Controlled-Submerged Flow Test Set 2

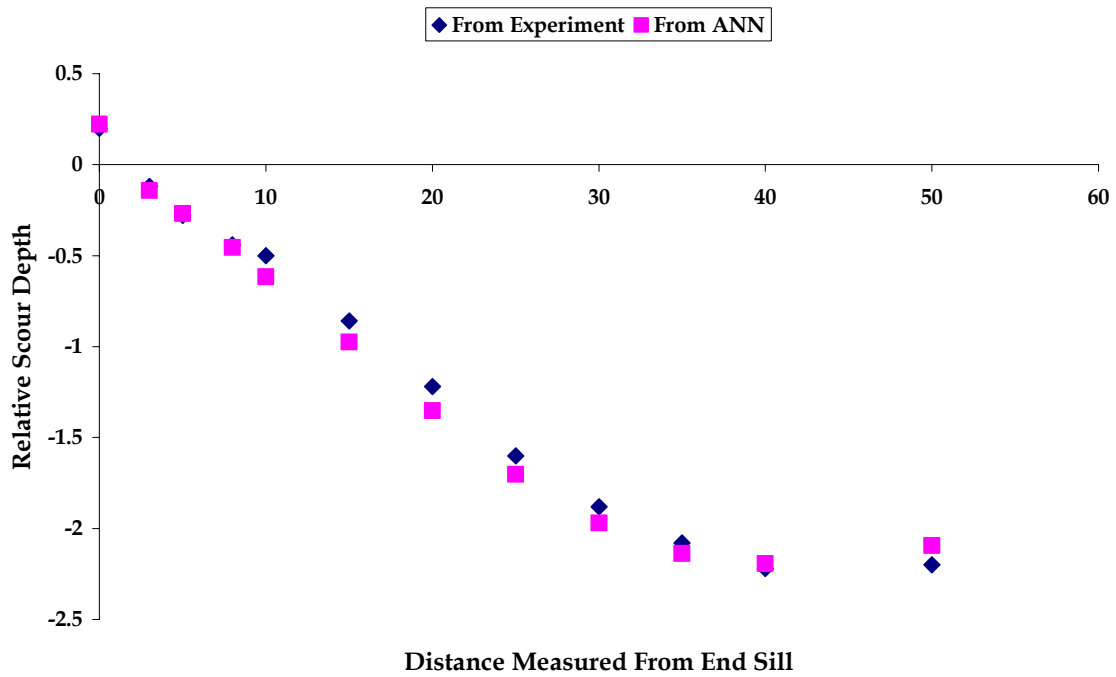


Fig. 3.33 Comparison of Relative Scour Depth from Experiment and ANN:  
Uncontrolled-Free Flow Test Set 1

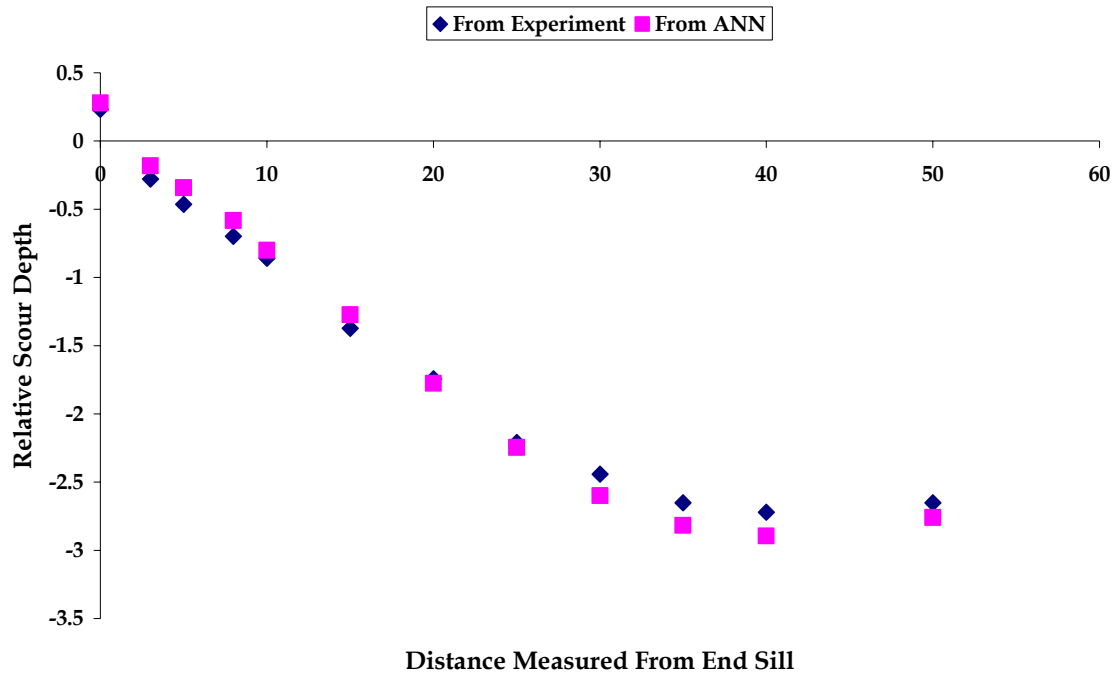


Fig. 3.34 Comparison of Relative Scour Depth from Experiment and ANN:  
Uncontrolled-Free Flow Test Set 2

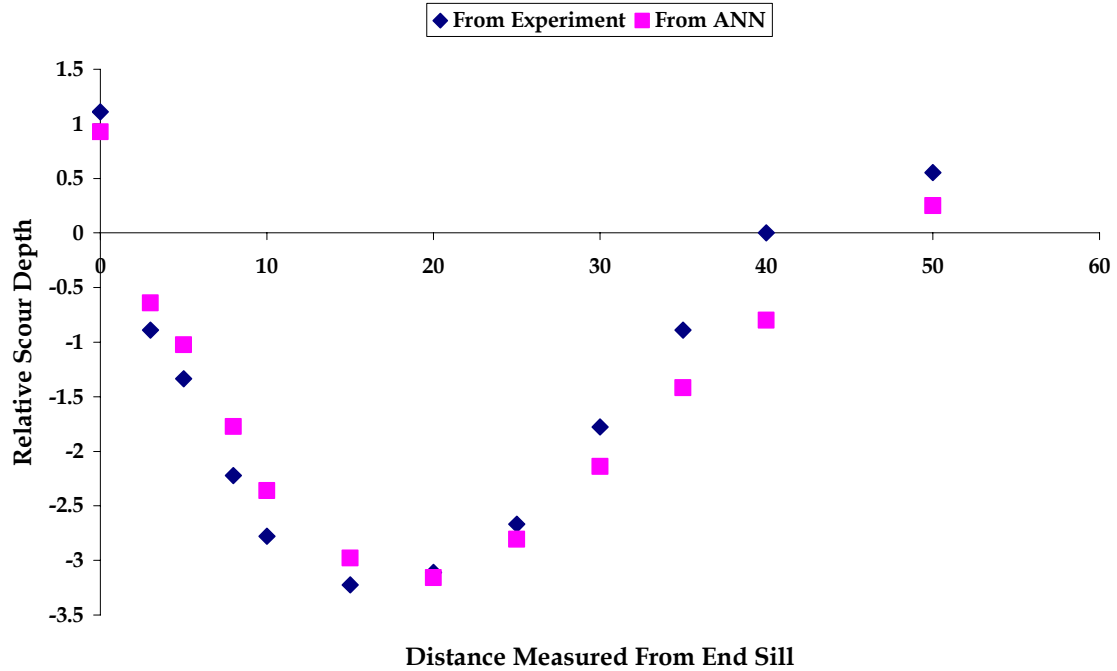
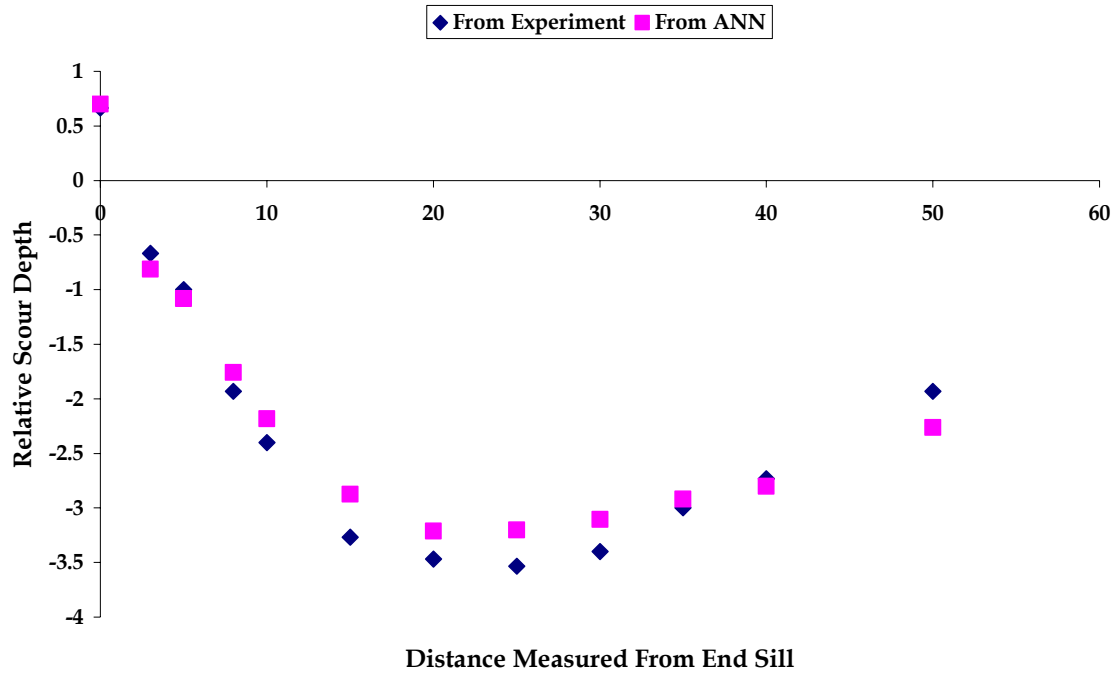


Fig. 3.35 Comparison of Relative Scour Depth from Experiment and ANN:  
Uncontrolled-Submerged Flow Test Set 1



**Fig. 3.36 Comparison of Relative Scour Depth from Experiment and ANN:  
Uncontrolled-Submerged Flow Test Set 2**

From Figures (3.29) to (3.36) it is seen that the results from the ANN model agree with those from experimental observations. But there are also some variations in exact matching of all the tested dataset. The following table shows the variations involved in the tested dataset in terms of percentage deviation from the maximum scour depth at the section.

**Table 3.3 Variations of Tested Dataset (60 cases) from the Maximum Scour Depth  
Observed from Experiments**

Sl. No.	Description of Variation	No. of Dataset	% of Dataset
1	With in 5% of Maximum Scour Depth at that Section	13	21.7
2	With in 10% of Maximum Scour Depth at that Section	24	40
3	With in 20% of Maximum Scour Depth at that Section	13	21.7
4	Beyond 20% of Maximum Scour Depth at that Section	10	16.6



### 3.6 Modelling of flow and scour by numerical simulation package

A numerical modelling study of the scoured bed was attempted using the commercially available software package FLUENT. One license of this package is available with Indian Institute of Technology, Kharagpur and an extensive study was carried out using the software.

#### 3.6.1 Numerical Modelling Setup

The CFD software FLUENT uses the standard k-epsilon viscous model with Eulerian Multiphase solver. The first step in simulating a flow condition using a numerical scheme is to setup a computational grid within a defined computational domain. A two and three dimensional non-uniform grid is used within refinement near wall region. GAMBIT is the program used to generate the grid or mesh for the CFD solver.

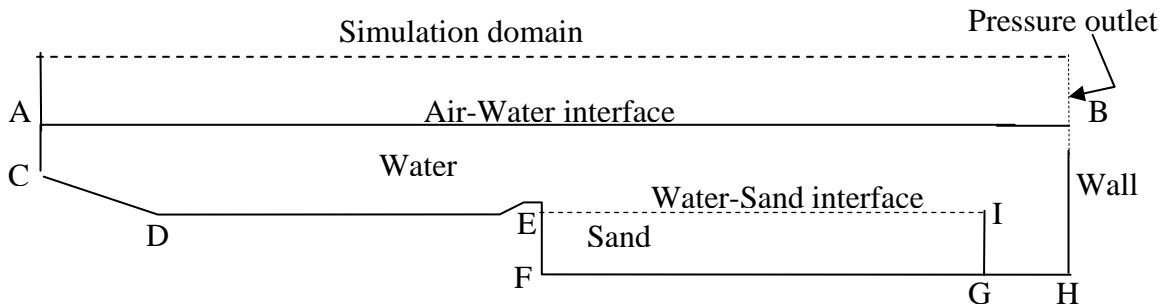


Fig.3.37 Numerical computation domain

The upstream gate is AC, with 3cm gate opening for controlled flow and fully open for uncontrolled flow at the bottom. The boundary CD is the downstream glaciis and DE is the horizontal solid apron of the barrage floor. At E, the end-sill has been modelled. Boundary AB is the air-water interface and its location has been specified as equal to the given tail water level. Thus, this assumed water surface would be correct more or less, except very close to the gate, where it would differ from the observed profile of the submerged jump. The boundary EFGI represents the base of the sand compartment. BH is the downstream outlet boundary. The boundary conditions prescribed are: zero gauge pressure at air-water interface; No flow condition at upper and lower boundaries; Uniform velocity at upstream (gate slot) boundary. The uniform velocities are worked out according to the given discharge condition for the experimental case being simulated. The flow was treated as unsteady and

time-stepped at 0.005-second interval until a steady state was achieved. The mesh structure of the model shown is here with specified boundary. The steps taken for grid generation in GAMBIT are as follows:

- a) Generation of geometry: This is done by creating points, edge and face of the geometry in two-dimensions.
- b) Meshing of lower entities: The initial geometry is divided into separate regions in order to apply constraints for the resulting mesh. This includes also the assignment of boundary regions (i.e. selected boundary of the domain which requires denser meshing).
- c) Meshing of higher entities: Based on the constraints given by the previous meshing of lower entities (mesh on the edge of a face) the final mesh was created.
- d) Defining zone: In the last stage, zone was defined for every boundary. In this case, velocity inlet was defined for gate opening and pressure outlet for outlet. Top of the model was defined as pressure outlet and rest edge was defined as a wall.

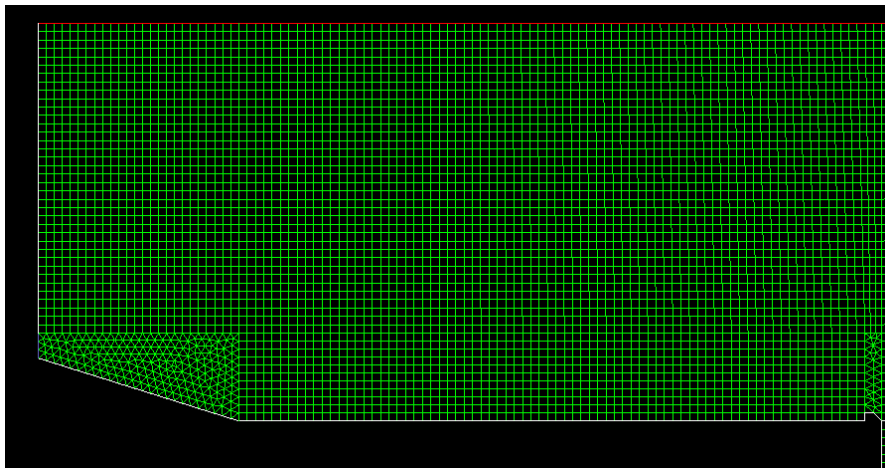


Fig. 3.38 (a) Grid from gate to end-sill of stilling basin

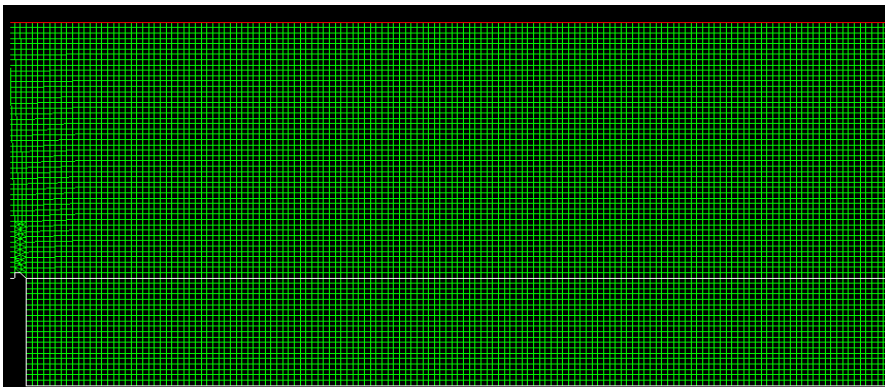


Fig. 3.38 (b) Grid from gate from end-sill to end of scour bed

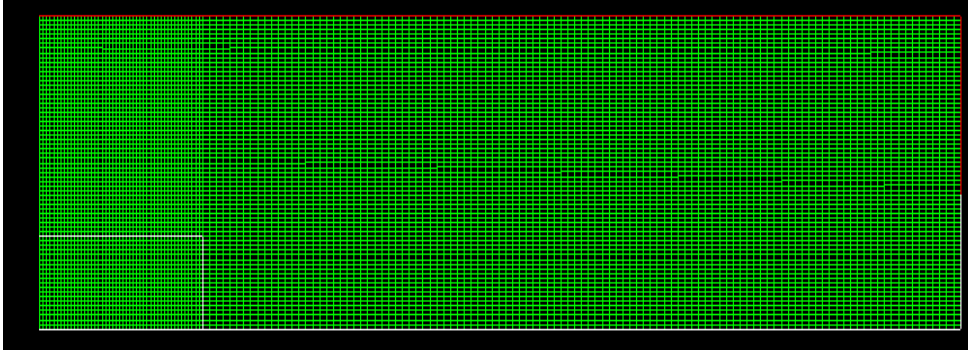


Fig.3.38 (c) Grid from gate from end of scour bed to tail gate

After grid generation, it was exported as a mesh file for use in FLUENT.

### 3.6.2 Numerical simulation using fluent

The CFD software uses the two-dimensional double precision (2ddp) solver with Eulerian multiphase model. Since, this geometry has features of very disparate length scale, single precision calculation may not be adequate to represent the nodal variation. The general conservation equations solved by **FLUENT** in Eulerian multiphase model are presented in this section, followed by the solved equations themselves.

#### *Conservation of Mass*

The continuity equation for phase q is

$$\frac{\partial}{\partial t}(\alpha_q \rho_q) + \nabla \cdot (\alpha_q \rho_q \vec{v}_q) = \sum_{p=1}^n m_{pq} \quad \text{..... (3.4)}$$

Where  $\vec{v}_q$  is the velocity of phase and  $m_{pq}$  characterize the mass transfer from  $p_{th}$  phase to  $q_{th}$  phase.

The unidirectional mass transfer model defines a positive mass flow rate per unit volume from phase  $p$  to phase  $q$  is

$$m_{pq} = \max[0, \lambda_{pq}] - \max[0, -\lambda_{pq}] \quad \text{.....(3.5)}$$

Where  $\lambda_{pq} = r \alpha_p \rho_q$  and  $r$  is a constant rate of particle shrinking or swelling.

### Conservation of Momentum

The momentum balance for phase  $q$  yields

$$\frac{\partial}{\partial t}(\alpha_q \rho_q v_q) + \nabla \cdot (\alpha_q \rho_q v_q) = -\alpha_q \nabla p + \nabla \cdot \tau_q + \alpha_q \rho_q g + \sum_{p=1}^n (R_{pq} + m_{pq} v_{pq}) + \alpha_q \rho_q (F_q + F_{lift,q} + F_{vm,q}) \quad \dots\dots\dots (3.6)$$

Where  $\tau_q$  is the  $q_{th}$  phase stress-strain tensor.

$$\tau_q = \alpha_q \mu_q (\nabla v_q + \nabla v_q^T) + \alpha_q \left( \lambda_q - \frac{2}{3} \mu_q \right) \nabla \cdot v_q I \quad \dots\dots (3.7)$$

Here  $\mu_q$  and  $\lambda_q$  are the shear and bulk viscosity of phase  $q$ ,  $F_q$  is an external body force,  $F_{lift,q}$  is a lift force,  $F_{vm,q}$  is a virtual mass force,  $R_{pq}$  is an interaction force between phases, and  $p$  is the pressure shared by all phases.

$v_{pq}$  is the interphase velocity, defined as follows. If  $m_{pq} > 0$  (i.e., phase  $p$  mass is being transferred to phase  $q$ ),  $v_{pq} = v_p$ ; if  $m_{pq} < 0$  (i.e., phase  $q$  mass is being transferred to phase  $p$ ),  $v_{pq} = v_q$ ; and  $v_{pq} = v_{qp}$ . Equation (4) must be closed with appropriate expressions for the interphase force  $R_{pq}$ . This force depends on the friction, pressure, cohesion, and other effects, and is subject to the conditions that  $R_{pq} = -R_{qp}$  and  $R_{qq} = 0$ .

### Lift Forces

For multiphase flows, **FLUENT** includes the effect of lift forces on the secondary phase particles (or droplets or bubbles). These lift forces act on a particle mainly due to velocity gradients in the primary-phase flow field. The lift force will be more significant for larger particles, but the **FLUENT** model assumes that the particle diameter is much smaller than the interparticle spacing.

The lift force acting on a secondary phase  $p$  in a primary phase  $q$  is computed from

$$F_{lift} = -0.5 \rho_q \alpha_p (v_q - v_p) \times (\nabla \times v_q) \quad \dots\dots (3.8)$$

The lift force  $F_{lift}$  will be added to the right-hand side of the momentum equation for both phases ( $F_{lift,q} = -F_{lift,p}$ ).

### ***Continuity Equation***

The equation for fluid-fluid and granular multiphase flows, as solved by FLUENT, are presented here for n phase flow. The volume fraction of each phase is calculated from a continuity equation:

$$\frac{\partial}{\partial t}(\alpha_q) + \nabla \cdot (\alpha_q V_q) = \frac{1}{\rho_q} \left( \sum_{p=1}^n m_{pq} - \alpha_q \frac{d_q \rho_q}{dt} \right) \quad \dots\dots\dots (3.9)$$

Now, **FLUENT** provides different expressions for the following steps used in the simulation.

- 1) Under define-model-solver section, following parameters have been input.
  - A. Solver- Solver contains the solution methods available for computing a solution for model. In this model, segregated solver was used. In this case a control-volume-based technique is used that consists of:
    - a) Division of the domain into discrete control volumes using a computational grid.
    - b) Integration of the governing equations on the individual control volumes to construct algebraic equations for the discrete dependent variables such as velocities, pressure, temperature, and conserved scalars.
    - c) Linearization of the discretized equations and solution of the resultant linear equation system to yield updated values of the dependent variables.
  - B. Velocity Formulation- It specifies the velocity formulation used in the calculation. The absolute velocity formulation is preferred in applications where the flow in most of the domain is not rotating.

C. Gradient Option- It contains options for setting method of computing the gradient of cell. The chosen option is cell-based method where cell center values are considered for computing the gradient. Equation solved for this method is taken from the arithmetic average of the values at the neighboring cell centers,

$$\text{i.e., } \phi_f = \frac{\phi_{c0} + \phi_{c1}}{2} \text{ where } \phi_f \text{ is the face value of cell f.}$$

D. Formulation- It specifies an implicit or explicit solution formulation. For a given variable, the unknown value in each cell is computed using a relation that includes both existing and unknown values from neighboring cells. Therefore each unknown will appear in more than one equation in the system, and implicit method was solved simultaneously to give the unknown quantities.

E. Time- It contains options related to time dependence. In this case unsteady flow is being solved.

F. Unsteady formulation- It contains options for setting different time-dependent solution formulations. This option appears only when Unsteady is enabled under Time. 1st-Order Implicit enables a time-dependent solution using first-order-accurate dual time stepping.

G. Porous Formulation- It contains option for setting the velocity in the porous medium simulation. Superficial velocity formulation was used in the present simulation.

2) Under define->model->multiphase section, Eulerian model (2 phase) has been selected. Eulerian model is best suited for granular phase flow. The modifications involve, among other things, the introduction of the volume fractions  $\alpha_1, \alpha_2, \alpha_3$  for the multiple phases, as well as mechanisms for the exchange of momentum, heat, and mass between the phases. The volume of phase  $q, V_q$  is defined by

$$V_q = \int_v \alpha_q dv \quad \dots\dots\dots(3.10)$$

$$\text{where } \sum_{q=1}^n \alpha_q = 1$$

The effective density of phase  $q$  is  $\rho_{eff} = \rho_q \alpha_q$  where  $\rho_q$  the physical density of phase  $q$  is.

- 3) Under define-model- viscous section,  $\mathcal{K} - \mathcal{E}$  model have been selected. The standard  $k - \epsilon$  model is a semi-empirical model based on model transport equations for the turbulence kinetic energy (  $k$  ) and its dissipation rate (  $\epsilon$  ). The model transport equation for  $\mathcal{K}$  is derived from the exact equation, while the model transport equation for  $\mathcal{E}$  was obtained using physical reasoning and bears little resemblance to its mathematically exact counterpart.

**Transport Equations for the Standard  $k - \epsilon$  Model:-** The turbulence kinetic energy,  $k$ , and its rate of dissipation,  $\epsilon$ , are obtained from the following transport equations:

$$\frac{\partial}{\partial t}(\rho k) + \frac{\partial}{\partial x_i}(\rho k u_i) = \frac{\partial}{\partial x_j} \left[ \left( \mu + \frac{\mu_t}{\rho_k} \right) \frac{\partial k}{\partial x_j} \right] + G_k + G_b - \rho \epsilon - Y_M + S_k$$

.....(3.11)

$$\text{and } \frac{\partial}{\partial t}(\rho \epsilon) + \frac{\partial}{\partial x_i}(\rho \epsilon u_i) = \frac{\partial}{\partial x_j} \left[ \left( \mu + \frac{\mu_t}{\sigma \epsilon} \right) \frac{\partial \epsilon}{\partial x_j} \right] + C1_\epsilon \frac{\epsilon}{k} (G_k + C3_\epsilon G_b) - C2_\epsilon \rho \frac{\epsilon^2}{k} + S_\epsilon$$

..... (3.12)

Where  $G_k$  represents the generation of turbulence kinetic energy due to the mean velocity gradients and it is calculated as  $G_k = \mu_t S^2$  where  $S$  is the modulus of the mean rate-of-strain tensor,  $G_b$  is the generation of turbulence kinetic energy due to buoyancy, calculated as  $G_b = \beta g_i \frac{\mu_t}{Pr_t} \frac{\partial t}{\partial x_i}$  where  $Pr_t$  is the turbulent Prandtl number for energy and  $g_i$  is the component of the gravitational vector in the  $i$ th direction. The coefficient of thermal expansion,  $\beta$  is defined as  $\beta = -\frac{1}{\rho} \left( \frac{\partial \rho}{\partial t} \right)_p$ ,  $Y_M$  represents the contribution of the

fluctuating dilatation in compressible turbulence to the overall dissipation rate, calculated as

$$Y_M = 2\rho\epsilon M_t^2 \text{ where } M_t \text{ is the turbulent Mach number, defined as } M_t = \sqrt{\frac{\kappa}{a^2}} \text{ where}$$

$a$  is the speed of sound,  $C_{1\epsilon}, C_{2\epsilon}$  and  $C_{3\epsilon}$  are constants.  $\sigma_k$  and  $\sigma_\epsilon$  are the turbulent Prandtl numbers for  $\kappa$  and  $\epsilon$  respectively. The turbulent (or eddy) viscosity  $\mu_t$  is computed by combining  $\kappa$  and  $\epsilon$  as follows:

$$\mu_t = \rho C_\mu \frac{\kappa^2}{\epsilon} \quad \dots\dots\dots (3.13)$$

Where  $C_\mu$  is a constant. The model constant  $C_{1\epsilon}$ ,  $C_{2\epsilon}$ ,  $C_\mu$ ,  $\sigma_k$  and  $\sigma_\epsilon$  have the following default values:  $C_{1\epsilon} = 1.44$ ,  $C_{2\epsilon} = 1.92$ ,  $C_\mu = 0.09$ ,  $\sigma_k = 1.0$ ,  $\sigma_\epsilon = 1.3$ . These defaults have been determined from experiments with air and water for fundamental turbulent shear flows including homogeneous shear flows and decaying isotropic grid turbulence.

4. Under define-model-materials section, following properties have been used for air, water and sand.

Material Name	Density(kg/m <sup>3</sup> )	Viscosity(kg/m-s)	Diameter(m)	Porosity
Air	1.225	1.7894e-5		
Water	998.2	0.001003		
Sand	2650	-	0.00098	0.4

5. Under define-phase section, water is considered as a primary phase and sand as a secondary phase with granular option enabled. These are the following properties have been used by granular material.

- a) Granular viscosity- The default expression for Syamlal et.al is



$$\mu_{s,kin} = \frac{\alpha_s d_s \rho_s \sqrt{\theta_s \pi}}{6(3 - e_{ss})} \left[ 1 + \frac{2}{5} (1 + e_{ss}) (3e_{ss} - 1) \alpha_s g_{0,ss} \right] \dots (3.14)$$

b) Granular Conductivity- The default expression for Gidaspow et.al is

$$\mu_{s,kin} = \frac{10 \rho_s d_s \sqrt{\theta_s \pi}}{96 \alpha_s (1 + e_{ss}) g_{0,ss}} \left[ 1 + \frac{4}{5} g_{0,ss} \alpha_s (1 + e_{ss}) \right]^2 \dots (3.15)$$

- c) Packing limit- it specifies the maximum volume fraction for the granular phase ( $\alpha_{s,max}$ ). For monodispersed spheres, the packing limit is about 0.63, which is the default value in **FLUENT**. In polydispersed cases, however, smaller spheres can fill the small gaps between larger spheres, so in this case maximum packing limit is 0.7.
- d) Defining the Interaction between Phases- In this case gidaspow method is used as fluid-solid drag function described by Equation

$$C_D = \frac{24}{\alpha_l Re_s} \left[ 1 + 0.15 (\alpha_l Re_s)^{0.687} \right] \dots (3.16)$$

Where  $C_D$  is the drag-coefficient,  $\alpha_l$  is the volume fraction,  $Re_s$  is the Reynolds number.

6. Under Define-Operating condition, operating pressure is taken as atmospheric pressure which has a value of 101325 Pascal. Reference pressure location is x=0 meter and y=0 meter. Reference pressure location sets the location of the cell whose pressure value is used to adjust the gauge pressure field for incompressible flows that do not involve any pressure boundaries. Gravity contains inputs for gravitational acceleration, which has of a value of -9.81 m/s<sup>2</sup> in the y-direction. In this simulation operating temperature is not involved.
7. Define- Boundary condition: This is the most important section in simulation. In this model, there are three types of zone namely velocity inlet, wall, pressure outlet is defined. These are the condition for different zone :

a). Velocity inlet: Upstream gate is defined as a velocity inlet with 3 cm gate opening. For velocity inlet, turbulence specification method is “intensity and viscosity ratio”. Turbulence

specification method specifies which method will be used to input the turbulence parameters. When the flow enters the domain at an inlet, **FLUENT** requires specification of transported turbulence quantities. It also provides guidelines for the most appropriate way of determining the inflow boundary values. It specifies the turbulence quantities in terms of more convenient quantities such as turbulence intensity and turbulent viscosity ratio.

Turbulence intensity is defined as the ratio of the root-mean-square of the velocity fluctuations,  $u'$  to the mean flow velocity,  $u_{avg}$ . A turbulence intensity of 1% or less is generally considered low and turbulence intensities greater than 10% are considered high. In this case, turbulence intensity is considered as 2%.

Turbulent viscosity ratio  $\frac{\mu_t}{\mu}$  is directly proportional to the turbulent Reynolds number. In this case this value is taken as 10%.

b) Pressure outlet: The Pressure Outlet panel sets the boundary conditions for a pressure outlet zone. Turbulent specification method is “intensity and viscosity ratio” as a value of 5% and 10 % for turbulent viscosity and turbulent viscosity ratio respectively. A set of “backflow” conditions is also specified to be used if the flow reverses direction at the pressure outlet boundary during the solution process. Backflow volume fraction for outlet must be set to zero. When the direction of the backflow re-entering the computational domain is known, and deemed to be relevant to the flow field solution, it can be specified by choosing one of the options available in the Backflow Direction Specification Method drop-down list. The default value for this field is Normal to Boundary, and requires no further input.

c) Wall: Wall boundary conditions are used to bound fluid and solid regions. In viscous flows, the no-slip boundary condition is enforced at walls by default. Base and side of the model is set as a wall. Default value is set for wall.

### ***Solution method in FLUENT***

For Eulerian multiphase calculations, **FLUENT** uses the Phase Coupled SIMPLE (PC-SIMPLE) algorithm for the pressure-velocity coupling. PC-SIMPLE is an extension of the SIMPLE algorithm to multiphase flows. The velocities are solved coupled by phases, but in a segregated fashion. The block algebraic multigrid scheme used by the coupled solver is used to solve a vector equation formed by the velocity components of all phases simultaneously. Then, a pressure correction equation is built based on total volume continuity rather than mass continuity. Pressure and velocities are then corrected so as to satisfy the continuity constraint.

#### **The Pressure-Correction Equation:**

For incompressible multiphase flow, the pressure-correction equation takes the form

$$\sum_{k=1}^n \left\{ \frac{\partial}{\partial t} \alpha_k + \nabla \cdot \alpha_k V_k - \frac{1}{\rho k} \sum_{l=1}^n m_{lk} \right\} = 0 \quad \dots\dots(3.17)$$

Where  $V_k$  is the velocity correction for  $kth$  phase.

In FLUENT, both the standard SIMPLE algorithm and the SIMPLEC (SIMPLE-Consistent) algorithm are available. For relatively uncomplicated problems (laminar flows with no additional models activated) in which convergence is limited by the pressure-velocity coupling, converged solution can be obtained by more quickly using SIMPLEC. In the present simulation, SIMPLE algorithm was used.

The choice of a particular scheme is not a clear cut issue. Some judicious experimentation of the relative stability characteristics of both schemes for a given number of iteration may be required before picking one of the solutions. The default solver or discretization scheme used was the “First order upwind” Alternatively, a higher order scheme termed the blended second Order Upward (Central Difference scheme was also applied in order to investigate the significance of the scheme. While the higher order scheme was supposed to provide improved accuracy, it was found that numerical instability occurred during the iterations. For that reason, the “First order upwind” scheme was chosen for the present analysis.

If the normalised residuals were converging stably but at a slower rate, the under relaxation factor can be increased for the velocity, turbulence kinetic energy and eddy dissipation, to speed up the convergence. However, this has to be done carefully as an increase in the under relaxation factors may also lead to a sudden divergence. An increase in the under relaxation

factors will only have an effect on the speed of convergence and not on the final converged solutions of the flow fields. Similarly, the use of pressure-velocity coupling algorithms in FLUENT, either SIMPLE or SIMPLEC, will give the same solutions when converged as both methods are only corrections of the variables. The question of which method to use only influences the convergence speed. In this simulation, the default algorithm i.e. SIMPLE was used. A trial run using SIMPLEC did not exhibit any significant increase in convergence speed.

### ***Choosing a Discretization Scheme in FLUENT***

The process of obtaining a converged solution is of great importance in the numerical simulation procedures. The residuals or normalised residuals are a measure of the degree to which each equation is satisfied throughout the flow field. Generally, a solution is well converged when the normalised residuals are of the order of  $10^{-3}$ . If the residuals have decreased to this level, are monotonically decreasing, and the flow field looks unchanged from the solution of iterations earlier, then the solution can be considered converged.

### ***Initializing the Solution***

Before starting CFD simulation, **FLUENT** needs a value with an initial "guess" for the solution flow field. There are two methods for initializing the solution:

- a. Initialize the entire flow field (in all cells).
- b. Patch values or functions for selected flow variables in selected cell zones or "registers" of cells. (Registers are created with the same functions that are used to mark cells for adaptation.)

In this simulation, solution was initialized with patch values for selected sand bed and some portion of water zone.

### ***Patching Values in Selected Cells***

After initializing the entire flow field, patching process was done with different values for particular variables into different cells. The ability to patch values in cell registers gives the flexibility to patch different values within a single cell zone. In the present simulation, a cell register was created for sand zone and another cell register was created for water zone. After

initializing the solution, the cell registers are patched with a value of 0.7 and 0.0 for the sand and water zone respectively.

After setting all these parameters, set the time step for the number of iterations to be performed. FLUENT automatically save case and data files at specified intervals during a calculation.

### 3.7 Significance of input parameters

Five non-dimensional input variables i.e Froude number ( $F_{din}$ ), upstream depth ( $\hat{H}_u$ ), tail water depth ( $\hat{H}_d$ ), water depth above crest level ( $\hat{G}$ ) and particle size ( $\hat{d}_{50}$ ) have been taken into consideration in both regression and ANN models for predicting depth of scour and position of maximum scour. It is seen from Table 3.4 that individually of all parameters water depth above crest ( $\hat{G}$ ) influences most the maximum depth of scour and position of maximum scour. Various input combinations are considered as shown in Table 3.4 by adding input variables one by one and their influence on testing the data set have been studied by evaluating RMSE and r value. Though all possible combinations using two, three, four variables are tested, only that giving the best result is presented in table. It may also be observed that the combination of all five parameters gives almost the same result as with the best combination of four parameters. It may therefore be conclude that the upstream water depth  $H_u$ , is redundant once the inflow Froude number ( $F_{din}$ ) is considered.

Table 3.4. Sensitivity analysis of variables for regression model

Input variables	$\hat{d}_s (d_s/b_e)$		$\hat{X}_s (X_s/b_e)$	
	r	RMSE	r	RMSE
$F_{din}$	0.614	1.0293	0.745	3.762
$H_u/b_e$	0.726	0.898	0.864	2.850
$H_d/b_e$	0.753	0.859	0.884	2.642
$G/b_e$	0.780	0.818	0.898	2.486
$d_{50}/b_e$	0.741	0.842	0.868	2.791
$H_u/b_e, H_d/b_e$	0.892	0.598	0.949	1.783

$F_{din}, H_u/b_e, G/b_e$	0.928	0.482	0.954	1.671
$F_{din}, H_d/b_e, G/b_e, d_{50}/b_e$	0.982	0.255	0.993	0.656
$F_{din}, H_u/b_e, H_d/b_e, G/b_e, d_{50}/b_e$	0.982	0.247	0.995	0.532

## References:

1. Liriano, S.L., Day, A.R. and White, A.R. (2002) Scour at culver outlets as influenced by the turbulent flow structure. *Journal of Hydraulic Research*, 2002, 40, No. 3, 367-376.
2. SPSS (2000) SPSS for windows ver.9.0. *SPSS Institute, Inc.*, Chicago, Illinois.
3. MATLAB. (2003) *Neural network tool box version 4.0*. The Math works, Inc., Matick, Mass.
4. ASCE Task Committee (2000). The ASCE Task Committee on Application of artificial neural networks in hydrology. *J. Hydrologic Engineering*, ASCE, 5, No. 2, 115-137.
5. Rojas. R (1996) “Neural Networks” Springer Verlag, Berlin
6. Azmatullah H. Md., Deo M.C. and Deolalikar P.B. (2005) Neural Networks for Estimation of Downstream of Ski-Jump Bucket. *Journal of Hydraulic Engineering*, ASCE, 131, No. 10, 898-908.

## CHAPTER 4

### **NON-UNIFORM GATE OPERATION**

#### **4.1 Non-uniform gate operation condition**

Non-uniform gate opening condition often occurs for barrages as it almost becomes essential to manage the flood condition by operating the gates according to the flow, sediment concentration and the pattern of the deposited shoals in the upstream pond or on the immediate downstream of the gates. This section discusses the experimental setup to investigate into the flow characteristics and its effects on scour for this condition.

The water flowing through the bays of a barrage passes through the weir section and is controlled by respective gates located over the weir crests and supported by the piers. The three bays barrage model consisting three vertical gates which can move vertically to get desired gate opening for each bay. Downstream of each gate are the inclined glacis of the weir followed by the horizontal stilling basin apron where the emerging gate-controlled undershot jet of water meets the tail water governed by the river downstream forming a hydraulic jump and dissipating excess energy. The length of horizontal stilling basin aprons were varied in three different sizes 0.74 m, 0.56 m and 0.41 m which is shown in Fig. 4.1 as  $L_{sa}$ . Then experiments were conducted for non-uniform (unequal) gate opening of three bays for different flow situations and observed bed scour profile. In nonuniform condition only one gate essentially middle gate of three bays was opened partially and fully with other two side gates were remain closed and open equally. Major emphasis was given for one gate opening conditions whether it may be controlled or uncontrolled to study the scour bed profile due to different hydraulic conditions. Three different sands sizes 0.00024 m, 0.00049 m and 0.00092 m known as fine sand, medium sand and coarse sand were also taken to study the effect of particle sizes on scour. All experimental conditions only for 0-F-0 gate operation conditions are shown in Table 4.1 and besides these experiments other gate opening conditions were also used for experiment i.e., 2-F-2, 3-F-3 and 4-F-4 details given in Fig.4.2.

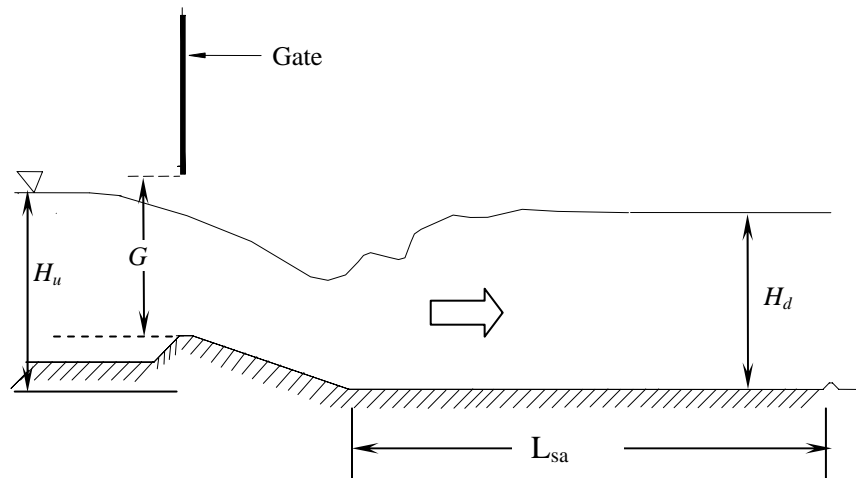


Fig.4.1 Typical longitudinal cross section of barrage bay showing the various parametrs

Table 4.1 Uncontrolled gate opening for middle gate experimental conditions

Phase No.	Type of gate opening	Length of horizontal apron ( $L_{sa}$ ) in m	Sand type and size ( $d_{50}$ ) in m.	Total discharge ( $m^3/s$ )	Flow type (Uncontrolled)
I	0-F-0	0.74	cs (0.00092)	0.0295	Free and submerged
				0.0387	Free and submerged
				0.0492	Free and submerged
			ms (0.00049)	0.0295	Free and submerged
				0.0387	Free and submerged
				0.0492	Free and submerged
			fs (0.00024)	0.0295	Free and submerged
				0.0387	Free and submerged
				0.0492	Free and submerged
		0.56	cs (0.00092)	0.0295	Free and submerged
				0.0387	Free and submerged
				0.0492	Free and submerged
		0.41	cs (0.00092)	0.0191	Free and submerged
				0.0247	Free and submerged
				0.0295	Free and submerged

\*0-F-0 means middle gate fully open (ungated middle bay) and side gates closed



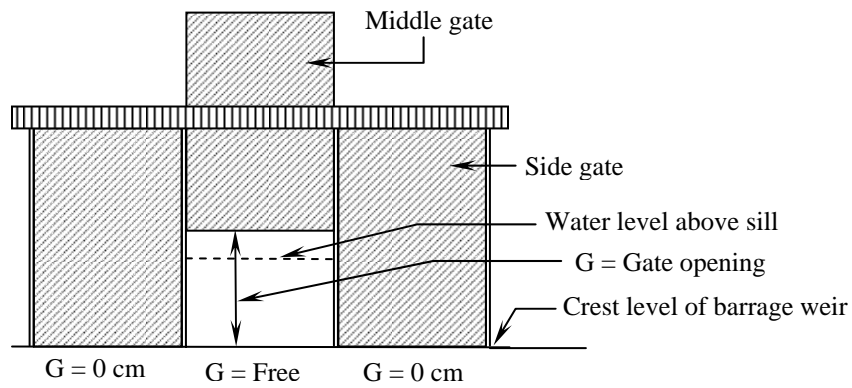


Fig.4.2(a) (0-F-0)

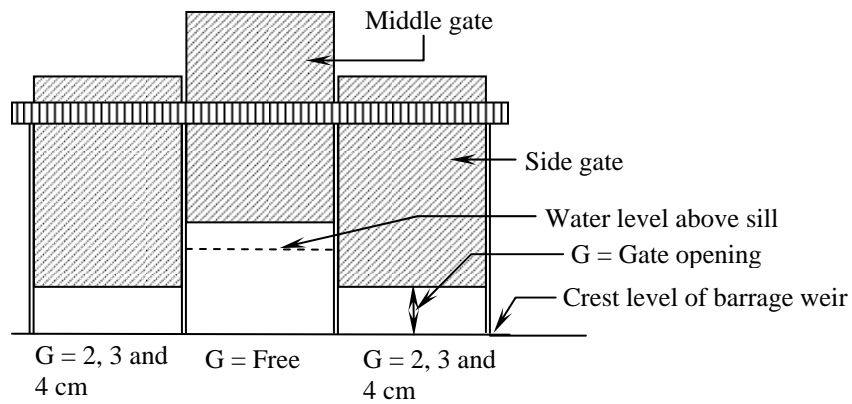


Fig.4.2(b) (2-F-2), (3-F-3) and (4-F-4)

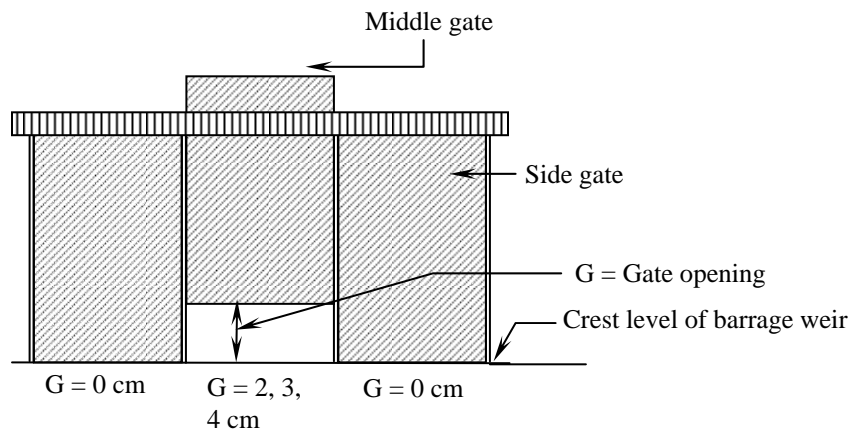


Fig.4.2(c) (0-2-0), (0-3-0) and (0-4-0)

Fig. 4.2 Different gate opening conditions shown in (a) only middle gate free(ungated) and two side gates closed (0-F-0) (b) middle gate free and side gate open gradually 2,3 and 4 cm (2-F-2, 3-F-3 and 4-F-4) (c) Only middle gate open 2,3 and 4 cm. (0-2-0, 0-3-0 and 0-4-0)

### ***Contour of Scoured bed profile***

The contour lines in the scour bed for non uniform gate operation of three bays of barrage were measured by placing point gage at all nodes shown in Fig 4.3 along seven lines which are along the direction of flows (x direction) and in the width wise direction or lateral direction (y direction) to enable the study of scour pattern.

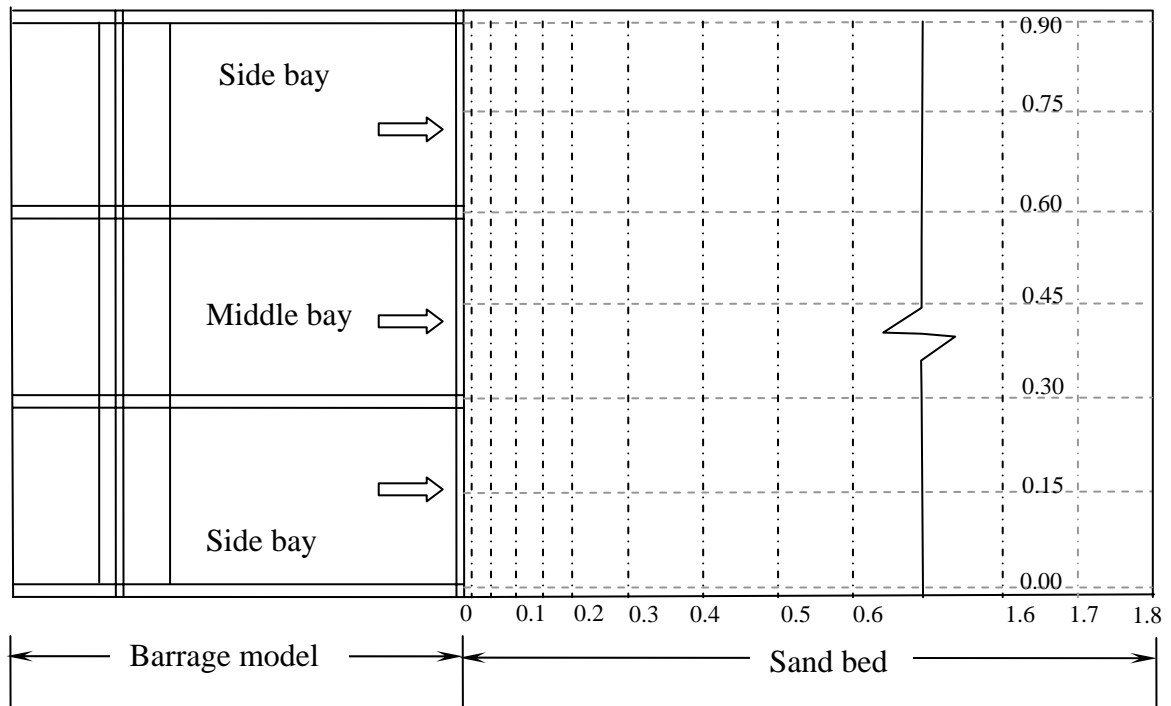


Fig. 4.3 showing grid for bed contour measurement on nodal points of non uniform gate operation



Fig. 4.4 Photograph after experimental run showing middle gate full open and two side gates closed with scour bed (0-F-0)



Fig. 4.5 Photograph after experimental run showing middle gate partially open and two side gates closed with scour bed (0-3-0)

### ***ANN Model***

An ANN model was developed for predicting non uniform scour profile taking all the gate opening conditions. For predicting the depth at different location of scour bed four lines of scour profile, i.e., along the side line (glass wall) just at the starting of width of bay, along the centre line of first bay 0.15 m away from first line, along the centre line of pier 0.30 m away and along the centre line of middle bay at 0.45 m away from first line were taken for ANN modelling. As the flume is 0.9 m width the line at centre of middle bay is the centre line of flume also. For four line four no. ANN model have been developed which predict the scour values at different points along each line for same hydraulic parameters.

The predicted through ANN model compared with observed scour profile and giving satisfactory prediction except first line which is along the glass wall and may be due to wall effect. For 0.0387 m<sup>3</sup>/s total discharge and horizontal stilling basin length 0.74 m scour depth was measured with point gage at all nodes as shown in Fig. 4.3 and using SURFER package contour profile was drawn for whole scour bed and shown in Fig. 4.6. Similarly bed profile was also drawn for predicting data from ANN model by using same package and shown in Fig. 4.7. As this experiment was for one gate operation (0-F-0) the scour profile drawn by SURFER giving same results as observed and shown in photograph Fig. 4.4 where maximum scour occur at the centre line of both the pier and location of maximum scour depth 0.4 m away from endsill of the stilling basin. The upstream water depth  $H_u = 0.27$  m and downstream water level  $H_d = 0.22$  m and the flow was submerged flow.

But when free flow occur for same discharge and same gate opening conditions the maximum scour depth occur along the centre line of pier and the location of maximum scour depth observed near the endsill means which may be endanger for sheet pile of horizontal stilling basin. In this conditions tail depth was 0.15m and shown in Fig. 4.8, in which dotted line shown initial bed level of scoured bed (at starting of experiments)

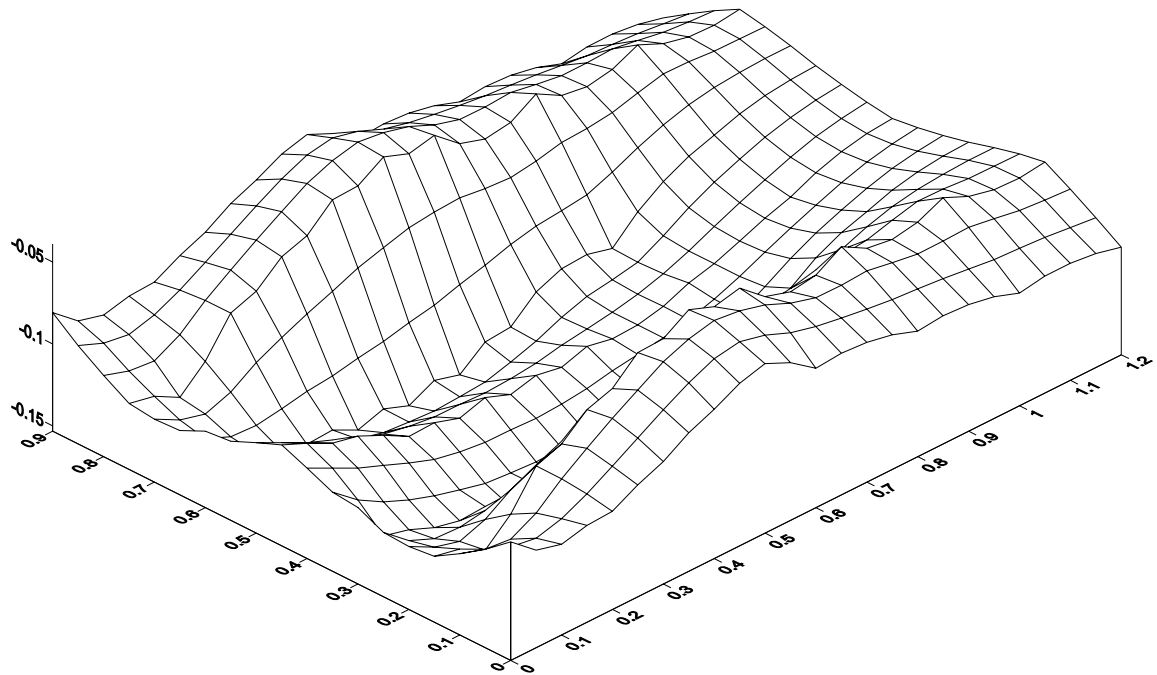
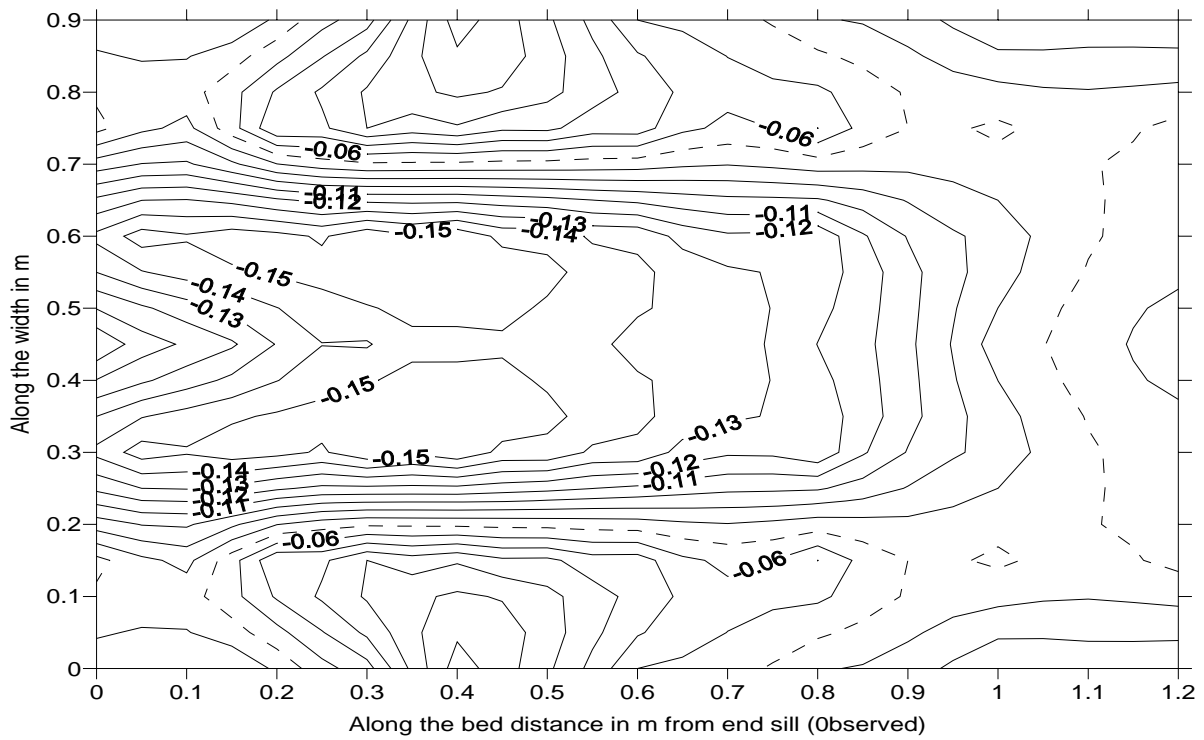


Fig. 4.6 Scour profile for 0-F-0 gate operation as observed using point gage and discharge (Q) 0.0387 cumec. for uncontrolled submerged condition (observed)

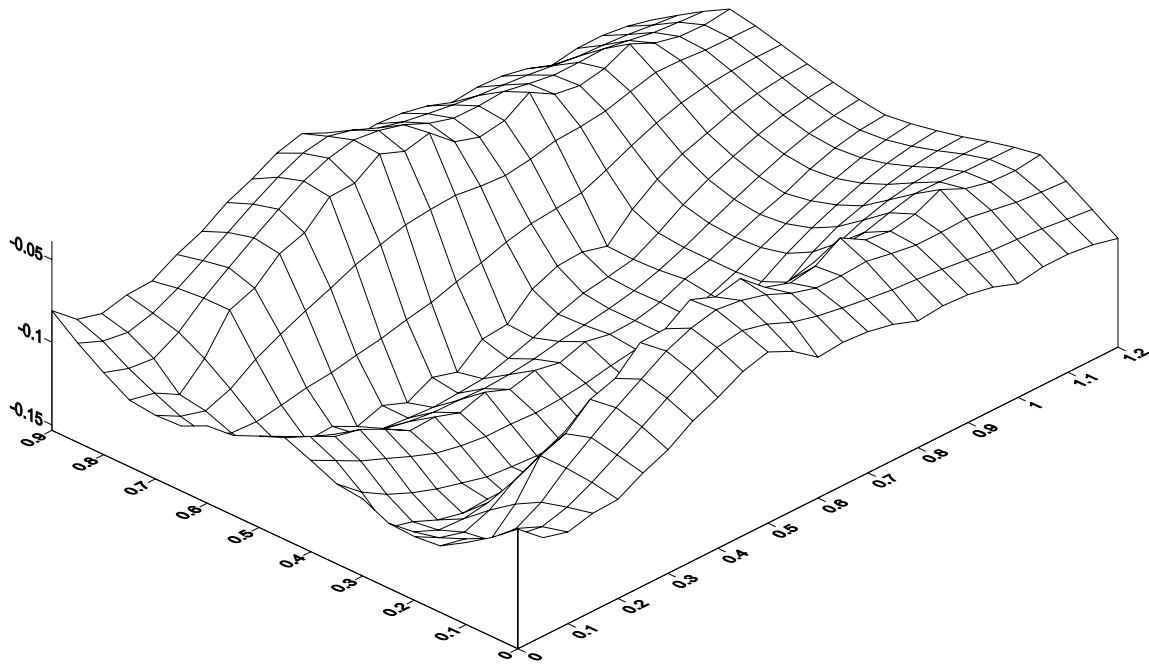
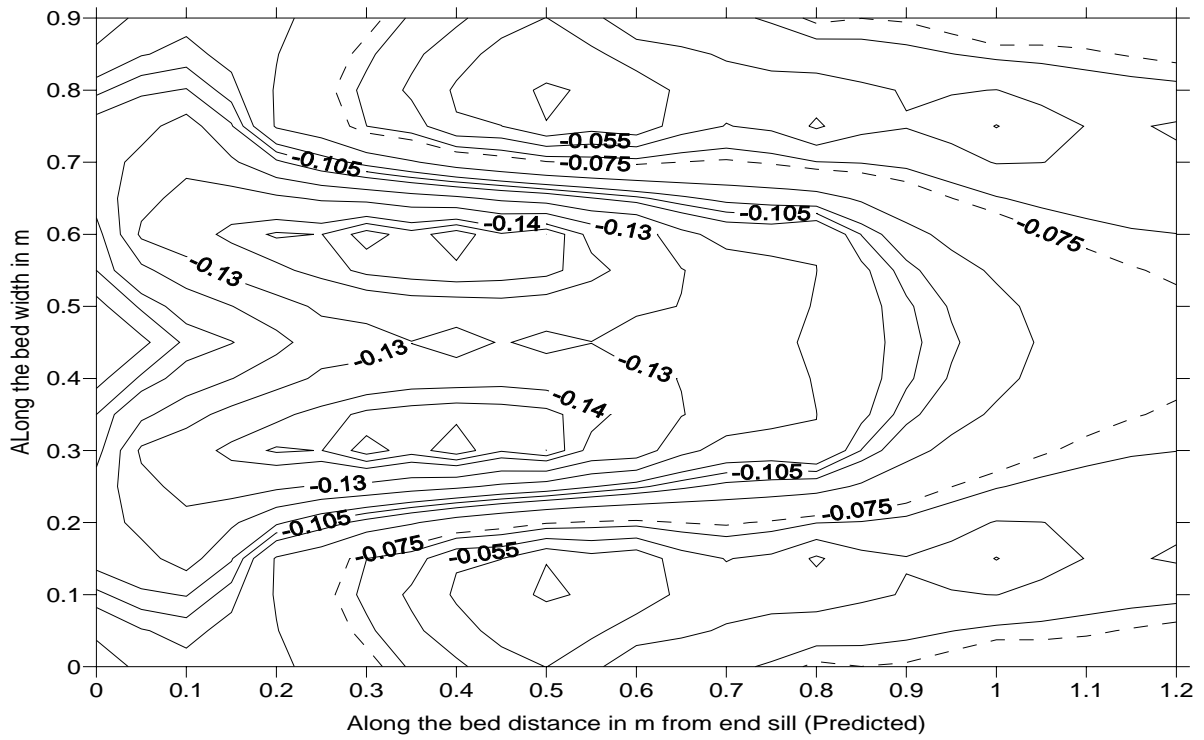


Fig. 4.7 Scour profile for 0-F-0 gate operation as observed using point gage and discharge (Q) 0.0387 cumec. for uncontrolled submerged condition (predicted-ANN)

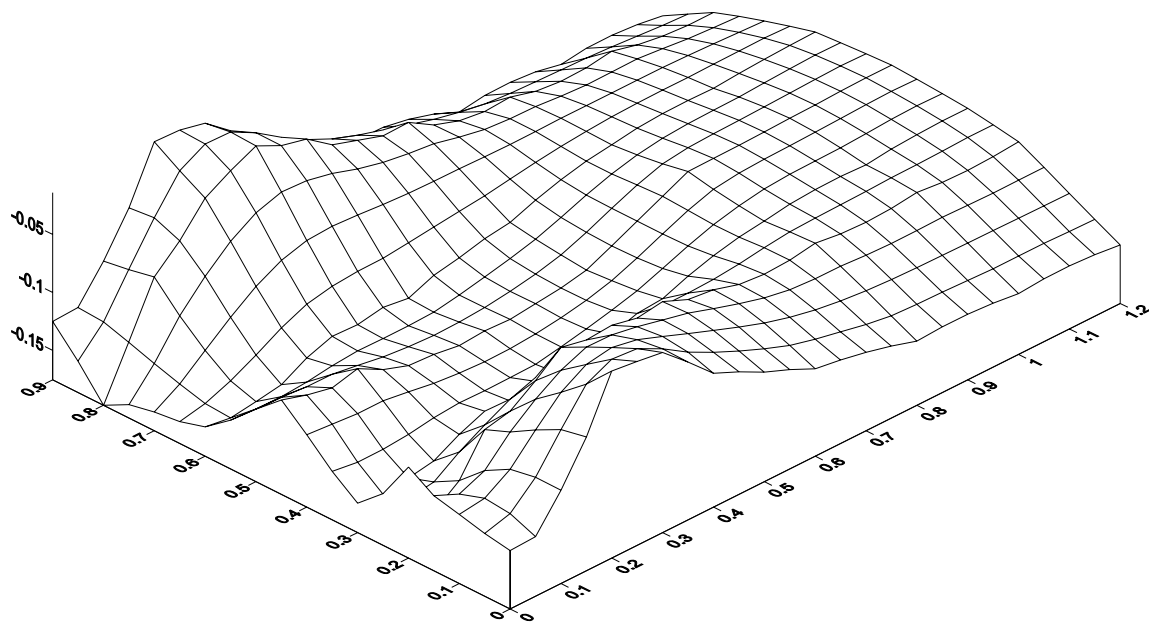
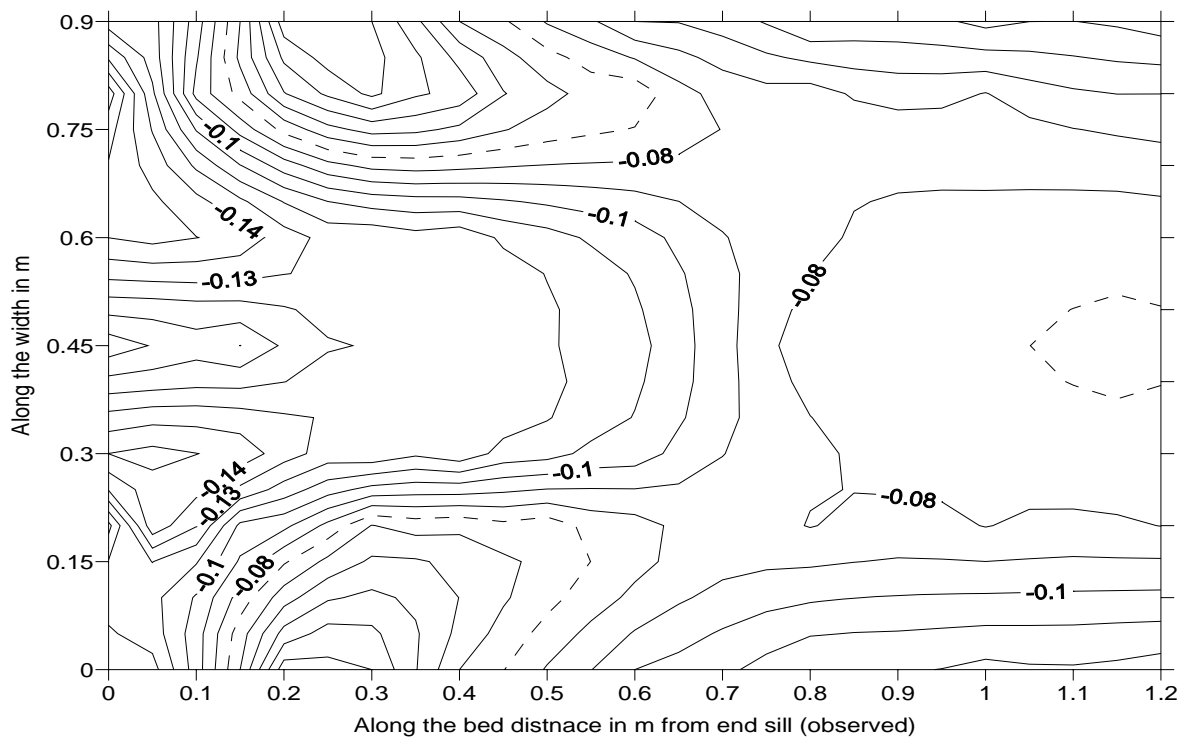


Fig. 4.8 Scour profile for 0-F-0 gate operation as observed using point gage and discharge (Q) 0.0387 cumec. for uncontrolled free flow condition (observed)

## CHAPTER 5

### DEPRESSED FLEXIBLE APRON

#### 5.1 Depressed flexible apron for scour reduction

It is observed for some barrages abroad, for example, the Qadirabad Barrage on River Chenab in Pakistan (Fig. 5.1), a depressed pool is provided just downstream of the stilling basin. It is felt that this is to reduce the scour taking place just downstream of the energy dissipating arrangement of a barrage. In this section we discuss our experimentations with the normal flexible apron of a barrage shaped into different configurations, with a view to investigate the effect on the reduction of scour downstream of the structure.

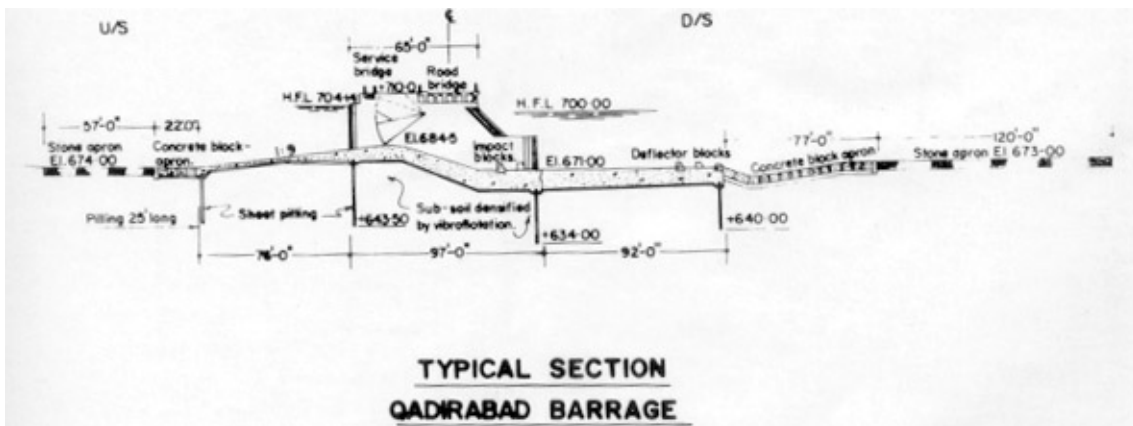


Figure 5.1 A typical section through the the Qadirabad Barrage in Pakistan

#### 5.1 Present Practice of laying Flexible Apron

Protection works are provided on the upstream as well as on the downstream of barrage in order to safeguard the possibility of the scour hole traveling close to solid floor downstream apron of the barrage and to relieve any residual uplift pressure through the filter. The protection work downstream of a barrage is shown in Fig 5.1. These protection works consist of

- (i) Inverted filter
- (ii) Block Protection
- (iii) Launching apron.



### ***Inverted filter***

An inverted filter consists of layers of materials of increasing permeability from bottom to top. It reduces the possibility of piping as it allows free flow of seepage water through itself without allowing the foundation soil to be lifted upward.

### ***Block protection***

(a) Upstream Block Protection: - Just beyond the upstream end of the impervious floor pervious protection comprising of cement concrete blocks of adequate size laid over loose stone shall be provided. The cement concrete blocks shall be of adequate size so as not to get dislodged, and shall generally be of  $1500 \times 1500 \times 900 \text{ mm}$  size for barrages in alluvium reaches of rivers. The length of upstream block protection shall be approximately equal to  $D$ , the design depth of scour below the floor level.

(b) Downstream Block Protection: - Pervious block protection shall be provided just beyond the downstream end of impervious floor. It shall comprise of cement concrete blocks of adequate size laid over a suitably designed inverted filter for the grade of material in the river bed. The cement concrete blocks shall generally be not smaller than  $1500 \times 1500 \times 900 \text{ mm}$  size to be laid with gaps of 75 mm width, packed with gravels. The length of downstream block protection shall be approximately equal to  $1.5D$ . Inverted filter with block protection is provided in part of the length and block protection only in remaining length.

### ***Launching apron***

A launching apron is an apron of loosely packed stones. The function of a launching apron is to protect the impervious floor and the pile from the scour holes progressing towards the floor and the pile.

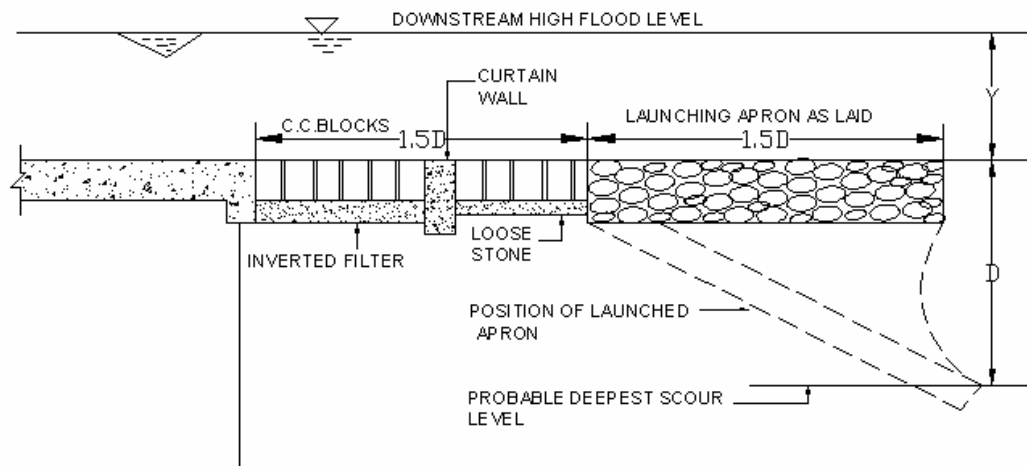
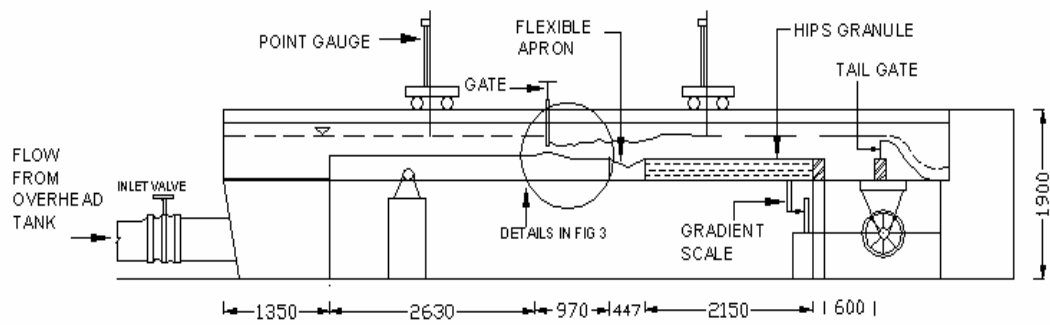


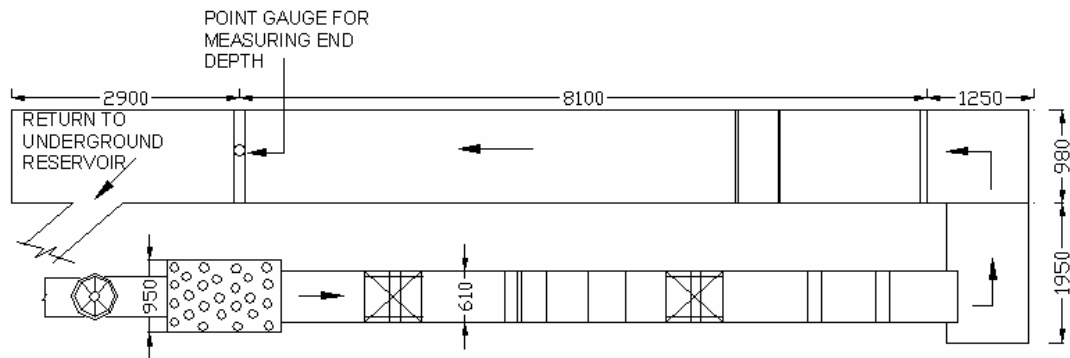
Figure 5.2 Downstream protection work of a barrage

## 5.2 Experimental set up for fixing the shape of the Flexible Apron

The schematic layout of the experimental setup is shown in Fig. 5.3. HIPS (High Impact Polystyrene) granules of specific gravity 1.054 are being used for comparing the scour profile of different configuration under four tail water conditions. Cement Concrete cubes of 30mm sizes are used for making different configuration in flexible apron. The discharge in the flume is measured by end depth method in the return channel.



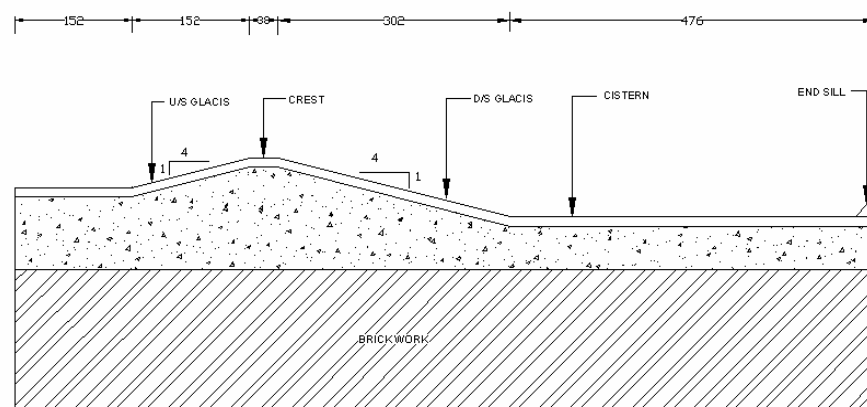
Sectional side view



Top view

All dimensions are in mm

Fig. 5.3 Schematic Layout of the experimental set-ups

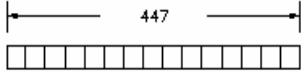
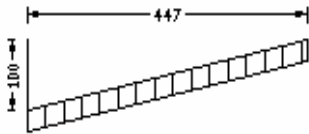
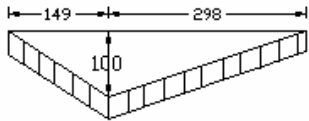
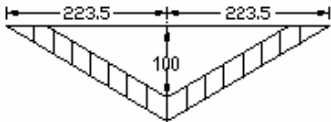
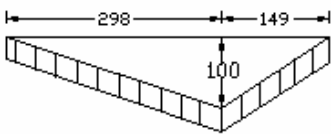
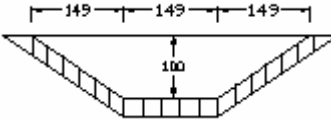


All dimensions are in mm

Fig.5.4. Details of the solid apron portion of the barrage

Experiments were carried out for six configurations each under four tail water conditions (two free flows and two submerged flows). The discharge in the flume was 10 lts/s and gate opening was 20mm for all the experiments. The comparison of maximum scour for different configuration is shown in the Table 5. 1.

Table 5.1. Different configurations of depressed apron experimented

Configuration of the Flexible Apron	Designation	Maximum scour depths (in mm) for different tail gate height (in mm)			
		95	105	155	135
	S1	138.5	129.5	107	105
	S2	122.4	122	105	96
	S3	122	118.4	93	70.8
	S4	126	124.5	113.5	100
	S5	134.2	132.1	110	126.4
	S6	143	132	117.5	115

The scour profile for the different configurations are shown in Figs. 5.5 to 5.8.

### 5.3 Inferences drawn from experimental observation on depressed floor

From the experiments it was observed that, by providing depression in the form of a pool in the flexible apron the scour in the downstream gets reduced. However, the extent of reduction depends upon the shape. By arranging CC blocks of flexible apron in the shape **S3**, there was maximum reduction of scour. The flow conditions for this shape has been studied in details using ADV and simulated using FLUENT. This is provided in the following section.

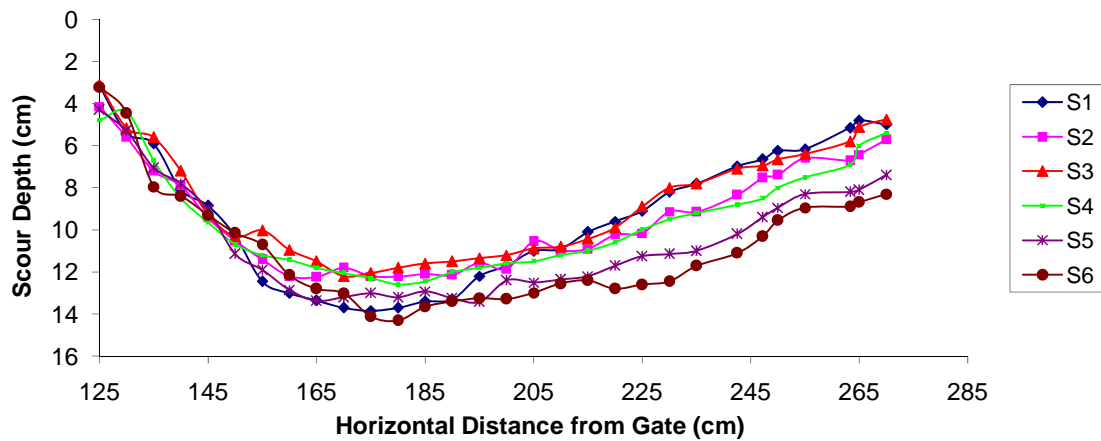


Fig. 5.5 Scour Profile for 95mm Tailgate height

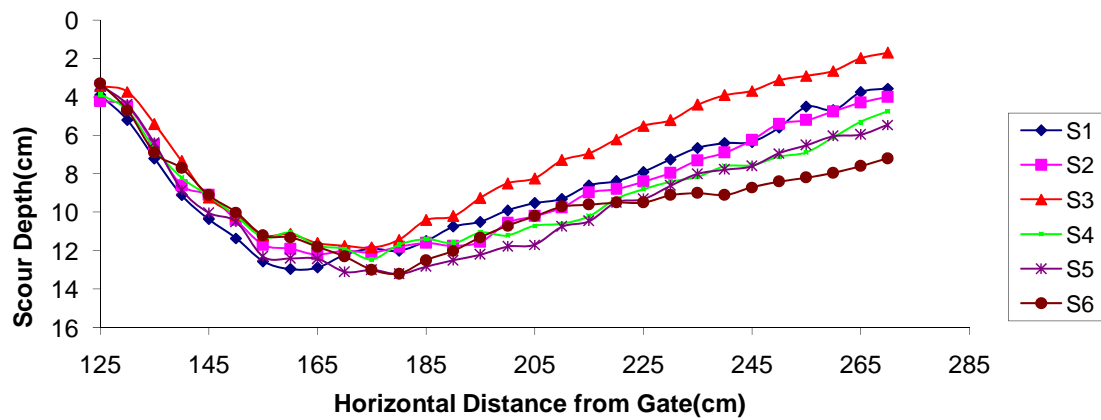


Fig. 5.6 Scour Profile for 105mm Tailgate Height

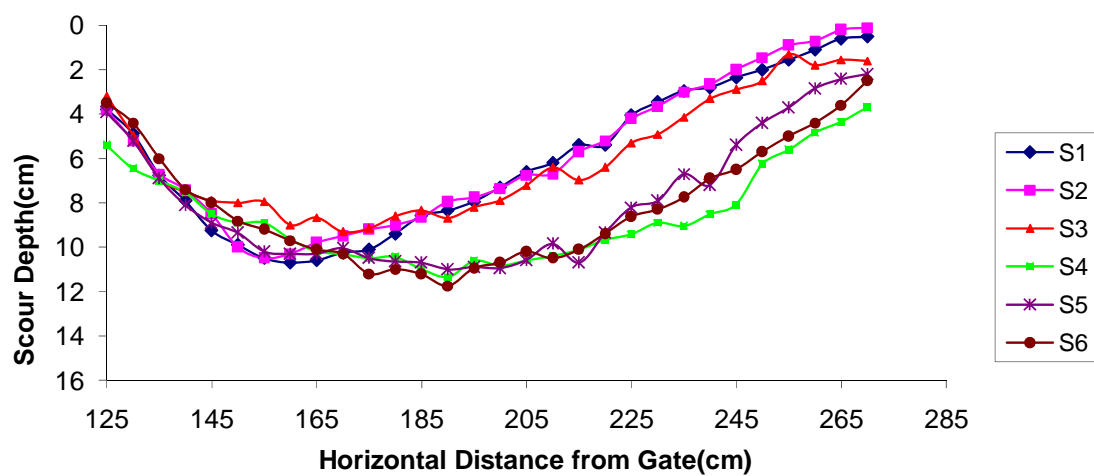


Fig. 5.7 Scour Profile for 125mm Tailgate height

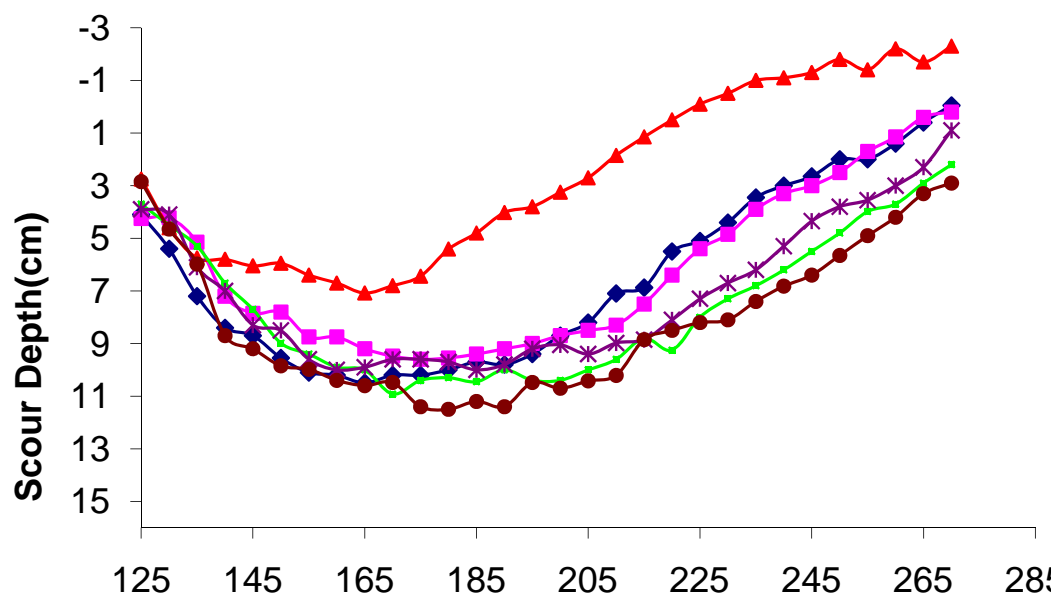


Fig. 5.8 Scour Profile for 135mm Tailgate height

## 5.4 Behavior of Depressed Flexible Apron

The flow behaviour of the depressed flexible apron so selected from the experimental observations in the preceding sections was investigated in detail using Acoustic Doppler Velocity meter probe (ADVANCE) as well as by a numerical study using the CFD package FLUENT. This section discusses these steps in detail.

### 5.4.1 Measurement of flow characteristics with ADV

A SonTek make 5cm down looking ADV probe was used to measure the instantaneous velocity components in the flume. The ADV readings were taken along the centre line of the flume at different stream wise distances from the end of the stilling basin. The ADV operates on a pulse-to-pulse coherent Doppler shift to provide instantaneous three-dimensional velocity components at a sampling rate of 50 Hz. The acoustic sensor comprises of transmitting transducer and receiving transducers. The receiving transducers are mounted on short arms around the transmitting transducer. The beams traveling through the water arrived at the measuring point (5cm below the transducer), where they are reflected by the ambient particles within the flow, being receives by the receiving transducers. The processing module processes the digital signals required to measure the Doppler shifts. The data acquisition software (WinADV) provides a real time display of the data in graphical and tabular form.

Experiments were run for controlled free and controlled submerged conditions over horizontal and inclined flexible aprons. The ADV was used to collect turbulence in the longitudinal ( $u'^2$ ), vertical ( $v'^2$ ), and lateral ( $w'^2$ ) directions at 10cm interval along the centerline of flexible apron and along the vertical at very close interval. The turbulent kinetic energy at each sampling point was calculated using these measurements and applying the following equation:

$$k = \frac{1}{2}((\sqrt{u'^2} + \sqrt{v'^2} + \sqrt{w'^2})^2 \quad \dots (5.1)$$

Here,  $\sqrt{u'^2}$ ,  $\sqrt{v'^2}$  and  $\sqrt{w'^2}$  are the root mean squares of the velocity fluctuations in the longitudinal lateral and vertical directions respectively.

The details of the software package FLUENT with which the flow patterns were studied have already been presented in Chapter 3. However, the general views of the computational grid with horizontal and depressed flexible aprons are presented in Figs. 5.9 and 5.10 respectively.

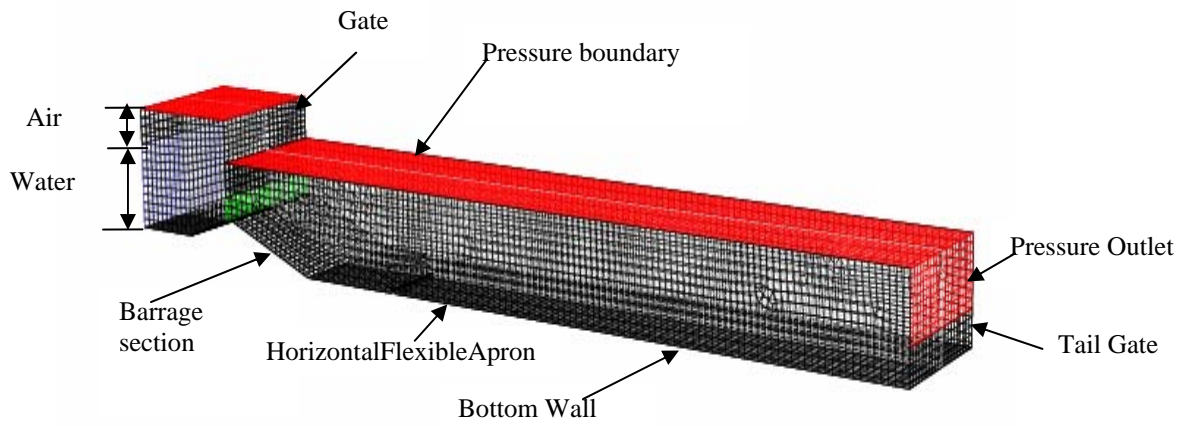


Fig. 5.9 View of three-dimensional grid of horizontal flexible apron flow domain

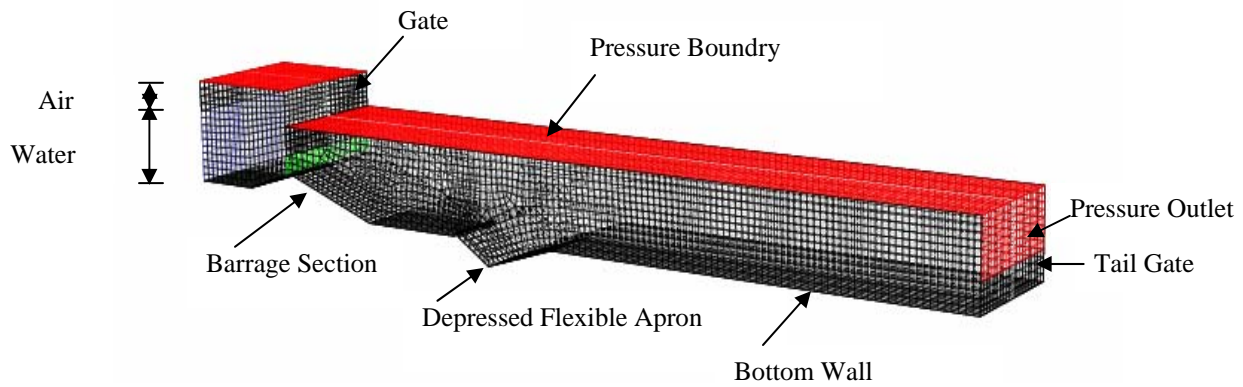


Fig. 5.10 View of three-dimensional grid of depressed flexible apron flow domain



### **5.4.2 Inferences drawn from the experimental observations and numerical computations about flow and energy dissipation within the depressed flexible apron**

The turbulence kinetic energy (KE) as computed using Eq. 5.1 based upon the observed velocity fluctuations measured using ADV for the controlled free and submerged conditions are shown in Figs. 5.11 and 5.12 respectively. Similarly, KE computed using the CFD software package FLUENT for the two cases have been presented in Figs. 5.13 and 5.14 respectively. As may be noticed, for both cases the turbulence kinetic energy for the depressed flexible apron is lower at the depression as compared to the horizontal configuration. The observed KE using ADV readings and that computed using the software package FLUENT are seen to agree well in Figs. 5.15 through 5.18. At the downstream end of the apron the turbulence kinetic energy is less for the depressed flexible apron in comparison with horizontal flexible apron for all the cases of controlled free and submerged flows. Here as the flow enters downward in the inclined portion of the flexible apron it distributes its momentum throughout a greater mass and much of the kinetic energy is converted into heat by creation of relatively fine grained turbulence.

The velocity vector diagrams are next presented in Figs. 5.19 through 5.22. It is observed that for the depressed flexible apron, a jet rises to the surface, which is clearly seen in the respective velocity vector diagrams. The kinetic energy being dissipated in a vertical direction, no high velocity currents or large concentrations of flow are directed against the bed, thus resulting in less scouring.

### **5.4.3 Recommendations**

It may thus be recommended that the flexible apron for barrages may henceforth be designed in a depressed form which shall reduce the probability of scouring. The recommended shape is in the form S3 as discussed earlier, in which the depression is located at  $1/3^{\text{rd}}$  distance (of the length of the flexible apron) from its upstream end. Thus, the depressed shape of the flexible apron would be steeper towards the upstream compared to its adverse slope on the downstream.

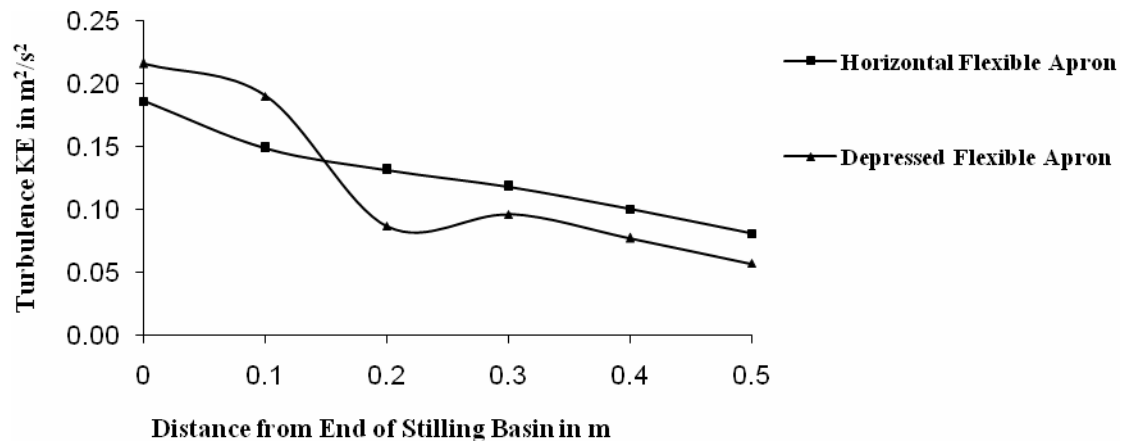


Fig. 5.11 Turbulence Kinetic Energy Downstream of Stilling Basin for Contolled Free Jump using ADV data

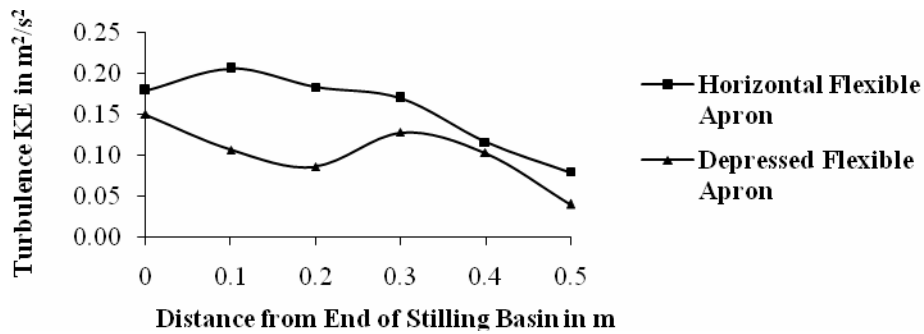


Fig. 5.12 Turbulence Kinetic Energy Downstream of Stilling Basin for Controlled Submerged Jump using ADV data

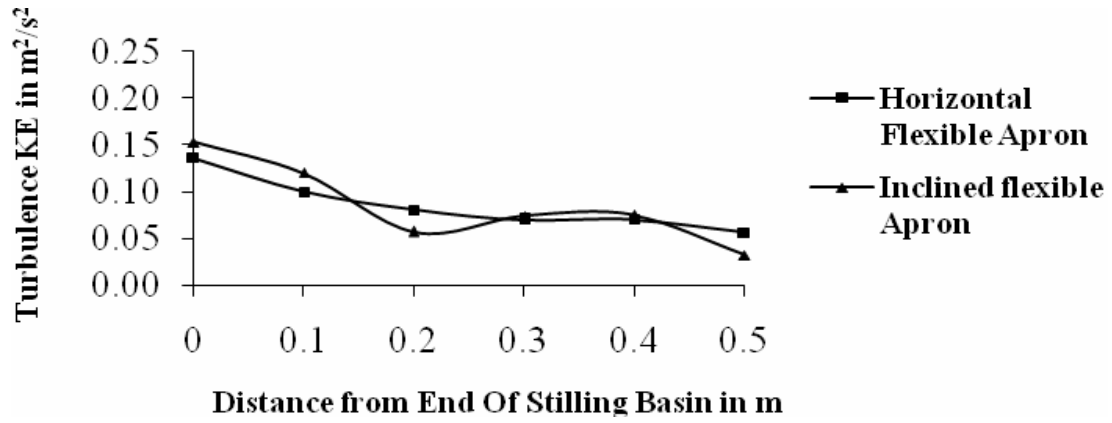


Fig. 5.13 Turbulence Kinetic Energy Downstream of Stilling Basin for Contolled Free Jump using FLUENT computed results

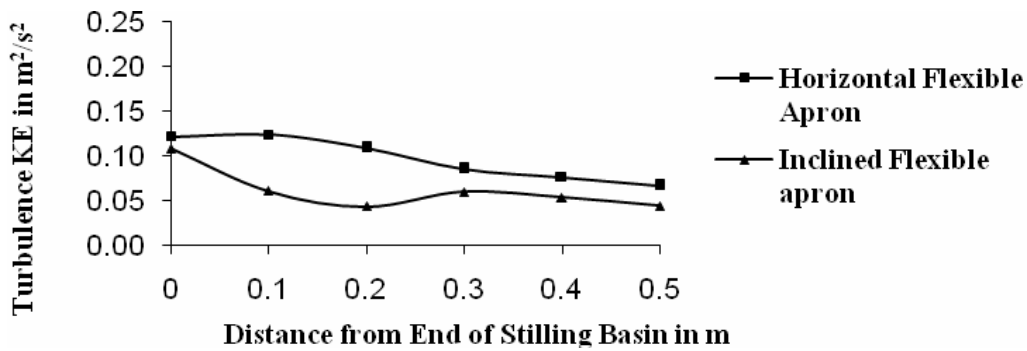


Fig. 5.14 Turbulence Kinetic Energy Downstream of Stilling Basin for Contolled Submerged Jump using FLUENT computed results

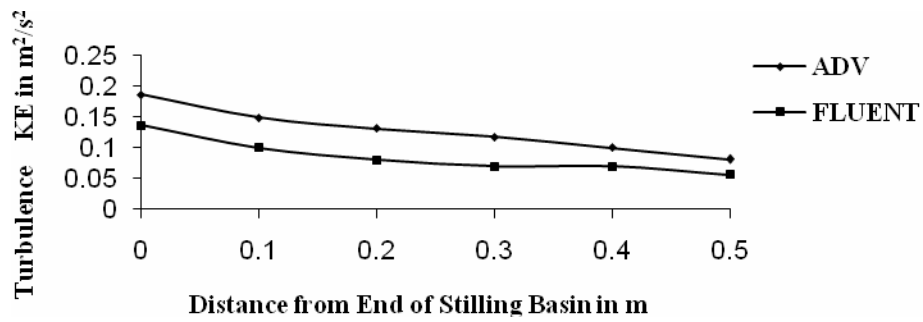


Fig. 5.15 Turbulence Kinetic Energy comparison in Horizontal Flexible Apron for Controlled Free Jump

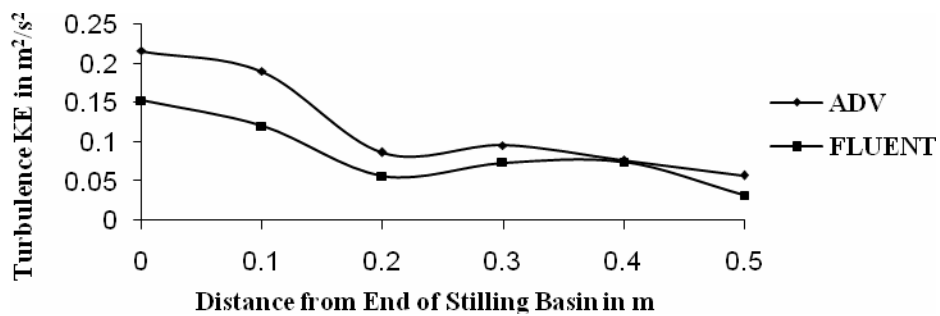


Fig. 5.16 Turbulence Kinetic Energy comparison in Inclined Flexible Apron for Controlled Free Jump

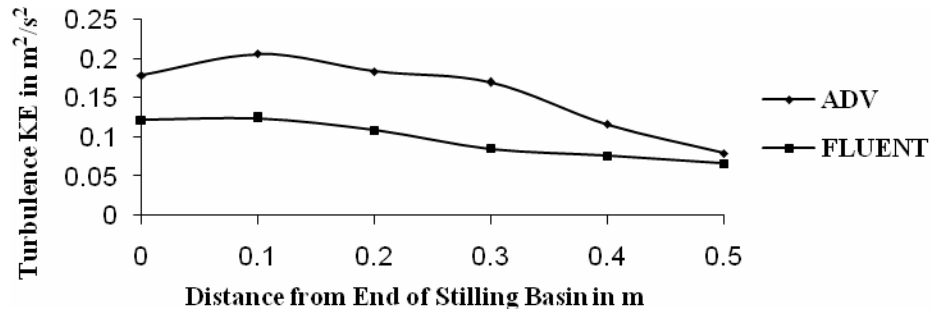


Fig. 5.17 Turbulence Kinetic Energy comparison in Horizontal Flexible Apron for Controlled Submerged Jump

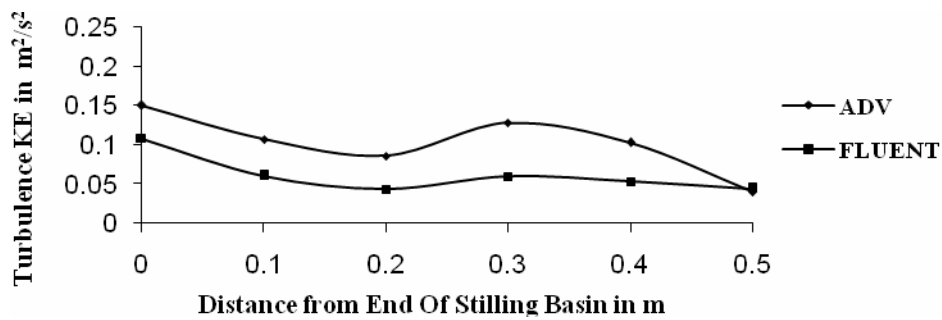


Fig. 5.18 Turbulence Kinetic Energy comparison in Inclined Flexible Apron for Controlled Submerged Jump

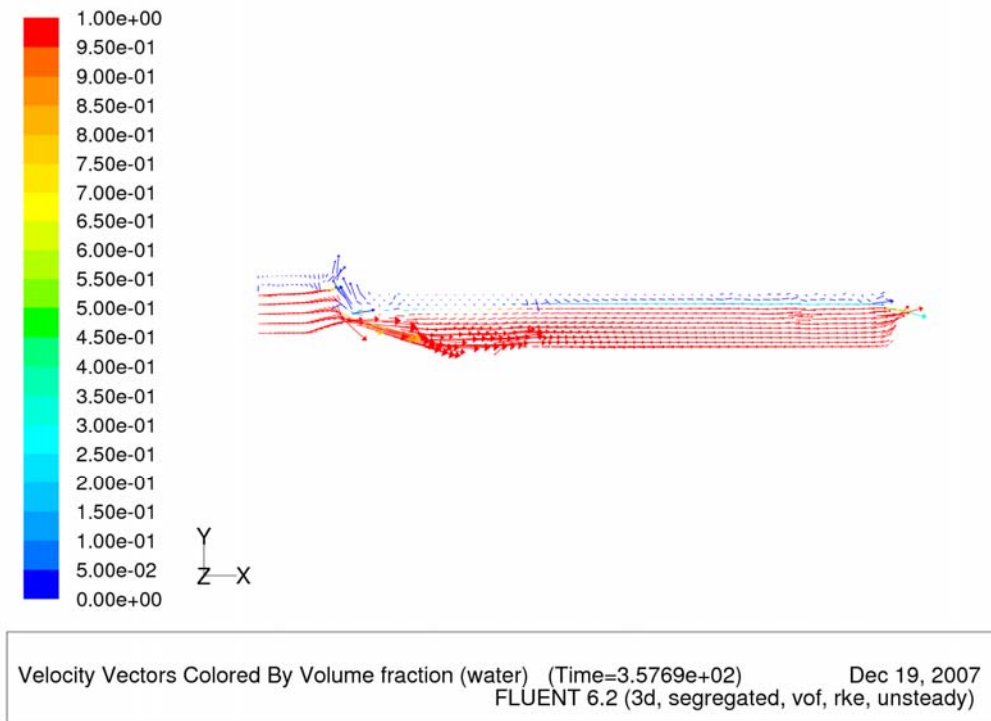


Fig. 5.19 Velocity Vectors for Controlled Free Jump in Barrage with Horizontal Flexible Apron

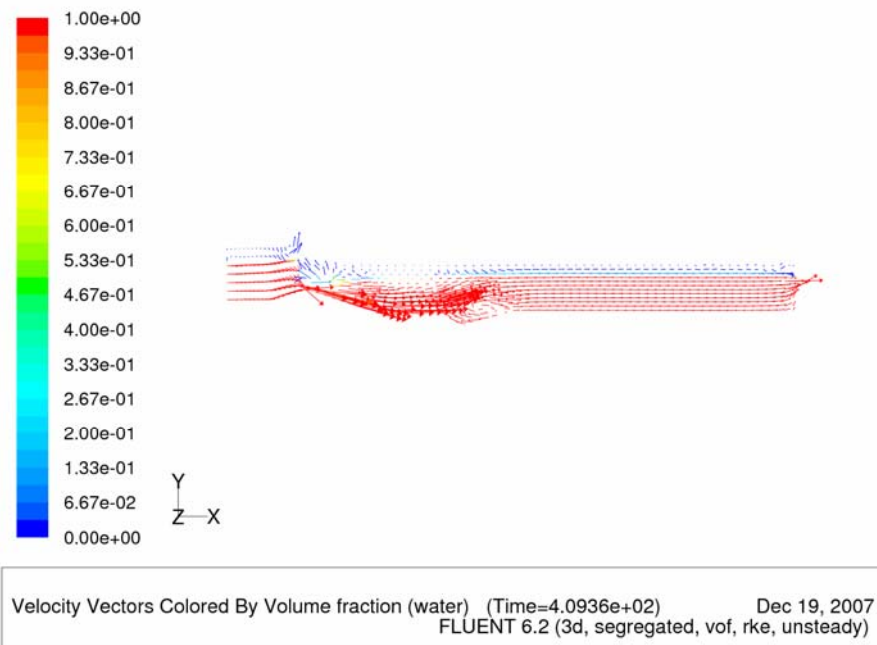


Fig. 5.20 Velocity Vectors for Controlled Free Jump in Barrage with Inclined Flexible Apron

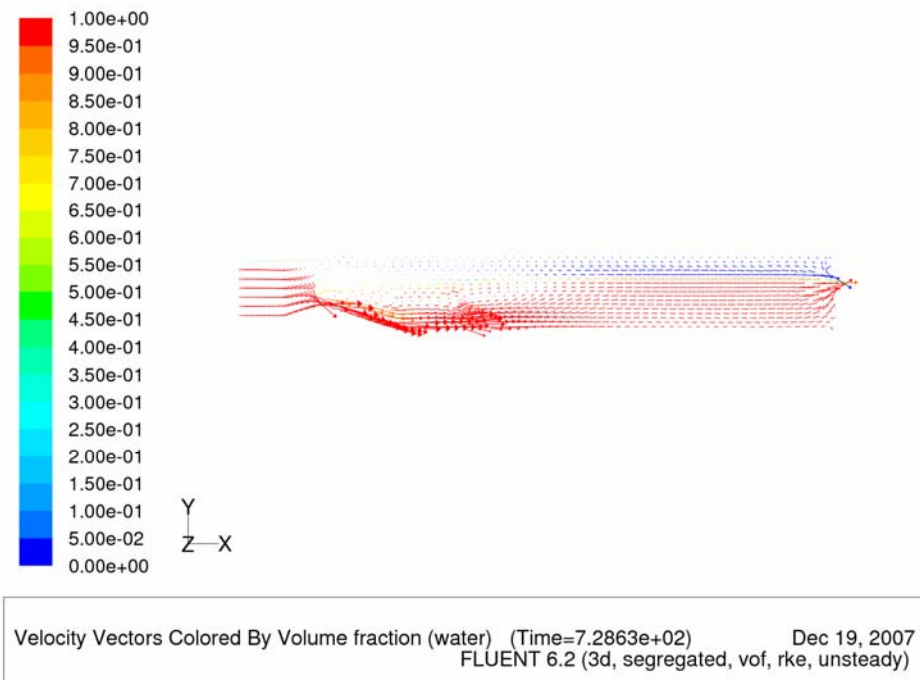


Fig. 5.21 Velocity Vectors for Controlled Submerged Jump in Barrage with Horizontal Flexible Apron

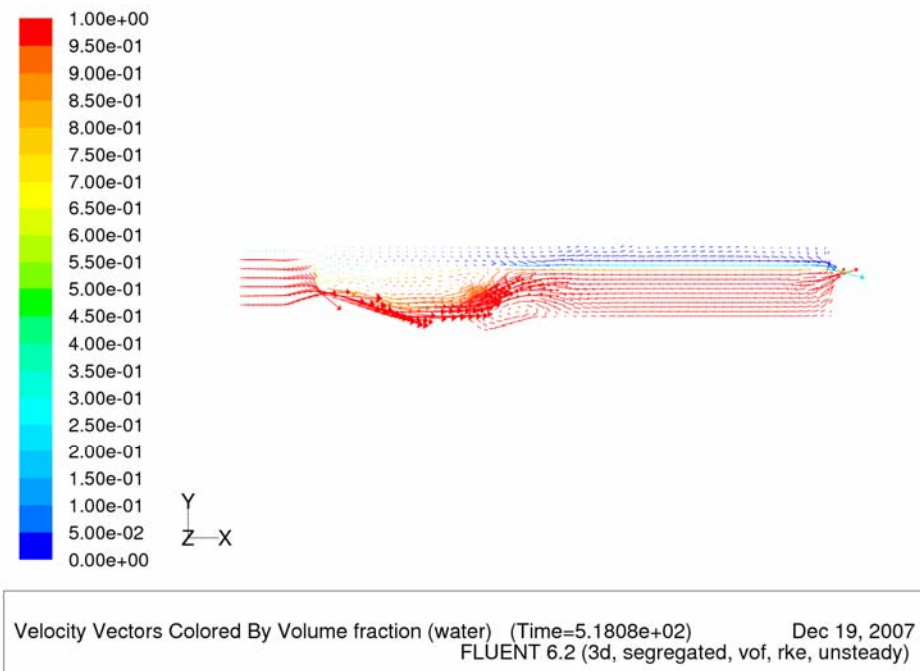


Fig. 5.22 Velocity Vectors for Controlled Submerged Jump in Barrage with Inclined Flexible Apron

## CHAPTER 6

### **FLOW MODELLING SOFTWARE**

#### **6.1 Two-dimensional numerical flow simulation model**

A two-dimensional flow model is based upon the solution of the two-dimensional shallow water equations (Cunge et al. 1980) was developed as a part of this report. This computer code, based upon the Finite Volume numerical scheme, is capable of simulating many free surface flow problems in hydraulic engineering, such as flows in rivers and open channels, flood wave propagation, dam-break event, hydraulic jump etc. here we discuss one such model, TINFLOW2D, which satisfy most of the above conditions are developed to solve the two-dimensional shallow water equations and the solution scheme for each is based upon cell-centred finite volume method. TINFLOW2D is implemented on unstructured triangular grids. The unstructured grid description is preferred because of its advantages over structured grids (Bates et al. 1996; Aronica et al. 1999). TINFLOW2D model is also devised to deal with drying and wetting phenomena so that the model can simulate flows over an initially dry bed. The model is capable of simulating the flow pattern in the pond behind a barrage, given the different flow conditions like the incoming discharge and the pond water level and outflows through gate.

#### **6.2 Governing equations**

Open channel flows may be described by three conservation laws – mass, momentum and energy. The flow variables are the flow depth and velocities or discharges in the three directions which are sufficient to define the flow conditions within a domain. Thus for the two-dimensional flow where the velocity (or discharge) in the vertical direction is neglected three equations may be used to analyse a typical flow situation. The continuity and momentum or energy equations in two directions are used for this purpose. If the flow is discontinuous such as for a jump or a bore momentum equations are the only choice (Cunge et al. 1980). These equations can be obtained by integrating the Navier-Stokes equations over the flow depth. The assumptions made in the process are: incompressible fluid, uniform velocity distribution in the vertical direction, hydrostatic pressure distribution and



small bottom slope. The governing equations based on the above assumptions are known as the shallow water equations.

Neglecting diffusion of momentum due to viscosity and turbulence, wind effects and the Coriolis term, two-dimensional shallow water equations in conservation form may be expressed as (Cunge et al. 1980):

$$\frac{\partial \mathbf{U}}{\partial t} + \nabla \cdot (\mathbf{E}, \mathbf{G}) = \mathbf{S} \quad (6.1)$$

in which

$$\mathbf{U} = \begin{pmatrix} H \\ hu \\ hv \end{pmatrix}, \mathbf{G} = \begin{pmatrix} hv \\ huv \\ hv^2 + \frac{1}{2}gh^2 \end{pmatrix}, \mathbf{E} = \begin{pmatrix} hu \\ hu^2 + \frac{1}{2}gh^2 \\ huv \end{pmatrix}, \mathbf{S} = \begin{pmatrix} 0 \\ gh(S_{0x} - S_{fx}) \\ gh(S_{0y} - S_{fy}) \end{pmatrix} \quad (6.2)$$

where  $\mathbf{U}$  represents the vector of conserved variables,  $\mathbf{E}$  and  $\mathbf{G}$  are the convective fluxes in the  $x$ - and  $y$ -directions, respectively and  $\mathbf{S}$  represents the source terms involving bed slope and friction. In addition,  $H$  is the water level defined above a datum,  $h$  is the depth of water measured from bed,  $u$  and  $v$  are the two vertically averaged velocity components in the horizontal plane along the  $x$ - and  $y$ - directions respectively and  $g$  is the acceleration due to gravity. Here, water level ( $H$ ) is considered as one of the unknown variables instead of water depth ( $h$ ) due to the fact that reconstruction of  $h$  for higher-order spatial accuracy from the cell average values will not guarantee a continuous reconstruction at the cell boundaries if the bed slope varies from cell to cell (Nujic 1995; Zhou et al. 2001).

Indicating the bottom elevation with  $z$ , the bed slopes in the  $x$ - and  $y$ -directions are given as  $S_{0x} = -\partial z / \partial x$  and  $S_{0y} = -\partial z / \partial y$ , respectively and  $S_{fx}$ ,  $S_{fy}$  are the friction slopes in the respective directions, which are estimated by the empirical relationships of the Manning form (Fennema and Chaudhry 1990; Chaudhry 1994; Zhao et al. 1994; Berger and Stockstill 1995) as given below.

$$S_{fx} = \frac{n^2 u \sqrt{u^2 + v^2}}{h^{4/3}}; \quad S_{fy} = \frac{n^2 v \sqrt{u^2 + v^2}}{h^{4/3}} \quad (6.3)$$

where  $n$  is the Manning's roughness coefficient.

### 6.3 Numerical Scheme

The governing equations for shallow water flow model as given in Eq. (6.1) are a set of nonlinear, hyperbolic partial differential equations that makes difficult finding the solutions to these equations. Hyperbolic equations admit discontinuous and smooth solutions. Even for smooth initial conditions, the non-linear character combined with hyperbolic nature of the equations can lead to discontinuous solutions in finite time. It is the nonlinear character of the equations that limits the analytical solutions to only very special cases. Therefore, these equations are solved with aid of numerical methods. Research on numerical methods of solution to two-dimensional shallow water equations has received considerable attention over the past two decades. Several techniques have been developed to solve the equations and these include: the method of characteristics (Katopodes and Strelkoff 1978); the finite difference method, FDM (Fennema and Chaudhry 1990; Molls and Chaudhry 1995); the finite-element method, FEM (Katopodes 1984; Chaudhry 1994; Tucciarelli and Termini 2000); and the finite volume method, FVM (Alcrudo and García-Navarro 1993; Zhao et al. 1996; Anastasiou and Chan 1997).

The method of characteristic has the capability of preserving directional information, but it is difficult to find solution for two or more dimensions. In the presence of shocks or jumps, this method fails to produce valid results. The finite difference method is simpler to implement even for two-dimensional flow. This method can be developed based on explicit and implicit schemes. Explicit schemes are relatively easy compared to implicit schemes. However, explicit methods have to satisfy Courant-Friedrichs-Lewy (CFL) condition for numerical stability and therefore these classes of methods suffer from small computational time steps. On the other hand, implicit schemes are generally unconditionally stable and they allow using large time steps and therefore suitable for long time simulations. Of course, implicit schemes involve solution of a set of algebraic equations in the form of a matrix and therefore, result in large number of calculations. Finite difference methods have been used with structured grids but may confront difficulties in handling irregular boundaries. In such a case grid transformation is preferred (Nagata et al. 2000; Molls and Chaudhry 1995). Finite element methods can handle irregular boundaries but they are computationally intensive and more difficult to implement than finite difference schemes. Finite volume methods have advantages over the other methods as discussed by Tan (1992) and Zhao et al. (1994).

Briefly, FVM has the following merits: (1) FVM can be considered as a special case of FDM and can also be easily implemented in arbitrary coordinates. Thus, the method combines the simplicity of FDM with the geometric flexibility of FEM; (2) generally, FVM takes less computational effort than FEM; (3) FVM is based on the integral form of the conservation laws, thus a scheme in conservation form can easily be constructed to capture shock waves; (4) by discretisation of integral form of the conservation equations, mass and momentum remain conserved (Hirsch 1988, p. 237); (5) FVM allows the treatment of a two-dimensional problem as a series of local one-dimensional problems, resulting in a simple but accurate and computationally efficient algorithm. Therefore, a finite volume method on unstructured triangular as well as quadrilateral grids is used in this study to solve the two-dimensional shallow water equations. A complex flow domain can easily be covered by unstructured grids especially by triangular grids. An advantage of using triangular grids is that the grids can be easily developed for irregular flow domains and the number of cells can be increased in high gradient regions or in regions of particular interest. This advantage is also quite true for unstructured quadrilateral grids as well. Moreover, there are a number of grid generators (Triangle; Easymesh, GEN4U) which are readily available on-line.

Finite volume method may be classified as cell-centred or vertex-centred methods. In this study a cell-centred method based on Godunov-type scheme is applied for solving the shallow water equations. Details of the finite volume scheme for two-dimensional shallow water equations are presented below.

## 6.4 Finite Volume Method

As described in the previous section, a cell-centred finite volume method is applied in this study to solve the two-dimensional shallow water equations. The scheme is suitable for irregular flow domains and easy to implement. The proposed finite volume method is an implicit scheme and second-order accurate in space. The flow domain is discretised into a grid of control volumes which, in the present work, is considered in the form of an unstructured triangular or quadrilateral mesh. Each segment making up the outer boundary of a control volume in plan is referred to as an edge and the vertical plane over an edge is called a face though they hold synonymous meanings under certain contexts. A cell-centred

finite volume algorithm is formulated for Eq. (6.1) over each control volume and the integral form of the system of two-dimensional shallow water equations can be written as

$$\int_{\Omega} \frac{\partial \mathbf{U}}{\partial t} d\Omega + \int_{\Omega} \nabla \cdot (\mathbf{E}, \mathbf{G}) d\Omega = \int_{\Omega} \mathbf{S} d\Omega \quad (6.4)$$

In the two-dimensional approach adopted in this work, the spatial domain is covered by a set of triangular or quadrilateral cells (Fig. 6.1), not necessarily aligned with the co-ordinate directions. A discrete approximation to Eq. (4) is applied in every cell  $\Omega$  so that the first term represents the integral of time evolution of the function over the area with the dependent variables represented as piecewise constants within the cell and the surface integral in the second term represents the total flux through the boundaries. Applying Gauss divergence theorem to the second integral, Eq. (6.4) reduces to the following equation:

$$A \frac{\partial \mathbf{U}}{\partial t} + \oint_{\Gamma} (\mathbf{E} n_x + \mathbf{G} n_y) d\Gamma = A \mathbf{S} \quad (6.5)$$

where  $\Gamma$  is the boundary of the area  $A$ ,  $\Omega$  is a fixed volume and;  $n_x$  and  $n_y$  are the components of unit normal in the  $x$ - and  $y$ -directions, respectively. The contour integral is approached via a mid-point rule, i.e. a numerical flux is defined at the mid-point of each edge, giving

$$\oint_{\Gamma} (\mathbf{E} n_x + \mathbf{G} n_y) d\Gamma = \sum_{m=1}^N \mathbf{F}_m^* \cdot \mathbf{n}_m d\Gamma_m \quad (6.6)$$

where  $N$  is the total number of edges in the cell. If triangular cell is considered,  $N = 3$  and for quadrilateral cells,  $N = 4$ .  $\mathbf{F}_m^*$  is the numerical flux vector through the edge  $m$  whose unit outward normal vector is given as  $\mathbf{n}_m$ . In Eq. (6.6) an estimate of the normal outward flux ( $\mathbf{F}_m^*$ ) is required to be computed. The problem thus reduces to the solution of a series of local one-dimensional problems normal to the cell interfaces where  $\mathbf{U}_L$  and  $\mathbf{U}_R$  are the states in the two neighbouring cells of each interface. Recalling that  $\mathbf{U}$  is assumed to be piecewise constant within each cell this will usually result in a discontinuity across the cell edge common to two cells. Local initial value problems that involve discontinuous neighbouring states are known as the Riemann problem.

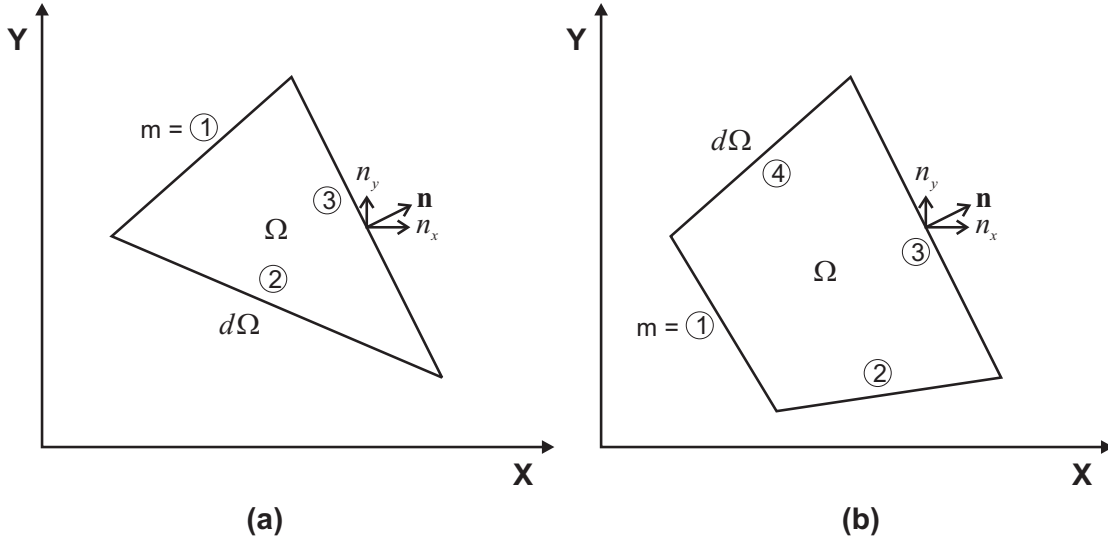


**Fig. 6.1:** Details of a computational cell (finite volume  $\Omega$  and surface surrounding the volume  $d\Omega$ ): (a) Triangular cell and (b) Quadrilateral cell

The Godunov scheme is one of the most successful approaches that has been developed for solving such Riemann problems. These schemes are robust and accurately capture the location of discontinuities such as shocks and bores. Two dimensional Riemann solvers do not appear to have matured enough to be used in the construction of multi-dimensional schemes (Billett and Toro 1997). Thus the explicit expression of  $\mathbf{F}^*$  depends upon the selected Riemann solver (Roe 1981 and 1986; Alcrudo et al. 1992; Zhao et al. 1994 and 1996; Nujic 1995; Anastasiou and Chan 1997; Valiani et al. 2002).

#### 6.4.1 Roe's Approximate Riemann Solver

The cell interface Riemann problem can be solved in an exact manner but often requires the solution of a set of nonlinear algebraic equations, which can be computationally very expensive. Moreover, the higher-order accuracy obtained from the exact solution is lost due to the cell averaging at the end of the flux calculation, since conservative variables are only represented as averages within cell volumes. Thus a number of approximate Riemann solvers have been developed over the years to solve the Riemann problem and Roe's approximate Riemann solver (Roe 1981) is one of them which have been widely used. In this study the one-dimensional Riemann problem at cell interface is solved using Roe's approximation,

which was initially introduced for the compressible Euler equations. The shallow water system of equations is similar to the Euler system of equations that describes inviscid compressible flow in gas dynamics. Compressibility in gas flows is equivalent to free surface deformability of free surface flows and Mach number is equivalent to Froude number. These similar properties form the basis of using the same numerical technique to solve the system of shallow water equations.

Roe's Riemann solver is termed as flux difference splitting (FDS) scheme for the Euler system of equations. This scheme was probably applied to the system of shallow water equations for the first time by Glaister (1988). In Roe's approximation, the nonlinear problem is linearised (Appendix C.3) at the cell interface. At each cell interface, we have a discontinuity with  $\mathbf{U}_L$  and  $\mathbf{U}_R$  being the states on the left and right of the cell and using the Roe's scheme the numerical flux across the cell interface can be written as

$$\mathbf{F}^* = \frac{1}{2} \left[ \mathbf{F}_R + \mathbf{F}_L - |\tilde{\mathbf{A}}_{RL}| (\mathbf{U}_R - \mathbf{U}_L) \right] \quad (6.7)$$

where  $\mathbf{F}_{R/L}$  are the flux vectors on the right and left sides of an interface, and  $\tilde{\mathbf{A}}_{RL}$  is the approximated flux Jacobian. Eq. (6.7) can also be expressed in the following form (Hubbard 1999)

$$\mathbf{F}^* = \frac{1}{2} \left[ \mathbf{F}_R + \mathbf{F}_L - \sum_{k=1}^3 \tilde{\alpha}^k |\tilde{\lambda}^k| \tilde{\mathbf{e}}^k \right] \quad (6.8)$$

where  $\{\tilde{\lambda}^k, k=1,3\}$  and  $\{\tilde{\mathbf{e}}^k, k=1,3\}$  are the eigenvalues and eigenvectors of the approximate Jacobian  $\tilde{\mathbf{A}}_{RL}$ :

$$\tilde{\lambda}^1 = \tilde{u}n_x + \tilde{v}n_y + \tilde{c}, \quad \tilde{\lambda}^2 = \tilde{u}n_x + \tilde{v}n_y, \quad \tilde{\lambda}^3 = \tilde{u}n_x + \tilde{v}n_y - \tilde{c} \quad (6.9)$$

$$\tilde{\mathbf{e}}^1 = \begin{pmatrix} 1 \\ \tilde{u} + \tilde{c}n_x \\ \tilde{v} + \tilde{c}n_y \end{pmatrix}, \quad \tilde{\mathbf{e}}^2 = \begin{pmatrix} 0 \\ -\tilde{c}n_y \\ \tilde{c}n_x \end{pmatrix}, \quad \tilde{\mathbf{e}}^3 = \begin{pmatrix} 1 \\ \tilde{u} - \tilde{c}n_x \\ \tilde{v} - \tilde{c}n_y \end{pmatrix} \quad (6.10)$$

and the corresponding wave strengths  $\{\tilde{\alpha}^k, k=1,3\}$  are defined as

$$\alpha^{1,3} = \frac{\Delta h}{2} \pm \frac{1}{2\tilde{c}} \left[ \Delta(hu)n_x + \Delta(hv)n_y - (\tilde{u}n_x + \tilde{v}n_y)\Delta h \right] \quad (6.11)$$

$$\alpha^2 = \frac{1}{\tilde{c}} \left[ \{ \Delta(hv) - \tilde{v} \Delta h \} n_x - \{ \Delta(hu) - \tilde{u} \Delta h \} n_y \right] \quad (6.12)$$

where  $\Delta(\cdot) = (\cdot)_R - (\cdot)_L$ .

The Roe averages are defined as

$$\tilde{u} = \frac{u_R \sqrt{h_R} + u_L \sqrt{h_L}}{\sqrt{h_R} + \sqrt{h_L}}, \quad \tilde{v} = \frac{v_R \sqrt{h_R} + v_L \sqrt{h_L}}{\sqrt{h_R} + \sqrt{h_L}}, \quad \tilde{c} = \sqrt{\frac{g}{2} (h_R + h_L)} \quad (6.13)$$

### 6.4.2 Entropy Correction

One of the main drawbacks of Roe solver is that it does not satisfy the entropy condition at critical points and shows unphysical jump. To avoid this problem, it is necessary to modify the flux computation near the points where an eigenvalue is close to zero. This can be achieved by modifying the eigenvalue  $|\lambda|$  in Eq. (8). The entropy correction suggested by Harten and Hyman (1983) or Alcrudo et al. (1992) is applied in the present study depending upon the flow problems.

If the intermediate states,  $\mathbf{U}_L$  and  $\mathbf{U}_R$  are defined as the cell-centred values, a first-order accurate scheme is obtained, which suffers from excess numerical dissipation and accuracy is undermined. A more accurate method can be obtained by choosing better values for the left and right states by adopting higher-order methods.

### 6.5 Higher-order Scheme

Although first-order schemes provide sufficient information for engineering purposes, their accuracy is greatly undermined due to excessive numerical dissipation. An approach to reduce numerical dissipation is the development of a reconstruction procedure for the variables inside each cell requiring the evaluation of gradients of the variables considering neighbourhood values and eventually leading to the development of higher-order schemes (Anastasiou and Chan 1997; Sleigh et al. 1998; Hubbard 1999; Wang and Liu 2000; Yoon and Kang 2004). The higher-order schemes based on the extension of one-dimensional MUSCL approach to unstructured grids make the schemes strongly dependent on grid

connectivity (Barth and Jespersen 1989; Jawahar and Kamath 2000; Yoon and Kang 2004) and therefore poor results are obtained when the grids are distorted. In the present study, a multi-dimensional gradient-reconstruction technique proposed by Jawahar and Kamath (2000), which includes a wide computational stencil (Fig. 6.2a) and does not strongly depend on vertex values, is employed for triangular grids and the same technique is modified and extended for quadrilateral grids.

On unstructured meshes, it is difficult to obtain reconstructions of order higher than second using existing procedures, and even second-order development with low grid sensitivity is not straightforward. Therefore, a second-order reconstruction is carried out for the variables. This is achieved by means of a linear reconstruction of the variables within a cell, as

$$\mathbf{U}_i^{\text{new}} = \mathbf{U}_i + \mathbf{r}_i \cdot \nabla \mathbf{U}_i^l \quad (14)$$

where  $\mathbf{r}_i$  is the position vector relative to the centroid of the cell  $i$  and  $\nabla \mathbf{U}_i^l$  is the limited gradient, and  $\mathbf{U}_i$  and  $\mathbf{U}_i^{\text{new}}$  are the variable vectors before and after reconstruction, respectively. Thus a second-order scheme requires evaluation of gradients and some kind of limiting procedure. Limiting is necessary in order to suppress oscillations which is common for higher-order extensions of the basic linear algorithm.

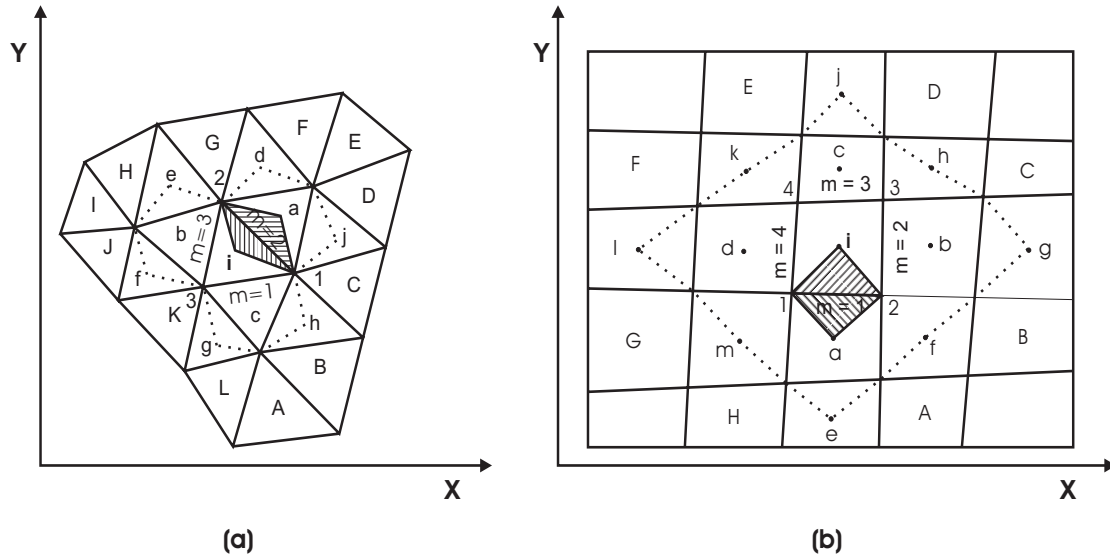


**Fig. 6.2:** Stencil used for gradient reconstructions: (a) Triangular grid and (b) Quadrilateral grid



### 6.5.1 Gradient Reconstruction

It is well known that a gradient plane is uniquely defined by three non-collinear points. Thus the reconstruction technique proposed by Jawahar and Kamath (2000) computes gradients based on the two vertices (end points of an interface) and a cell centre (on either side of an interface) by looping over all the interfaces of a cell. Thus a sub-cell can be imagined by joining two vertices and a cell centre and area-weighted average of the gradients of sub-cells on either side of an interface are used to calculate the face gradients. Again, the area-weighted average of the face gradients gives the unlimited gradients for the variables of a cell and this unlimited gradient is moderated by the use of a function called the limiter.

The gradients of  $\mathbf{U}$  for a sub-cell can be estimated by applying the Green-Gauss theorem as

$$\nabla \mathbf{U} = \frac{1}{A} \oint_{\Gamma} \mathbf{U} n d\Gamma \quad (6.15)$$

where  $\Gamma$  is the integration path connecting the vertices of the sub-cell and  $A$  is the area of the sub-cell. In the above derivation, the values of conserved variables are desired at the cell vertices and, since they are never explicitly evaluated, are calculated on the basis of the pseudo-Laplacian formula (Appendix E) proposed by Holmes and Connell (1989). The conserved variable at a vertex  $cv$  is given by

$$\mathbf{U}_{cv} = \sum_{j=1}^{nc} \frac{\omega_j}{\sum_{j=1}^{nc} \omega_j} \mathbf{U}_j \quad (6.16)$$

where  $nc$  denotes the cells surround the vertex  $cv$ . The weight  $\omega_j$  corresponding to a surrounding cell  $j$  is calculated as follows

$$\omega_j = 1 + \lambda_x (x_j - x_{cv}) + \lambda_y (y_j - y_{cv}) \quad (6.17)$$

$$\lambda_x = \frac{I_{xy} R_y - I_{yy} R_x}{I_{xx} I_{yy} - I_{xy}^2}, \quad \lambda_y = \frac{I_{xy} R_x - I_{xx} R_y}{I_{xx} I_{yy} - I_{xy}^2}$$

$$(18) I_{xx} = \sum_{j=1}^{nc} (x_j - x_{cv})^2, \quad I_{yy} = \sum_{j=1}^{nc} (y_j - y_{cv})^2, \quad I_{xy} = \sum_{j=1}^{nc} (x_j - x_{cv})(y_j - y_{cv}) \quad (19)$$

$$R_x = \sum_{j=1}^{nc} (x_j - x_{cv}), \quad R_y = \sum_{j=1}^{nc} (y_j - y_{cv}) \quad (6.20)$$

The cells at boundaries suffer from one-sided triangulation which yields unrealistic values of weights that are either zero or negative. These unrealistic values are modified by assigning unity for the weights if they all vanish. If any value becomes negative its absolute value is taken for simplicity and no weight is allowed to exceed unity. This simple modification is seen to work well.

The gradient at any face, say  $m=1$  (Fig. 6.2a), is computed using the area-weighted average of the gradients of the two sub-cells  $\Delta i2$  and  $\Delta 1a2$  formed by the edge and the centroids of the connected cells and having areas  $A_{i2}$  and  $A_{1a2}$ , in the following manner

$$(\nabla \mathbf{U})_{m=1} = \frac{[A_{i2}(\nabla \mathbf{U})_{i2} + A_{1a2}(\nabla \mathbf{U})_{1a2}]}{[A_{i2} + A_{1a2}]} \quad (6.21)$$

In the same way, the other face gradients  $(\nabla \mathbf{U})_{m=2}$  and  $(\nabla \mathbf{U})_{m=3}$  of cell  $i$  are computed considering the respective neighbouring cells  $b$  and  $c$ .

The unlimited gradient  $(\nabla \mathbf{U}_i)$  for a triangular cell  $i$  is then constructed using the area-weighted average of the corresponding face gradients given by

$$\nabla \mathbf{U}_i = \frac{[A_{i1a2}(\nabla \mathbf{U})_{m=1} + A_{i2b3}(\nabla \mathbf{U})_{m=2} + A_{i3c1}(\nabla \mathbf{U})_{m=3}]}{[A_{i1a2} + A_{i2b3} + A_{i3c1}]} \quad (6.22)$$

In the above expression, each of the areas ( $A_{i1a2}$ ,  $A_{i2b3}$ ,  $A_{i3c1}$ ) is defined over the respective edge by the trapezoidal area joining the two ends of the edge and the two centroids of the triangular cells connected to the edge. For example, in Fig. 6.2(a), the area  $A_{i1a2}$  is the trapezoidal area for face  $m=1$  (edge 1-2) and is formed by joining the points  $i-1-a-2$ .

## 6.5.2 Multidimensional Limiter

Unfortunately, the higher-order schemes are not free from non-physical oscillations in the presence of shocks which are suppressed by limiting the cell-centred gradients of the variables. The use of continuously differentiable multidimensional limiter developed by Jawahar and Kamath (2000) produces a smooth transition between discontinuous jumps and

therefore adopted for triangular grids. A similar kind of multi-dimensional limiter is proposed for quadrilateral grids. Brief descriptions of the limiters for two different types of grids are presented below.

For a two-dimensional triangular unstructured grid, the limited gradient within a cell  $i$  can be obtained by taking the weighted average of three representative gradients of the surrounding cells  $a$ ,  $b$  and  $c$  as (Fig. 3.2a)

$$\nabla \mathbf{U}_i^l = \omega_a \nabla \mathbf{U}_a + \omega_b \nabla \mathbf{U}_b + \omega_c \nabla \mathbf{U}_c \quad (6.23)$$

where  $\omega_a$ ,  $\omega_b$  and  $\omega_c$  are the weights given by the multidimensional limiter function (Jawahar and Kamath 2000) and  $\nabla \mathbf{U}_a$ ,  $\nabla \mathbf{U}_b$  and  $\nabla \mathbf{U}_c$  are the unlimited gradients of the three surrounding cells  $a$ ,  $b$  and  $c$  which are combined to produce the limited gradient  $\nabla \mathbf{U}_i^l$ . The weights are defined as follows, according to the reference cited

$$\omega_a = \frac{(g_b g_c + \varepsilon^2)}{(g_a^2 + g_b^2 + g_c^2 + 3\varepsilon^2)} \quad (6.24)$$

$$\omega_b = \frac{(g_c g_a + \varepsilon^2)}{(g_a^2 + g_b^2 + g_c^2 + 3\varepsilon^2)} \quad (6.25)$$

$$\omega_c = \frac{(g_a g_b + \varepsilon^2)}{(g_a^2 + g_b^2 + g_c^2 + 3\varepsilon^2)} \quad (6.26)$$

where  $g_a$ ,  $g_b$  and  $g_c$  are functions of the gradients of the surrounding cells and can be chosen as the square of the  $L_2$  norm, i.e.,  $g_a = \|\nabla \mathbf{U}_a\|_2^2$ ,  $g_b = \|\nabla \mathbf{U}_b\|_2^2$ , and  $g_c = \|\nabla \mathbf{U}_c\|_2^2$ ; and  $\varepsilon$  is a small number which is introduced to prevent indeterminacy caused by the vanishing of the three gradients in regions of uniform flow.

After computing the unlimited gradients using Eq. (6.22), the limited gradients are calculated with the help of Eq. (6.23).

## 6.6 Source Terms

The simulation of shallow water flow in a real world situation demands a suitable numerical treatment for an irregular bottom topography that determines the bottom slope source term and the bed shear stress which is evaluated as friction slope source term. The discretisation of the source terms for finite volume shallow water flow models has been the subject of numerous recent studies (Bermúdez and Vázquez-Cendón 1994; Nujic 1995; Vázquez-Cendón 1999; Delis et al. 2000; García-Navarro and Vázquez-Cendón 2000; Hubbard and García-Navarro 2000; Burguete and García-Navarro 2001; Sanders 2001, Zhou et al. 2001, Bradford and Sanders 2002; Komaei 2004; Valiani and Begnudelli 2006). In this work, the bed slope source term is treated in a simple way which also satisfies a compatibility relation with the hydrostatic flux term. The proposed technique is explained below in detail for triangular cell and the same idea is extended to a quadrilateral cell. The friction slope source term is determined by the usual quadratic friction law [Eq. (6.3)] .

### 6.6.1 Bed Slope Source Term

The treatment of bed slope source terms for triangular and quadrilateral grids are discussed below in two separate sections.

#### 6.6.1.1 Bed Slope Source Term for Triangular Cell

The bed slope source term has the following form

$$\mathbf{S}_0 = \begin{bmatrix} 0 \\ ghS_{0x} \\ ghS_{0y} \end{bmatrix} \quad (6.27)$$

The numerical treatment of  $\mathbf{S}_0$  for a triangular cell can easily be done by considering a linear bottom plane and calculating its slopes in the  $x$ - and  $y$ -directions on the horizontal plane. But this treatment to the bed slope term must satisfy certain compatibility relations with the hydrostatic flux term so that still water condition is satisfied as explained below.

The water surface slope for flow taking place over a domain of uneven and rough bed would be inclined, in general. As the velocity approaches zero, the water surface tends to

horizontal. Simultaneously, the friction slope source term and the momentum flux approach zero as both are functions of velocity. In the limit, when the flow is zero, the water surface becomes horizontal. Only the pressure force on the cell faces and the weight of the water contained within each cell remain, and they should exactly balance each other to satisfy the still water condition. That is, in the absence of flows through the boundaries, the momentum equations in  $x$ - and  $y$ -directions reduce to

$$\oint_{\Gamma} \left( \frac{1}{2} g h^2 \right) n_x d\Gamma = g \int_{\Omega} h S_{ox} d\Omega \quad (6.28)$$

$$\oint_{\Gamma} \left( \frac{1}{2} g h^2 \right) n_y d\Gamma = g \int_{\Omega} h S_{oy} d\Omega \quad (6.29)$$

This indicates that the sum of the hydrostatic pressure forces on the vertical faces of a cell in a particular direction is numerically equal to the weight component of the water contained within the cell in the same direction.

Two developments based on this concept may be cited, which are important from the point of view of flow modelling by the finite volume method. Valiani and Begnudelli (2006) use this idea to evaluate the bed slope source term which is rather difficult to evaluate for an  $n$ -faced cell, where  $n$  is larger than three. Komaei (2004), too, utilizes this concept in a flow model where the water surface is considered horizontal, that is, first-order accurate. Both the developments are important but each appears to be incomplete to a certain extent (Kuiry et al. 2006). In the first reference, though the use of the concept is fine, the evaluation of the pressure term as suggested by the writers could be improved by adopting the method proposed by Komaei and Bechteler (2004). As for the second reference itself, the proposed model may be improved by considering a second-order accurate water surface variation while computing the hydrostatic pressure forces on the cell faces.

The following sections describe evaluation of the two terms, the weight of water prism and the hydrostatic pressure force, for a triangular cell that satisfies Eqs. (6.28) and (6.29) under still water condition.

### Weight of water prism

Consider a triangular cell with a sloped bottom and an inclined water surface as in Fig. 6.3(a). The numerical integration of the right hand sides of Eqs. (6.28) and (29) after multiplication with water density,  $\rho$ , gives the weight component of the water prism along the coordinate axes  $x$ - and  $y$ - as

$$W_{x,y} = \rho g \int_{\Omega} h S_{0x,y} d\Omega = W_{\Omega} S_{0x,y} \quad (6.30)$$

The weight of the water prism ( $W_{\Omega}$ ) may be computed by the following expression

$$W_{\Omega} = \gamma A h_c = \gamma A (h_1 + h_2 + h_3)/3 \quad (6.31)$$

where  $h_1$ ,  $h_2$  and  $h_3$  are the water depths at the three vertices of the triangular cell. These are obtained by a second-order reconstruction of the water surface at the cell vertices

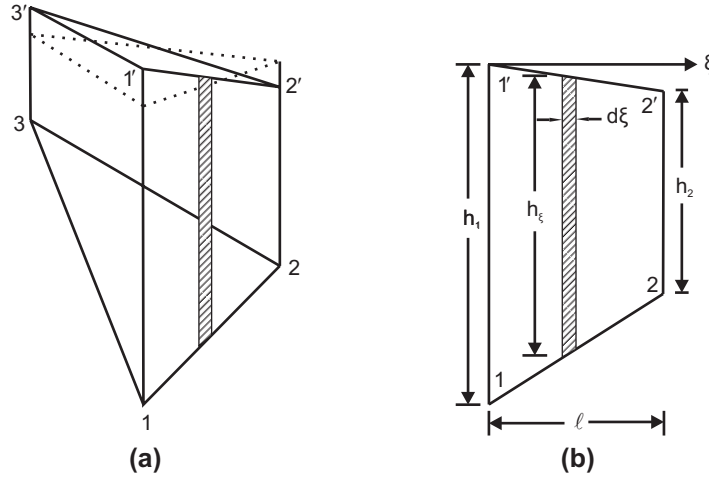


**Fig. 6.3:** (a) Water prism with inclined water surface and sloped triangular base;  
(b) One face of the water prism

$(H_k, k=1,3)$  as described before and deducting the corresponding vertex elevations  $(z_k, k=1,3)$  of the cell bottom.

In order to calculate the weight component of the water prism, the general equation of the triangular cell base is evaluated as

$$z = c_1 x + c_2 y + c_3 \quad (6.32)$$

where the coefficients  $c_1$ ,  $c_2$  and  $c_3$  are constants and may be derived by substituting vertex coordinates into Eq. (32) and solving the simultaneous equations. The bottom slope along the two co-ordinate directions may then be defined as

$$S_{ox} = -\frac{\partial z}{\partial x} = -c_1 = -\frac{1}{2A} \left[ (y_2 - y_3)z_1 + (y_3 - y_1)z_2 + (y_1 - y_2)z_3 \right] \quad (6.33)$$

$$S_{oy} = -\frac{\partial z}{\partial y} = -c_2 = -\frac{1}{2A} \left[ (x_3 - x_2)z_1 + (x_1 - x_3)z_2 + (x_2 - x_1)z_3 \right] \quad (6.34)$$

where,  $2A = x_1y_2 + x_2y_3 + x_3y_1 - y_1x_2 - y_2x_3 - y_3x_1$ ;  $(x_k, y_k, k=1,3)$  are the  $x$ - and  $y$ -coordinates of the respective vertices and  $A$  is the projected area of the triangular base onto the horizontal plane.

The bed elevations  $(z_k, k=1,3)$  of the three vertices of the triangular cell are then replaced back in Eqs. (33) and (34); and the weight of the water prism in the  $x$ -direction ( $W_x$ ) is obtained as

$$\begin{aligned} W_x &= \rho \left[ g \int_{\Omega} h S_{ox} d\Omega \right] \\ &= \frac{\gamma h_c}{6} \left[ (y_2 - y_3)h_1 + (y_3 - y_1)h_2 + (y_1 - y_2)h_3 - \Delta w_x \right] \end{aligned} \quad (6.35)$$

Similarly, the weight component in the  $y$ -direction ( $W_y$ ) is found out to be

$$W_y = \frac{\gamma h_c}{6} \left[ (x_3 - x_2)h_1 + (x_1 - x_3)h_2 + (x_2 - x_1)h_3 - \Delta w_y \right] \quad (6.36)$$

In Eqs. (35) and (36), the terms  $\Delta w_x$  and  $\Delta w_y$  appear due to second-order spatial variation of water surface within a cell and are defined as

$$\Delta w_x = \left[ (y_2 - y_3)H_1 + (y_3 - y_1)H_2 + (y_1 - y_2)H_3 \right] \quad (6.37)$$

$$\Delta w_y = \left[ (x_3 - x_2)H_1 + (x_1 - x_3)H_2 + (x_2 - x_1)H_3 \right] \quad (6.38)$$

### **Hydrostatic force**

For the water prism shown in Fig. 6.3(a), contained between the inclined water surface and the sloped triangular base, a typical vertical face  $1-2-2'-1'$  is depicted in Fig. 363(b). A vertical strip of infinitesimal width  $d\xi$  is also marked on the face for the derivation of the hydrostatic pressure force as given below.

$$f_{hyd} = \frac{1}{2} \gamma h_{\xi}^2 d\xi \quad (6.39)$$

where,  $f_{hyd}$  is the force due to hydrostatic pressure on the strip considered and  $\gamma = \rho g$  is the specific weight of water.

Integration of Eq. **Error! Reference source not found.** for the entire face results in an expression for the total hydrostatic force on the face as given below.

$$\frac{1}{2} \gamma \int_{\xi=0}^{\ell} h_{\xi}^2 d\xi = \frac{1}{2} \gamma \left[ \frac{h_1^2 + h_1 h_2 + h_2^2}{3} \right] \ell \quad (6.40)$$

where,  $\ell$  is the length of the considered edge in the horizontal plane and,  $h_1$  and  $h_2$  are the water depths at the vertices 1 and 2 computed as discussed in the previous section. The net hydrostatic force ( $F_{hyd}$ ) on a cell face of edge length  $\ell$  may be written as

$$F_{hyd} = \frac{1}{2} \gamma h_{eq}^2 \ell \quad (6.41)$$

where an equivalent depth of water ( $h_{eq}$ ) for the cell face is given by

$$h_{eq} = \sqrt{\frac{h_1^2 + h_1 h_2 + h_2^2}{3}} \quad (6.42)$$

After some algebraic manipulation, the net sum of the hydrostatic forces acting on the three faces of the water prism, along any direction, say the  $x$ -co-ordinate, is shown to be as follows



$$\begin{aligned}
(F_{hyd})_x &= \left( \oint \frac{1}{2} gh^2 \right) n_x d\Gamma \\
&= \sum_{m=1}^3 \left( \frac{1}{2} \gamma \int_{\xi=0}^{\ell} h_{\xi}^2 d\xi \right)_m n_{xm} \\
&= \frac{\gamma h_c}{6} [(y_2 - y_3)h_1 + (y_3 - y_1)h_2 + (y_1 - y_2)h_3]
\end{aligned} \tag{6.43}$$

Similar expression for the hydrostatic force component along the  $y$ -coordinate would be

$$(F_{hyd})_y = \frac{\gamma h_c}{6} [(x_3 - x_2)h_1 + (x_1 - x_3)h_2 + (x_2 - x_1)h_3] \tag{6.44}$$

where  $h_c = (h_1 + h_2 + h_3)/3$  is the depth of water at the centroid of the cell,  $(h_k, k=1,3)$  and  $(x_k, y_k, k=1,3)$  are the water depths and the  $x$ - and  $y$ -coordinates of the respective vertices.

Under still water condition, that is, when the velocity is zero and the water surface is horizontal, Eqs. (6.43) and (6.44) reduce exactly to those given by Eqs. (6.37) and (6.38).

#### 6.6.1.2 Bed Slope Source Term for Quadrilateral Cell

The bed slope source term for a quadrilateral cell may be treated by assuming that a quadrilateral cell is composed of two triangular sub-cells,  $\Delta 123$  and  $\Delta 134$ , as shown in Fig. 3.4 and similar treatment for each triangular cell can be applied as discussed in the previous section. Thus bed slope treatment for a quadrilateral cell is nothing but the treatment of two triangular sub-cells which form a quadrilateral cell (Kuiry and Sen 2006).

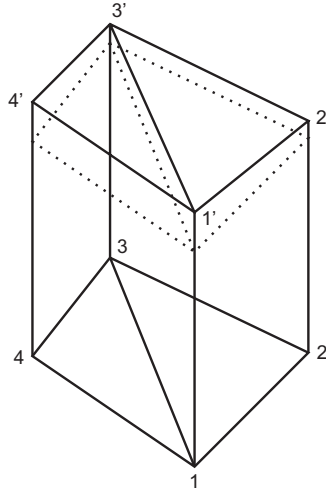


**Fig. 6.4:** A quadrilateral cell composed of two triangular sub-cells

## 6.6.2 Friction Slope Source Term

The so called friction slope of the source term has the following form

$$\mathbf{S}_f = \begin{bmatrix} 0 \\ -ghS_{fx} \\ -ghS_{fy} \end{bmatrix} \quad (6.45)$$

The above friction term is highly nonlinear and it may be a source of problematic convergence if treated explicitly. It has often been reported that an implicit or semi-implicit treatment of the friction term can solve many of these problems and improve the numerical stability (Beffa and Connell 2001; Valiani et al. 2002, Yoon and Kang 2004). Since in the present study, an implicit technique is used for solving the governing equations, as described later, no special treatment for the friction term is required.

## 6.7 Boundary Conditions

When a face of a cell coincides with the boundary of the flow domain or some physical boundary, it is necessary to solve a boundary Riemann problem (Sleigh et al. 1998; Yoon and Kang 2004). The theory of characteristics provides sufficient information to establish a relationship to find out the unknown variables at the boundary.

According to this theory, the Riemann invariants of one-dimensional shallow water equations are

$$R^- = u + 2c, \quad R^+ = u - 2c \quad (6.46)$$

Additionally, we have

$$\frac{d}{dt}(u - 2c) = 0 \quad \text{on} \quad \frac{dx}{dt} = u - c \quad (6.47)$$

$$\frac{d}{dt}(u + 2c) = 0 \quad \text{on} \quad \frac{dx}{dt} = u + c \quad (6.48)$$

Such that  $u \pm 2c$  are constant along  $u \pm c$  and  $c$  is the local wave speed given by  $c = \sqrt{gh}$ .

$R^-$  and  $R^+$  represent the states to the right and left of a face, respectively. According to the adopted convention of an anticlockwise traverse along cell edges to be considered as positive, the right side of a cell is on the outer side of a cell face. Naturally, since the right

side of a boundary face is outside the domain, the  $R^-$  relationship is replaced by the boundary condition itself. The  $R^-$  condition can be written as

$$u_L + 2c_L = u_* + 2c_* \quad (6.49)$$

where the subscripts  $L$  and  $*$  denote the variables at the left side and at the boundary, respectively.

Two types of boundaries are encountered in this study. These are: (i) the open boundary and (ii) the no-flow boundary. The boundary conditions used are the same as those used by Zhao et al. (1994) and Yoon and Kang (2004). Denoting  $\bar{u} = un_x + vn_y$  as the velocity in the outward normal direction to the cell face and  $\bar{v} = -un_y + vn_x$  as that parallel to the cell face in a local co-ordinate system centred at the mid-point of the cell face in question, the open and the wall boundary conditions are defined as described in the following sections.

### 6.7.1 Open Boundary

In this case,  $\mathbf{U}_L$  is the known state to the left of the boundary while  $\mathbf{U}_R = \mathbf{U}_*$  is the unknown solution to the right of the boundary. The variable  $\mathbf{U}_R$  has to be determined by selecting the outgoing characteristic relation according to the local flow regime and depending upon the type of physical boundary condition specified as under:

For a subcritical flow, three conditions may arise

1. When the depth of flow is specified at the boundary. Here,  $h_R$  is known, and  $u_R$  can be obtained from the following relation

$$u_R = u_L + 2\sqrt{g} \left( \sqrt{h_L} - \sqrt{h_R} \right) \quad (6.50)$$

2. When the discharge per unit width,  $q_R$  is given. In this case  $h_R$  and  $u_R$  can be solved from the relation  $q_R = h_R u_R$  and using Eq. (6.50). The substitution  $h_R = q_R / u_R$  in Eq. (6.50) yields a non-linear equation for  $h_R$  which can be solved by iteration such as the Newton-Raphson method.
3. When the rating curve, that is, a relationship between depth and unit discharge is known. The unknowns  $h_R$  and  $u_R$  can be solved from the relationship between the variables given by the rating curve and Eq. (6.50)..

The transverse velocity is assumed to be passively advected (Toro 1992), so  $v_R = v_L$ .

For a supercritical flow, only inflow boundary conditions such as depth of flow and unit discharge are specified. It is not necessary to specify outflow boundary conditions.

For a free outflow boundary, the boundary variables are same as the internal variables, that is, variables to the left of the boundary.

The above variables computed in local co-ordinate system are again transformed back to Cartesian system defined as  $u = \bar{u}n_x - \bar{v}n_y$  and  $v = \bar{u}n_y + \bar{v}n_x$ , respectively and used for calculating flux through the boundary.

### 6.7.2 No-flow Boundary

An interface between two cells is a wall boundary if there is no flow across that interface. The boundary condition specified, therefore, includes the normal velocity component being set as zero and  $h_R = h_L$  (Singh and Bhallamudi 1997). Then the normal flux is calculated simply as

$$\text{flux} = \left[ 0, \left( \frac{1}{2} gh_R^2 \right) n_x, \left( \frac{1}{2} gh_R^2 \right) n_y \right]^T \quad (6.51)$$

## 6.8 Time Discretisation

Time integration of Eq. (1) using the first-order Euler implicit time difference method can be obtained as

$$\left[ \frac{(AU)^{n+1} - (AU)^n}{\Delta t} \right] = - \left[ \theta \mathbf{R}(\mathbf{U}^{n+1}) + (1 - \theta) \mathbf{R}(\mathbf{U}^n) \right] \quad (6.52)$$

where  $\mathbf{R}$  is the convective terms and source terms as a whole,  $\Delta t$  is the size of time step and,  $\mathbf{U}^{n+1}$  and  $\mathbf{U}^n$  are the conserved variables at new and old time steps respectively and  $\theta$  is a time weighting factor. Newton's linearisation of Eq. (6.52) can be used about a known state  $\mathbf{U}^n$  to yield

$$\left[ \frac{\mathbf{I}A}{\Delta t} + \theta \frac{\partial \mathbf{R}(\mathbf{U}^s)}{\partial \mathbf{U}} \right] (\mathbf{U}^{s+1} - \mathbf{U}^s) = - \left[ \frac{(\mathbf{U}^s - \mathbf{U}^n)A}{\Delta t} + \theta \mathbf{R}(\mathbf{U}^s) + (1 - \theta) \mathbf{R}(\mathbf{U}^n) \right] \quad (6.53)$$

where  $\mathbf{I}$  is the identity matrix and  $s$  is a sub-iteration index. The terms associated with  $s$  are evaluated at an iteration level  $s$ .  $\Delta\mathbf{U} = \mathbf{U}^{s+1} - \mathbf{U}^s$  is the improvement in the assumed value of  $\mathbf{U}$  at iteration level  $s$ . Eq. (6.53) is evaluated for  $N$  unknown  $\Delta\mathbf{U}$  values for  $N$  unknown cells. Thus a system of linear algebraic equations for  $\Delta\mathbf{U}$  can be obtained by evaluating Eq. (6.53) for all the cells in the flow domain with appropriate boundary conditions. When the right hand side is sub-iterated towards zero,  $\mathbf{U}^{s+1}$  approaches the time-accurate  $\mathbf{U}^{n+1}$ . In order to solve this system of equations, a large matrix is to be handled at each iteration level. The variable  $\Delta\mathbf{U}$  in any single equation involves the cell itself and its neighbouring cells. Thus an optimised band matrix can be formed, if systematic numbering of cells is followed. A bandwidth minimization technique developed by Collins (1972) is implemented in the present study and the matrix is stored. Now, the system of equation obtained by applying Eq. (6.53) for all the cells can be solved simultaneously for  $\Delta\mathbf{U}$  values. These values are added to the previous values of  $\mathbf{U}$  such that a better estimation is obtained. This procedure is repeated till the  $\Delta\mathbf{U}$  values are less than a specified tolerance.

The solution scheme is explicit for  $\theta = 0$  and if  $\theta = 1/2$ , the scheme corresponds to trapezium rule with second-order accuracy in time. A fully implicit scheme is obtained for  $\theta = 1$  and this may help in adopting a large time step. In this study, the system of equations is solved by the Gauss elimination method with  $\theta = 1$ .

## 6.9 Application to barrage flow pattern study

In the absence of a real bathymetry of a prototype barrage, one hypothetical barrage is considered for flow simulation. The following pages show in figures the following:

1. Bathymetry (that is, the bottom elevation) of the pond. There is assumed to be a shoal some distance upstream of the barrage axis (Fig. 6.5).
2. Mesh of the hypothetical pond behind a barrage (Fig. 6.6). The flow is from left to right. There are 8 gate bays of the barrage and the flow through each is unequally distributed. The gates of the bays on the left are opened comparatively more than those on the right. The middle bay gates are assumed to be closed.
3. Flow vectors, after plotting the output as obtained using the flow modelling software TINFLOW2D (Fig. 6.6).

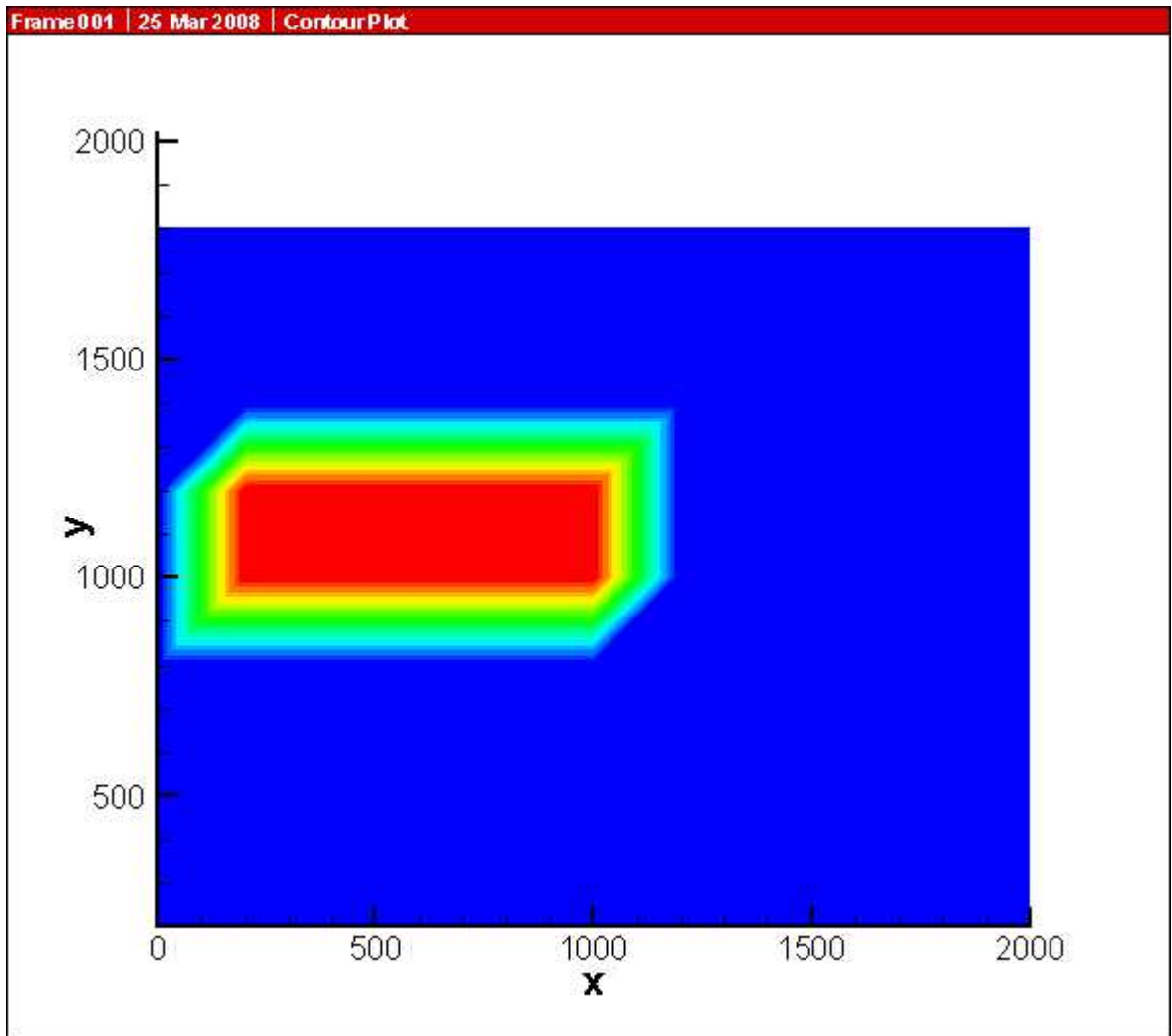


Figure 6.5. Bathymetry of the hypothetical barrage pond in plan. A sedimented mound (shoal) is assumed to be towards the upper left of the plan.

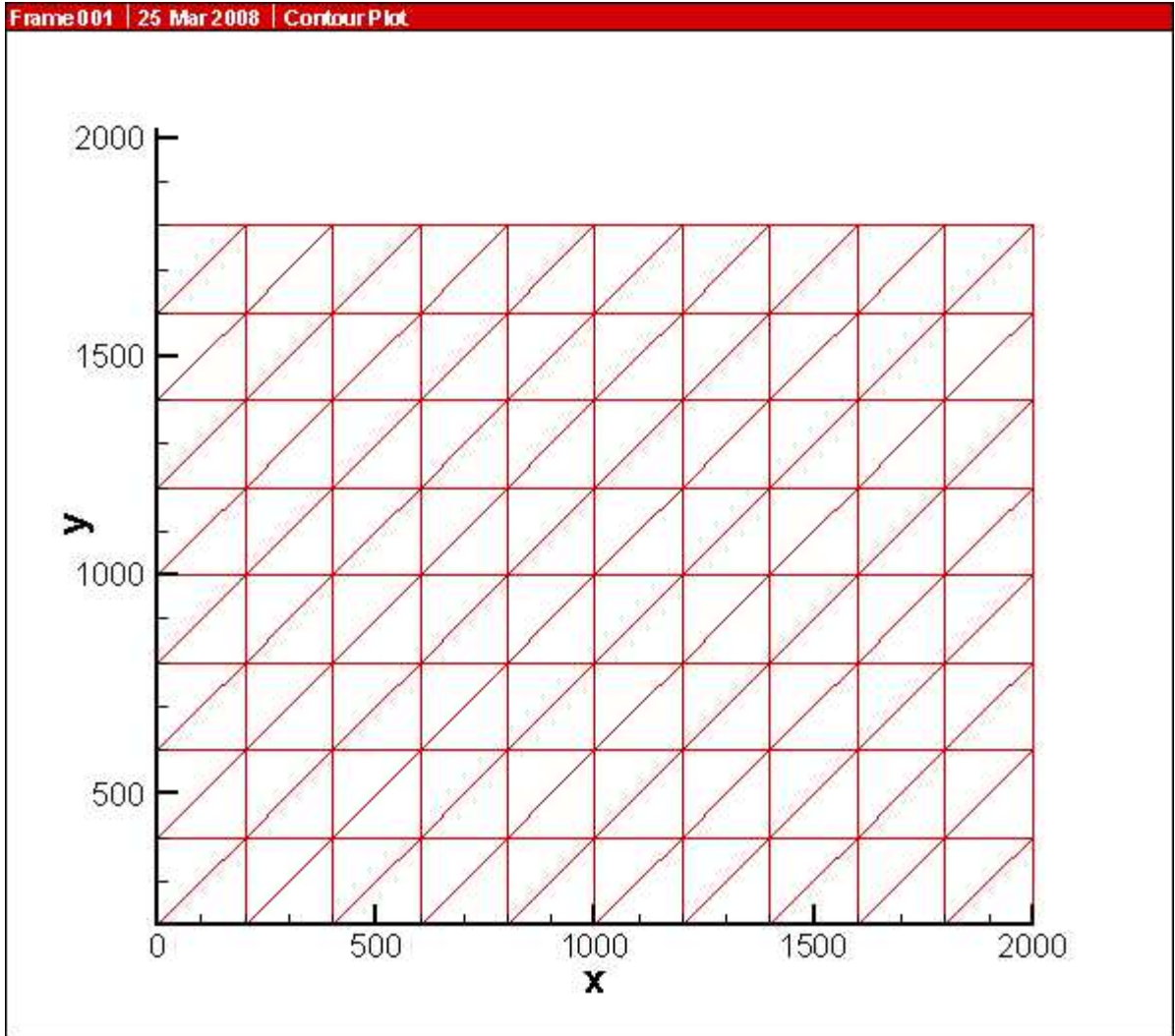


Figure 6.6 Computational mesh (generated as a regular triangular grid, but in general may be arbitrary, that is, unstructured) for the solution of two-dimension flow by TINFLOW2D

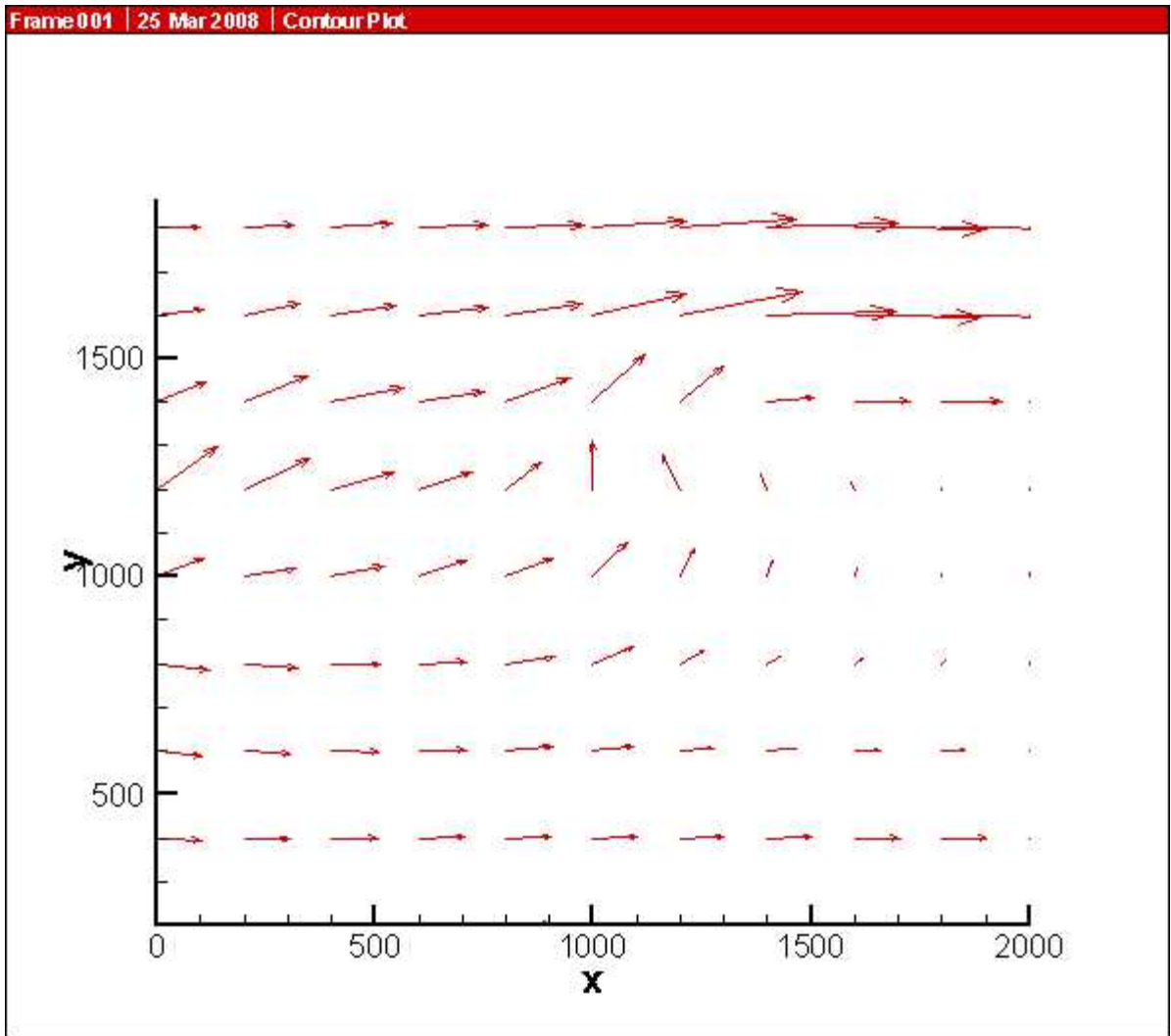


Figure 6.7 Simulated flow patterns as a consequence of both gate operation as well as shoal formation



## References

- Achdou, Y., and Bernardi, C.** (2001). "Adaptive finite-volume or finite-element discretisation of Darcys equations with variable permeability." *Comptes Rendus de L'Academie des Sciences Serie 1-Mathematique*, 333 (7), 693-698.
- Alcrudo, F., and García-Navarro, P.** (1993). "A high-resolution Godunov-type scheme in finite volumes for the 2D shallow water equations." *Int. J. Numer. Methods Fluids*, 16, 489-505.
- Alcrudo, F., García-Navarro, P., and Saviron, J.** (1992). "Flux difference splitting for 1D open channel flow equations." *Int. J. Numer. Methods Fluids*, 14, 1009-1018.
- Anastasiou, K., and Chan, C. T.** (1997). "Solution of the 2D shallow water equations using the finite volume method on unstructured triangular meshes." *Int. J. Numer. Methods Fluids*, 24, 1225-1245.
- Aronica, G., Tucciarelli, T., and Nasello, C.** (1999). "2D multilevel model for flood wave propagation in flood-affected areas." *J. Water Res. Plann. Manag.*, 124, 210-217.
- Aureli, F., Mignosa, P., Tomirotti, M.** (2000). "Numerical-simulation and experimental verification of dam-break flows with shocks." *J. Hydraul. Res.*, 38 (3), 197-206.
- Barth, J. T., and Jespersen, D. C.** (1989). "The design and application of upwind schemes on unstructured meshes." AIAA Paper, 89-0366.
- Bates, P. D., and Anderson, M. G.** (1993). "A two-dimensional finite-element model for river flow inundation." *Proc. R. Soc. Lond. A*, 440, 481-491.
- Bates, P. D., and Hervouet, J. -M.** (1999). "A new method for moving boundary hydrodynamics problems in shallow water." *Proc. R. Soc. Lond. A*, 455, 3107-3128.
- Bates, P., Anderson, M., Price, D., Hardy, R., and Smith, C.** (1996). "Analysis and development of hydraulic models for floodplain flows." In: *Floodplain Processes*, 215-254, John Wiley & Sons.
- Beffa, C., and Connell, R. J.** (2001). "Two-dimensional flood plain flow. I: model description." *J. Hydrol. Eng.*, 6(5), 397-405.
- Begnudelli, L. and Sanders, B. F.** (2006). "Unstructured grid finite-volume algorithm for shallow water flow and scalar transport with drying and wetting." *J. Hydraul. Eng.*, 132(4), 371-384.
- Benqué, J. P., Hauguel, A., and Viollet, P. L.** (1982). *Engineering applications of computational hydraulics*. Vol. 2, Pitman Publications.
- Bento-Franco, A.** (1996). "Modelacao computacional e experimental de escoamentos provocados por roturas de barragens." *Ph. D. Thesis*. Universidade Tecnica de Lisboa, Portugal.
- Berger, R. C., and Stockstill, R. L.** (1995). "Finite-element model for high-velocity channels." *J. Hydraul. Eng.*, 121(10), 710-716.
- Bermúdez, A., and Vázquez-Cendón, M. E.** (1994). "Upwind methods for hyperbolic conservation laws with source terms." *Comput. Fluids*, 23(8), 1049-1071.

- Berzins, M., and Ware, J. L.** (1995). "Positive cell-centred finite volume discretisation methods for hyperbolic equations on irregular meshes." *Appl. Numer. Math.*
- Billett, S. J., and Toro, E. F.** (1997). "On WAF-type schemes for multi-dimensional hyperbolic conservation laws." *J. Comput. Phys.*, 130, 1-24.
- Borthwick, A. G. L., Leon, S. C., and Jozsa, J.** (2001). "Adaptive quadtree model of shallow-flow hydrodynamics." *J. Hydraul. Res.*, 39 (4), 413-424.
- Bradford, S. F., and Sanders, B. F.** (2002). "Finite volume model for shallow-water flooding of arbitrary topography." *J. Hydraul. Eng.*, 128(3), 289-298.
- Brufau, p., and García-Navarro, P.** (2000). "2-Dimensional dam-break flow simulation." *Int. J. Numer. Methods Fluids*, 33 (1), 35-57.
- Brufau, P., and García-Navarro, P.** (2003). "Unsteady free surface flow simulation over complex topography with a multidimensional upwind technique." *J. Comput. Phys.*, 186, 503-526.
- Brufau, P., Vázquez-Cendón, M. E., and García-Navarro, P.** (2002). "A numerical model for the flooding and drying of irregular domains." *Int. J. Numer. Methods Fluids*, 39, 247-275.
- Burguete, J., and García-Navarro, P.** (2001). "Efficient construction of high-resolution TVD conservative schemes for equations with source terms: Application to shallow water flows." *Int. J. Numer. Methods Fluids*, 37, 209-248.
- Caleffi, V., Valiani, A., and Zanni, A.** (2003). "Finite volume method for simulating extreme flood events in natural channels." *J. Hydraul. Res.*, 41 (2), 167-177.
- Casulli, V., and Stelling, G. S.** (1998). "Numerical simulation of 2D quasi-hydrostatic, free surface flows." *J. Hydraul. Eng.*, 124(7), 678-686.
- Collins, R. J.** (1972). "Bandwidth reduction by automatic renumbering.", *Int. J. Numer. Methods Eng.*, 6(3), 345-356.
- Connell, R. J., Painter, D. J., and Beffa, C.** (2001). "Two-dimensional flood plain flow. II: Model validation." *J. Hydrol. Eng.*, 6(5), 406-415.
- Cueto-Felgueroso, L., Colominas, I., Navarrina, J. F. F., Casteleiro, M.** (2006). "High-order finite volume schemes on unstructured grids using moving least-squares reconstruction. Application to shallow water dynamics." *Int. J. Numer. Methods Eng.*, 65, 295-331.
- Cunge, J. A., Holly, F. M., and Verwey, A.** (1980). *Practical Aspects of Computational River Hydraulics*. Pitman Publishing Limited, London.
- Chaudhry, M. H.** (1994). *Open-Channel Flow*. Prentice Hall of India Pvt. Ltd., New Delhi.
- Chow, V. T.** (1973). *Open Channel Hydraulics*. McGraw-Hill, New York.
- Delis, A. I., Skeels, C. P., and Ryrie, S. C.** (2000). "Evaluation of some approximate Riemann solvers for transient open channel flows." *J. Hydraul. Res.*, 38(3), 217-231.
- Dodd, N.** (1998). "Numerical model of wave run-up, overtopping, and regeneration." *J. Waterw., Port, Coastal, Ocean Eng.*, 124(2), 73-81.

- Fennema, R. J., and Chaudhry, M. H.** (1990). "Explicit methods for 2-D transient free-surface flows." *J. Hydraul. Eng.*, 116(8), 1013-1034.
- Fraccarollo, L., and Toro, E. F.** (1995). "Experimental and numerical assessment of the shallow water model for two-dimensional dambreak type problems." *J. Hydraul. Res.*, 33, 843-864.
- García-Navarro, P., and Vázquez-Cendón, M. E.** (2000). "On numerical treatment of the source terms in shallow water equations." *Comput. Fluids*, 29(8), 951-979.
- Ghamry, H. K, and Steffler, P. M.** (2005). "Two-dimensional depth-averaged modelling of flow in curved open channels." *J. Hydraul. Res.*, 43, 44-55.
- Glaister, P.** (1988). "Approximate Riemann solutions of the shallow water equations." *J. Hydraul. Res.*, 26(3), 293-306.
- Goutal, N., and Maurel, F.** (1997). *Technical Report HE-43/97/016/A*, Electricité de France, Département Laboratoire National d'hydraulique, Groupe Hydraulique Fluviale.
- Harten, A., and Hyman, J. M.** (1983). "Self adjusting grid method for one-dimensional hyperbolic conservation laws." *J. Comput. Phys.*, 50, 235-296.
- Hauke, G.** (1998). "A symmetrical formulation for computing transient shallow-water flows." *Comp. Methods Appl. Mech. Eng.*, 163, 111-122.
- Hauke, G.** (2002). "A stabilized finite element method for the Saint Venant equations with application to irrigation." *Int. J. Numer. Methods Fluids.*, 38, 963-984.
- Heinrich, P., Piatanesi, A., Okal, E., and Hebert, H.** (2000). "Near-field modelling of the July 17, 1998 Tsunami in Papua-New-Guinea." *Geograph. Res. Letters* 2000, 27 (19), 3037-3040.
- Heniche, M., Secretan, Y., Boudreau, P., and Leclerc, M.** (2000). "A two-dimensional finite element drying-wetting shallow water model for rivers and estuaries." *Adv. Water. Resou.*, 23, 359-372.
- Hervouet, J. -M., and Janin, J. -M.** (1994). "Finite element algorithms for modelling flood propagation." In: *Modelling flood propagation over initially dry areas*, Edited by Molinaro, P., and Natale, L., ASCE, New York, 101-113.
- Hervouet, J., and Haren, L. V.** (1996). "Recent advances in numerical methods for fluid flows." In: *Floodplain Processes*, 182-214, John Wiley & Sons.
- Hervouet, J., -M., and Petitjean, A.** (1999). "Malpasset dam-break revisited with 2-dimensional computations." *J. Hydraul. Res.*, 37 (6), 777-788.
- Hesselink, A., Stelling, G., Kwadijk, J., and Middelkoop, H.** (2003). "Inundation of a dutch river polder, sensitivity analysis of a physically based inundation model using historic data." *Water Res. Res.*, 39, 1234.
- Hirsch, C.** (1988). *Numerical Computation of Internal and External Flows*. Vol. II. John Wiley & Sons, Inc., New York.
- Hirt, C. W., and Nichols, B. D.** (1981). "Volume of fluid (VOF) method for the dynamics of free boundaries." *J. Comput. Phys.*, 29, 201.

- Holmes, D. G., and Connel, S. D.** (1989). "Solution of the 2D Navier Stokes equations on unstructured adaptive grids." *Proc., AIAA 9<sup>th</sup> CFD Conf.*, AIAA Paper, 89-1932.
- Hubbard, M. E.** (1999). "Multidimensional slope limiters for MUSCL-type finite volume schemes on unstructured grids." *J. Comput. Phys.*, 155, 54-74.
- Hubbard, M. E., and García-Navarro, P.** (2000). "Flux difference splitting and the balancing of source terms and flux gradients." *J. Comput. Phys.*, 165(1), 89-125.
- Imamura, F.** (1996). "Review of tsunami simulation with a finite difference method." In: long-wave run-up mathematical models, Edited by Yeh, Liu and Synolakis, World Scientific, 25-42.
- Ippen, A. T, and Drinker, P. A.** (1962). "Boundary shear stress in curved trapezoidal channel." *J. Hydraul. Div.*, 88, 143-79.
- Ivanenko, S. A., and Muratova, G. V.** (2000). "Adaptive grid shallow water modelling." *Appl. Numer. Math.*, 32 (4), 447-482.
- Jawahar, P., and Kamath, H.** (2000). "A high-resolution procedure for Euler and Navier-Stokes computations on unstructured grids." *J. Comput. Phys.*, 164, 165-203.
- Katopodes, N. D.** (1984). "A dissipative Galerkin scheme for open channel flow." *J. Hydraul. Eng.*, 110(6), 450-466.
- Katopodes, N. D., and Strelkoff, R.** (1978). "Computing two-dimensional dam-break flood waves." *J. Hydr. Div.*, 104(9), 1269-1288.
- Komaei, S. and Bechteler, W.** (2004). "An improved, robust implicit solution for the two-dimensional shallow water equations on unstructured grids." *Proc. 2<sup>nd</sup> int. Conf. on Fluvial Hydraulics*, M. Greco, Ed., Vol. 2, 1065-1072, Balkema, Rotterdam.
- Kuiry, S. N. and Sen, D. J.** (2006). "Finite volume model for the shallow water equations on unstructured quadrilateral meshes." *Comput. Fluids*, (under review).
- Kuiry, S. N., Pramanik, K, and Sen, D. J.** (2006). "Finite volume model for the shallow water equations with improved treatment of the source terms." *J. Hydraul. Eng.*, (accepted for publication, March 2007).
- Lai, C.** (1986). "Numerical modelling of unsteady open-channel flow." In: *Advances in Hydrosience*, Academic Press, New York.
- Laura, R. A., and Wang, J. D.** (1984). "Two-dimensional flood routing on steep slope." *J. Hydraul. Eng.*, 110 (8), 1121-1135.
- Linder, K.** (1982). "Der strömungswiderstand von pflanzenbeständen." Fachbereich für Bauingenieur und Vermessungswesen, TU Braunschweig, Braunschweig, Germany.
- Molls, T., and Chaudhry, M. H.** (1995). "Depth-averaged open-channel flow model." *J. Hydraul. Eng.*, 121(6), 453-465.
- Murillo, J., Burguete, J., Garía-Navarro, P., and Brufau, P.** (2004). "Consideration of flood propagation model performance in relation to laboratory physical model data." *IMPACT project technical report 2004*.
- Nagata, N, Hosoda, T., and Muramoto, Y.** (2000). "Numerical analysis of river channel processes with bank erosion." *J. Hydraul. Eng.*, 126(4), 243-252.

- Niceno, B.** "A two-dimensional quality mesh generator" <[http://web.mit.edu/easymesh\\_v1.4/www/easymesh.html](http://web.mit.edu/easymesh_v1.4/www/easymesh.html)>.
- Nujic, M.** (1995). "Efficient implementation of non-oscillatory schemes for the computation of free surface flow." *J. Hydraul. Res.*, 33(1), 101-111.
- Osher, S., and Solomone, F.** (1982). "The computation of transonic flow through two-dimensional gas turbine cascades." *ASME Paer 71-GT-89*, American Society of Mechanical Engineers, New York, NY.
- Paquier, A., and Farisser, P.** (1996). *Use of 2D model for simulating the flooding of plain*. In: *Hydroinformatics 1996*, Edited by Müller, 129-136, Balkema, Rotterdam.
- Roe, P. L.** (1981). "Approximate Riemann solvers, parameter vectors and difference schemes." *J. Comput. Phys.*, 43, 357-372.
- Roe, P. L.** (1986). "A basis for upwind differencing of the two-dimensional unsteady Euler equations." *Numer. Methods Fluid Dyn. II*, Oxford University Press.
- Rogers, B., Fujihara, M., and Borthwick, A. G. L.** (2001). "Adaptive Q-tree Godunov-type scheme for shallow water equations." *Int. J. Numer. Methods Fluids.*, 35 (3), 247-280.
- Rozovskii, I. L.** (1957). *Flow of water in bends of open channels*. Israel Program for Scientific Translation, Jerusalem, Israel.
- Sanders, B. F.** (2001). "High-resolution and non-oscillatory solution of the St. Venant equations in non-rectangular and non-prismatic channels." *J. Hydraul. Res.*, 39(3), 321-330.
- Sarrate, J., and Huerta, A.** (2000). "Efficient unstructured quadrilateral mesh generation." *Int. J. Numer. Methods. Eng.*, 49, 1327-1350 (2000).
- Sheu, T. W. H., and Fang, C. C.** (2001), "High-resolution finite-element analysis of shallow water equations in 2 dimensions." *Comp. Methods Appl. Mech. Eng.*, 190, 2581-2601.
- Shewchuk, J. R.** (1996). "Triangle: engineering a 2D quality mesh generator and Delaunay triangulator." *Lect. Notes Comput. Sci.*, 1148, 203-222 <<http://www-2.cs.cmu.edu/~quake/triangle.html>>.
- Singh, V., and Bhallamudi, M.** (1997). "Hydrodynamic modeling of basin irrigation." *J. Irr. Drain. Eng.*, 23(6), 407-414.
- Sinha, P. A., Sotiropoulos, F., and Odgaard, A. J.** (1998). "Three-dimensional numerical model for flow through natural rivers." *J. Hydraul. Eng.*, 124(1), 479-508.
- Sleigh, P. A., Berzins, M., Gaskell, P. H., and Wright, N. G.** (1997). "An unstructured finite-volume algorithm for predicting flow in rivers and estuaries." *Comput. Fluids.*, 27(4), 479-508.
- Soares-frazao, S., Lau, J., and Zech, Y.** (1999). "Transient flows in natural valleys computed on topography adapted mesh." In: *Proceedings of Finites Volumes for Complex Applicatios II*, Edited by Vilsmeier, R., Benkhaldoun, F., and Hänel, D., Duisburg, Germany 199-22 July 1999, Hermès, Paris, 403-410.
- Spurk, H. S.** (1997). *Fluid Mechanics*. Springer-Verlag, Berlin, Germany

- Stelling, G. Kernkamp, H., and Laguzzi, M.** (1998). "Delft flooding system: A powerful tool for inundation assessment based on a positive flow simulation." In: *Hydroinformatics 1998*, Edited by Babovic and Larsen, 449-456, Balkema.
- Tan, W.** (1992). *Shallow water hydrodynamics*. Elsevier, Amsterdam, The Netherlands.
- Thacker, W. C.** (1981). "Some exact solutions to the nonlinear shallow water wave equations." *J. Fluid Mech.*, 107, 499-508.
- Toro, E. F.** (1992). "Riemann problems and the WAF method for solving the 2-dimensional shallow-water equations." *Philos. Trans. Royal Soc. London, Series A. Physical Sciences and Engineering* 1649, 338, 43-68.
- Tucciarelli, T., and Termini, D.** (2000). "Finite-element modelling of floodplain flow." *J. Hydraul. Eng.*, 126(6), 416-24.
- Valiani, A., and Begnudelli, L.** (2006). "Divergence form of bed slope source term in shallow water equations." *J. Hydraul. Eng.*, 132(7), 652-665.
- Valiani, A., Caleffi, V., and Zanni, A.** (2002). "Case study: Malpasset Dam-break simulation using two-dimensional finite volume method." *J. Hydr. Engrg.*, 128(5), 460-472.
- Vázquez-Cendón, M. E.** (1999). "Improved treatment of source terms in upwind schemes for the shallow water equations." *J. Comput. Phys.*, 148, 497-526.
- Wang, J. -W., and Liu, R. -X.** (2000). "A comparative study of finite volume methods on unstructured meshes for simulation of 2D shallow water problems." *Math. Comput. Simul.*, 53, 171-184.
- Welch, J. E., Harlow, F. H., Shannon, J. P., and Daly, B. J.** (1966). *The MAC method*. Technical Report LA-3425, Los Alamos National Library.
- Ye, J., and McCorquodale, J. A.** (1998). "Simulation of open channel flows by 3D hydrodynamic model." *J. Hydraul. Eng.*, 124(7), 687-698.
- Yen, B. C.** (1965). *Characteristics of subcritical flow in a meandering channel*. Institute of Hydraulic Research, University of Iowa, Iowa City, IA.
- Yoon, S. B.** (2000). "Coastal flooding simulation using explicit finite difference scheme." In: *Kore-China Conference on port and Coastal Engineering*, September 21-23, Seoul, Korea.
- Yoon, T. H., and Kang, S. K.** (2004). "Finite volume model for two-dimensional shallow water flows on unstructured grids." *J. Hydraul. Eng.*, 130(7), 678-688.
- Yoon, T. H., Yoon, S. B., Lee, H. J., and Shin, W. T.** (1994). "Prediction of flow velocity due to tidal closing." In: *Proceedings of 36<sup>th</sup> Conference for Korean Association of hydrological Sciences*, Yeosu, Korea, 133-138 (Korean).
- Zhao, D. H., Shen, H. W., Lai, J. S. and Tabios III, G. Q.** (1996). "Approximate Riemann solvers in FVM for 2D hydraulic shock wave modeling." *J. Hydraul. Eng.*, 122(12), 692-702.
- Zhao, D. H., Shen, H. W., Tabios III, G. Q., Lai, J. S., and Tan, W. Y.** (1994). "A finite-volume two-dimensional unsteady flow model for river basins." *J. Hydraul. Eng.*, 120(7), 863-883.

- Zhou, J. G., Causon, D. M., Mingham, C. G., and Ingram, D. M.** (2001). "The surface gradient method for the treatment of source terms in the shallow-water equations." *J. Comput. Phys.*, 168, 1-25.
- Zienkiewicz, O. C., and Taylor, R. I.** (2000). *Finite Element Method. Volume 3-Fluid Dynamics*, Butterworth Heinemann, London, UK.
- Zoppou, C., and Roberts, S.** (1999). "Catastrophic collapse of water supply reservoirs in urban areas." *J. Hydraul. Eng.*, 125 (7), 686-695.